



AFRL-AFOSR-UK-TR-2018-0034

Analysis and Design of Curved Metasurface Structures

Zvonimir Sipus
FAKULTET ELEKTROTEHNIKE I RACUNARSTVA
UNSKA 3
ZAGREB, 10000
HR

08/14/2018
Final Report

DISTRIBUTION A: Distribution approved for public release.

Air Force Research Laboratory
Air Force Office of Scientific Research
European Office of Aerospace Research and Development
Unit 4515 Box 14, APO AE 09421

REPORT DOCUMENTATION PAGE					Form Approved OMB No. 0704-0188	
<p>The public reporting burden for this collection of information is estimated to average 1 hour per response, including the time for reviewing instructions, searching existing data sources, gathering and maintaining the data needed, and completing and reviewing the collection of information. Send comments regarding this burden estimate or any other aspect of this collection of information, including suggestions for reducing the burden, to Department of Defense, Executive Services, Directorate (0704-0188). Respondents should be aware that notwithstanding any other provision of law, no person shall be subject to any penalty for failing to comply with a collection of information if it does not display a currently valid OMB control number.</p> <p>PLEASE DO NOT RETURN YOUR FORM TO THE ABOVE ORGANIZATION.</p>						
1. REPORT DATE (DD-MM-YYYY) 14-08-2018		2. REPORT TYPE Final		3. DATES COVERED (From - To) 01 Jun 2015 to 28 Feb 2018		
4. TITLE AND SUBTITLE Analysis and Design of Curved Metasurface Structures				5a. CONTRACT NUMBER		
				5b. GRANT NUMBER FA9550-15-1-0121		
				5c. PROGRAM ELEMENT NUMBER 61102F		
6. AUTHOR(S) Zvonimir Sipus				5d. PROJECT NUMBER		
				5e. TASK NUMBER		
				5f. WORK UNIT NUMBER		
7. PERFORMING ORGANIZATION NAME(S) AND ADDRESS(ES) FAKULTET ELEKTROTEHNIKE I RACUNARSTVA UNSKA 3 ZAGREB, 10000 HR				8. PERFORMING ORGANIZATION REPORT NUMBER		
9. SPONSORING/MONITORING AGENCY NAME(S) AND ADDRESS(ES) EOARD Unit 4515 APO AE 09421-4515				10. SPONSOR/MONITOR'S ACRONYM(S) AFRL/AFOSR IOE		
				11. SPONSOR/MONITOR'S REPORT NUMBER(S) AFRL-AFOSR-UK-TR-2018-0034		
12. DISTRIBUTION/AVAILABILITY STATEMENT A DISTRIBUTION UNLIMITED; PB Public Release						
13. SUPPLEMENTARY NOTES						
14. ABSTRACT <p>The purpose of this project is to develop an analysis approach and specialized programs that are able to efficiently and accurately design curved multilayer metasurface structures. The proposed approach combines the concept of sheet impedance with a new transmission matrix formulation that is applicable to stratified, canonical curved geometries. The results are verified both numerically and experimentally through many metasurface examples of cylindrical and spherical shape, as well as through structures with body of revolution type of symmetry.</p>						
15. SUBJECT TERMS EOARD, Metamaterials						
16. SECURITY CLASSIFICATION OF:			17. LIMITATION OF ABSTRACT	18. NUMBER OF PAGES	19a. NAME OF RESPONSIBLE PERSON	
a. REPORT	b. ABSTRACT	c. THIS PAGE			FOLEY, JASON	
Unclassified	Unclassified	Unclassified	SAR		19b. TELEPHONE NUMBER (Include area code) 011-44-1895-616036	

Analysis and Design of Curved Metasurface Structures

by

**Zvonimir Šipuš
Marko Bosiljevac
Dominik Barbarić
Zoran Ereš
Mladen Vukomanović**

SUBMITTED BY: Prof. Zvonimir Sipus
Faculty of Electrical Engineering and Computing
University of Zagreb
Unska 3
Zagreb, HR-10000, Croatia

30 June 2018

TABLE OF CONTENTS

PROJECT OBJECTIVE AND REALIZED OUTCOMES	5
INTRODUCTION.....	9
2.1 FORMULATION OF GENERAL METASURFACE ELECTROMAGNETIC PROBLEM	10
MODELING CASCADED CURVED METASURFACES WITH HOMOGENEOUS SURFACE IMPEDANCE.....	13
3.1 INTRODUCTION	13
3.2 ANALYSIS OF SINGLE-LAYER CYLINDRICAL METASURFACE	14
3.3 ANALYSIS OF CASCADED CYLINDRICAL METASURFACE STRUCTURES	16
3.4 ALGORITHM FOR CALCULATING GREEN'S FUNCTIONS OF CASCADED METASURFACE STRUCTURES	18
3.5 EXACT SURFACE IMPEDANCE VS. APPROXIMATIONS	20
3.6 SELECTION OF OPTIMAL ELEMENTS FOR CYLINDRICAL METASURFACES	24
3.7 INFLUENCE OF MUTUAL COUPLING BETWEEN METASURFACE LAYERS	26
3.8 ANALYSIS OF CASCADED SPHERICAL METASURFACE STRUCTURES.....	29
MODELING CASCADED CURVED METASURFACES WITH NON-HOMOGENEOUS SURFACE IMPEDANCE.....	35
4.1 SINGLE-LAYER CURVED NON-HOMOGENEOUS METASURFACE SHEET IN FREE-SPACE.....	36
4.2 CASCADED CURVED NON-HOMOGENEOUS METASURFACE SHEETS EMBEDDED INTO A MULTILAYER STRUCTURE.....	44
4.3 COMPARISON OF TWO APPROACHES OF CALCULATING METASURFACE SHEET IMPEDANCE	46
ANALYSIS OF BODY-OF-REVOLUTION (BOR) METASURFACE STRUCTURES	48
5.1 GEOMETRY OF THE BOR PROBLEM	48
5.2 FORMULATION OF THE ELECTRIC FIELD INTEGRAL EQUATION	49
5.3 THE METHOD OF MOMENTS (MoM)	52
5.4 NUMERICAL ALGORITHM FOR CALCULATING GREEN'S FUNCTIONS OF 2D MULTIREGION STRUCTURES.....	60
5.5 NUMERICAL RESULTS	65
MEASURED RESULTS.....	69
6.1 SINGLE-LAYER CYLINDRICAL METASURFACE	69
6.1.1. Monopole feed - curved metasurface printed on a thin substrate with no support layer.....	71
6.1.2. Monopole feed - curved metasurface is printed on a thick substrate support layer	75
6.1.3. Waveguide feed - curved metasurface printed on a thin substrate with no support layer	77
6.2 TWO-LAYER CYLINDRICAL METASURFACE	80
6.2.1. Waveguide feed - curved two-layer metasurface	82
6.2.2. Rectangular horn feed - curved two-layer metasurface.....	85
6.3 PRODUCTION OF CURVED METASURFACES STRUCTURES	88
CONCLUSIONS	95
APPENDIX.....	97
A.1 APPROXIMATE EXPRESSIONS FOR SHEET IMPEDANCE OF METASURFACES WITH CANONICAL PATTERNS.....	97
A.2 MOMENT METHOD PROGRAM FOR ANALYZING CIRCULAR-CYLINDRICAL PERIODIC STRUCTURES.....	100
BIBLIOGRAPHY	103

Project objective and realized outcomes

Curved multilayered dielectric structures with embedded metallic patterns (commonly referred to as metasurfaces) can act as electromagnetic devices that direct waves, manipulate the polarization of transmitted or reflected waves, or influence the spectrum properties of those waves. Recently, it was shown that these properties of metasurfaces can be successfully used for building various electromagnetic structures applied in different applications that vary from smart radomes for airplane or missile applications (in particular nose radomes) to subreflectors for multi-frequency antenna reflector systems. Till now most of the attention was focused on the development of planar metasurface structures, however, many demanding electromagnetic applications require the implementation of curved structures. Introduction of curvature significantly complicates the analysis and the design since the quasi-infinite periodicity used in planar structures is lost in this case (if the structure is curved in both principal directions). Furthermore, the considered structures are very large in terms of wavelength and they contain a lot of small metallic details within each of the metasurface layers (by definition, the unit cell of the metasurface pattern is much smaller than the wavelength). With all this in mind in order to successfully design curved metasurface structures one needs to develop a specialized efficient numerical analysis algorithms. The need for this specialized program lies in the fact that these large finite structures with numerous small cells cannot be efficiently designed using general electromagnetic solvers since the needed computer time for analyzing such complex structures would be very long (quite often more than several tens of hours or even days), memory requirements would be extremely large and the successful optimization would simply be too slow.

The objective of the project is to develop a systematic approach and associated computer programs for designing curved multilayer structures containing metasurface layers. First part of the project was focused on the development of an efficient and accurate program for designing such structures, while second part was focused on the development of experimental prototypes that demonstrated the abilities of the developed analysis and design approach.

The development of efficient and accurate programs was based on combining several approaches that show superior properties when designing electromagnetic structures containing metasurface layers:

(1) Modeling of a curved metasurface sheet

Metasurface structures are usually very complex and it is extremely time consuming to directly analyze them using general EM solver (note that it is practically impossible to use optimization procedure in such cases since one evaluation of the cost function takes typically numerous hours). Therefore, one needs good approximate models of metasurface sheets without going into details about their geometries. In the planar case the metasurface sheets were successfully analyzed using the surface sheet impedance approach. Therefore, as a first step we have developed a model of curved metasurface sheets using the modified surface impedance approach. In planar case the value of surface impedance tensor $\bar{\bar{Z}}$ depends on frequency, polarization and angle of incidence. In conformal case we need to include principle radii of curvature and the EM wave variation along the metasurface of the impinging wave. Both of them play a crucial role in selecting types of elements for building curved metasurface sheets. Note that the local value of the surface impedance tensor $\bar{\bar{Z}}$ can be determined using either the specialized software, approximate formulas, or the general electromagnetic software.

(2) Analysis of canonical curved multilayer metasurface structures

The second step in developing general program for analyzing curved metasurface structures was the development of a program for analyzing canonical curved multilayer metasurface structures – cylindrical and spherical ones. There are two main reasons why we have chosen this intermediate step. The first reason is that the program for the analysis of canonical metasurface structures is extremely fast and thus the needed computer time for getting the parameters of the considered design is very short. Therefore, we have connected the developed analysis programs with a global optimization routine in order to obtain the initial design of the metasurface structure, which can serve as a starting point for making a design of the final general structure. Another reason for developing the program for analyzing canonical structures, perhaps even more important, is that such program makes it possible to investigate all the effects that are caused by the bending of metasurfaces. In other words, by analyzing canonical structures it is possible to understand what are the differences in the electromagnetic parameters of curved metasurfaces (compared to the planar structures) and to incorporate this knowledge into the process for designing general curved metasurface structures.

The analysis of canonical multilayer metasurface structures is based on combining the surface impedance approach for modeling the curved metasurface sheet with the ABCD matrix approach for modeling cascaded metasurface structures. We have made the extension of ABCD matrix approach (originally derived for planar multilayer structures) to include the cylindrical and spherical geometries. The generalization is based on representing the curved dielectric layer as cylindrical or spherical transmission lines, and proper description of transmission line modes was used in the derivation of ABCD matrix parameters.

The surface impedance tensor $\bar{\bar{Z}}$ can be determined either by a rigorous EM solver, such as the Method of Moments (MoM), or by an approximate approach. The latter approach gives the value of tensor $\bar{\bar{Z}}$ that does not change with the curvature of the structure and with the angular variation of the incidence field. This can lead to inaccuracies if $\bar{\bar{Z}}$ changes rapidly as a function of the spectral variable (in other words, such approach gives a very poor

approximation of tensor $\bar{\bar{Z}}$). Furthermore, it was demonstrated on several examples that the knowledge of angular variation of tensor $\bar{\bar{Z}}$ gives the information about which type of metasurface realization gives the best electromagnetic parameters (i.e. patches, crosses and Jerusalem crosses can give the same value of tensor $\bar{\bar{Z}}$ in the planar case, but bending the metasurface sheet with such building elements gives quite different curvature effects). Therefore, accurate modeling of surface impedance tensor $\bar{\bar{Z}}$ is extremely important in the design process.

To conclude, the reported method for analysis of canonical curved multilayer metasurface structures represents a powerful starting point in the design of general curved metasurface structures. Furthermore, the proposed method aids in selecting the type of patterned sheet that is needed to obtain a desired angular variation of surface impedance tensor $\bar{\bar{Z}}$.

(3) Analysis of curved metasurfaces with spatially-varying impedance distribution

Some devices like e.g. cylindrical or spherical cloaks would require homogeneous distribution of surface impedance. However, many devices would require spatially-varying impedance distribution in order to modulate amplitude and phase of incoming wave. Furthermore, quite often the considered metasurface is occupying only a part of canonical surface (such as a cylinder or a sphere). One example is a dome antenna with a purpose to either flatten the gain dependency or to enhance the gain of the antenna array inside the dome. Consequently, the analysis approach for canonical curved structures was generalized in order to include a class of metasurface structures with spatially-varying impedance distribution. There are several ways how to make this generalization. As demonstrated in the report, the most suitable selection depends on the domain in which we would like to calculate the metasurface sheet impedance distribution (i.e. spatial or spectral domain) and on the way how we would like to calculate the needed Green's functions. Fortunately, all the possibilities lead to a solution of the same complexity and accuracy.

(4) Analysis of general curved multilayer metasurface structures with Body-of-Revolution (BoR) type of symmetry

Most curved metasurface structures of interest (smart radomes, nose radomes, reflectors and subreflectors, etc.) contain Body-of-Revolution (BoR) symmetry. Therefore, in order to develop a fast and accurate program for design purposes, we have decided to develop a computer program for curved metasurfaces structures with BoR type of symmetry. By this a general three-dimensional electromagnetic problem is transformed into a spectrum of two-dimensional problems which are much easier and faster to solve. The developed program is very general, it is based on the Moment Method with sub-domain basis and test functions (used to solve two-dimensional problems), the analyzed structure can be multilayer and can contain arbitrary number of metasurface layers, the value of the surface impedance tensor can vary spatially and can have different values for different angular variation of the incident wave, etc. The developed program is written in a form of an algorithm. We named the algorithm the G2DMULT-BoR algorithm, i.e. the algorithm that calculates the Green's functions of two-dimensional (2D) multilayer structures with body-of-revolution type of symmetry.

(5) Experimental verification of the developed analysis and design method

Second part of the project was focused on the realization of practical curved metasurface prototypes needed to answer two questions – is it possible to successfully use the developed computer programs for designing realistic electromagnetic devices, and which technology can be used for making such structures. The planar metasurface structures can be easily built using the printed circuit board (PCB) technology. The same technology can be used for singly-curved structures. One need to consider the flexural modulus of selected substrate, i.e. one has to select a substrate that is suitable for bending (luckily, the substrate producers offer such products). However, double-curved structures cannot be built in such a way and some alternative technology should be implemented. In recent years, there is an expansion of 3D printing methods and we propose to test if such technology can be used for building double-curved metasurface structures. The main problem in this realization will be to obtain accurate metallization of the desired pattern, and as a part of the project we have investigated several metallization approaches. The easiest approach is to use a spray with conductive (most often silver-based) paint. However, such method is not suitable for obtaining metasurfaces with geometrically small details. Furthermore, the ohmic losses are larger comparing with the structures produced using printed circuit technology. Much better properties can be obtained with sputtering process (however, one needs to have access to such production technology). The last considered option is metallization of 3D printed structures using electroless copper plating process. It is important to note that in all considered methods one first needs to manufacture or print an appropriate mold pattern or template to apply the metallization on the dielectric sample.

Introduction

New electromagnetic devices that contain metamaterial structures have attracted strong interest over the past several years. Metamaterials are usually engineered by arranging small volume scatterers in a periodic grid with periodicity much smaller than the wavelength. The complex manufacturing of these volume scatterers is often one of the practical limitations (together with small bandwidth and ohmic loss issues) and it is why metamaterial structures are nowadays implemented in only few commercial devices.

Recently, a simplified two-dimensional version of metamaterial structures was proposed. Here the metamaterial structure is realized by printing metallic patterns on dielectric supporting layer. By this a so-called metasurface structure is realized that can be easily produced using printed circuit board technology. In general, metasurfaces have advantage of taking up less physical space than full three-dimensional metamaterial structures (consequently, metasurfaces are structures with smaller ohmic losses). While this interest has resulted in very interesting designs (for example, electromagnetic cloaks and superlenses), it has also initiated research in other directions. In particular, new possibilities for manipulating the direction and polarization properties of transmitted electromagnetic waves have been explored. Traditionally, resonant elements were used in the design of periodic frequency selective surfaces (FSS) [1]. The more recent use of sub-wavelength elements as building blocks for metasurfaces has enabled a wider range of functionality such as focusing, beam tilting, polarization manipulation, and increased bandwidth and angular performance. (see e.g. [2] -[8]).

In modern communication and radar applications there is often the requirement for curved structures which are “smart” in electromagnetic sense. For example, nose radomes on airplanes and missiles are often used to house airborne scanning radar antennas. The presence of these radomes, strongly affects the antenna pattern and causes main beam offset, gain decrease and side-lobe level variation. These are only some of the effects that must accurately be predicted in order to maintain system performances at the desired level. That can be only done if the whole structure is analyzed with accurate software. The size of the structure (in terms of the wavelength) and the ratio between the structure details and the structure size represent considerable practical limitations if general electromagnetic software is used, in particular if the same software is used for optimization purposes [9]. These arguments foster development of a specialized software for the class of electromagnetic problems of interest.

Studies to date have predominantly considered planar surfaces that can be realized using conventional planar fabrication techniques. For such surfaces, efficient design approaches based on surface impedance boundary conditions (both penetrable [3] – [6], [10] – [14] and opaque surface impedance formulations [7], [15], [16]) have been developed. However, either

for mechanical/aerodynamic, or electromagnetic reasons, some metasurface designs require curvature. In general, introducing curvature to metasurface design is a challenging task, since one needs to deal with finite dimensions and a more complex periodicity. Several other difficulties arise when translating analysis and design approaches from planar to curved structures. For example, the projection of a periodic grid onto curved surfaces becomes an issue, and incident plane waves are scattered as a spectrum of reflected waves, as opposed to a single plane wave in the planar case. Cylindrical metasurfaces, fabricated from flexible printed circuit boards, have been considered in the past as attractive class of curved metasurface structures. They were used for reshaping radiation patterns [17], [18], mantle cloak realizations [19], [20], the reduction of antenna blockage [21], and scattering manipulation and camouflage [22].

2.1 Formulation of general metasurface electromagnetic problem

Ideally, a wave-shaping metasurface can be considered as a thin, planar or curved electromagnetic structure that transforms an arbitrary impinging field distribution into the desired scattered wave. An analytical approach to define the needed properties of the considered metasurface that has been recently proposed is based on implementation of the surface equivalence principle [5], [6]. In order to create the desired field distribution in different regions of space (see Fig. 2.1), the additional electric and magnetic currents must be enforced over the interface in order to satisfy the electromagnetic boundary conditions. In other words, we need to somehow obtain electric and magnetic currents that have the role of equivalent currents in the equivalence theorem:

$$\mathbf{J}^{eq} = \hat{n} \times (\mathbf{H}_2 - \mathbf{H}_1), \quad \mathbf{M}^{eq} = -\hat{n} \times (\mathbf{E}_2 - \mathbf{E}_1) \quad (2.1)$$

where \mathbf{J}^{eq} and \mathbf{M}^{eq} are the required distribution of surface electric and magnetic currents.

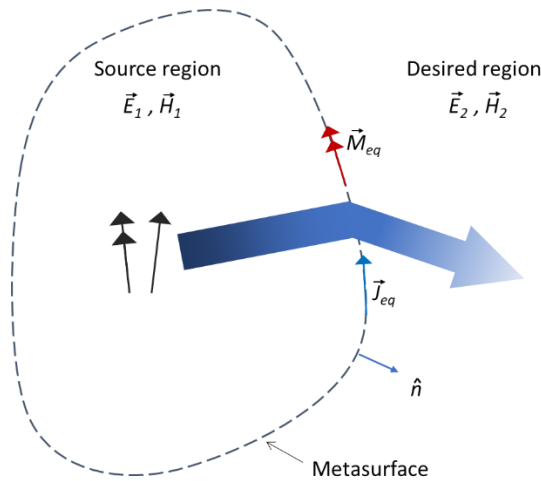


Fig. 2.1. *Metasurfaces inspired with equivalence principle.*

One way to achieve the needed current distribution is incorporate carefully excited electric and magnetic dipole antennas over the virtual boundary, which is usually not easy to obtain in practice. Other approach is based on inducing polarization currents on suitably designed admittance surfaces. In this case, the electric and magnetic polarizability can be tailored to

satisfy the condition (2.1), i.e. to obtain the desired field distribution. The needed Huygens electric surface impedance $\bar{\bar{Z}}^E$ and magnetic surface admittance $\bar{\bar{Y}}^H$ is related to the average tangential fields along the interface [5]:

$$\hat{n} \times \mathbf{E}_{av} = \hat{n} \times \left[\bar{\bar{Z}}^E \cdot \mathbf{J}^{eq} \right] = \hat{n} \times \left[\bar{\bar{Z}}^E \cdot (\hat{n} \times (\mathbf{H}_2 - \mathbf{H}_1)) \right] \quad (2.2)$$

$$\hat{n} \times \mathbf{H}_{av} = \hat{n} \times \left[\bar{\bar{Y}}^H \cdot \mathbf{M}^{eq} \right] = \hat{n} \times \left[\bar{\bar{Y}}^H \cdot (-\hat{n} \times (\mathbf{E}_2 - \mathbf{E}_1)) \right] \quad (2.3)$$

Here the notation *av* means the average of two tangential field components along the different sides of the interface. Note that the necessity of a magnetic response on the surface is connected with a request for symmetry breaking. A combined magnetic and electric response can result in breaking the radiation symmetry of the surface that enables the desired wave control without unwanted back-reflection [23].

At microwaves, an immediate candidate to realize an electromagnetically polarizable surface is to employ loaded wires and loop antennas or metallic patterns, designed to follow the desired effective sheet impedances, at least at closely spaced discrete points on the surface. Magnetic effects, however, are usually not compatible with simplicity of production using standard printed circuit-board technology. Furthermore, inducing this magnetic response in conjunction with the electric properties of a thin surface is one of the main challenges in applying the Huygens metasurfaces in the optical frequency range.

Recently, it has been demonstrated that an arbitrary wavefront and polarization distribution of a transmitting metasurface can be achieved with cascaded metasurfaces (containing three or four metasurface layers) with electric response only. The same approach can be applied to opaque metasurfaces designed to reflect the waves with desired wavefront [24]. Theoretical background is given in [4] where it has been shown that one can realize an arbitrary (passive and reciprocal) bianisotropic metasurface by cascading anisotropic sheets with electric responses only.

The electromagnetic problem containing metasurfaces (described with eq. (2.2)) can be solved using the Mode Matching (MM) or the Method of Moments (MoM) approach. The MM approach is suitable for canonical problems where the considered metasurface is of canonical shape (e.g. planar, cylindrical or spherical). Then one can represent the EM fields in terms of the eigenmodes of that type of geometry. The eigenmode expansion itself is obtained by performing the suitable form of two-dimensional (2D) Fourier transformation – in cylindrical case the suitable 2D transformation is combination of Fourier series in ϕ -direction and Fourier transformation in axial direction. The solution is obtained by matching the boundary condition (2.2) by each eigenmode separately (if the metasurface is homogeneous with no sheet impedance variation; the non-homogeneous metasurfaces of canonical shape can also be analyzed with the same approach). The details of the MM approach will be given in chapters 3 and 4.

In the Moment Method (MoM) approach one needs to determine the variation of surface currents defined with eqs. (2.2) and (2.3). The first step in implementing the solution procedure is to define the integral equation. If the metasurface has the electric response only, i.e. if the unknown is the surface electric current distribution, then for the transmitting metasurfaces the integral equation to be numerically solved is [25]:

$$\begin{aligned}\hat{n} \times \mathbf{E}_{av}(\mathbf{r}) &= \hat{n} \times \mathbf{E}^{inc}(\mathbf{r}) + \hat{n} \times \int_S \bar{\bar{G}}^{EJ}(\mathbf{r}|\mathbf{r}') \cdot \mathbf{J}^{eq}(\mathbf{r}') dS' + \hat{n} \times \int_S \bar{\bar{G}}^{EM}(\mathbf{r}|\mathbf{r}') \cdot \mathbf{M}^{eq}(\mathbf{r}') dS' \\ \hat{n} \times \mathbf{E}_{av}(\mathbf{r}) &= \hat{n} \times (\bar{\bar{Z}}^E \cdot \mathbf{J}^{eq}(\mathbf{r}))\end{aligned}\quad (2.4)$$

Here $\bar{\bar{G}}$ denotes the suitable (i.e. problem dependent) dyadic Green's function. For homogeneous space the Green's functions in compact notation are:

$$\bar{\bar{G}}^{EJ}(\mathbf{r}|\mathbf{r}') = j\eta k \left[\bar{\bar{I}} + \frac{\nabla' \nabla'}{k^2} \right] \frac{e^{-jkR}}{4\pi R} \quad (2.5)$$

$$\bar{\bar{G}}^{MJ}(\mathbf{r}|\mathbf{r}') = \nabla \times \left[\frac{e^{-jkR}}{4\pi R} \bar{\bar{I}} \right] \quad (2.6)$$

Here R denotes the distance between the source and observation points $R = |\mathbf{r} - \mathbf{r}'|$. If the metasurface structure has no magnetic response, i.e. if $\mathbf{E}_2 - \mathbf{E}_1 \approx 0$, i.e. under the assumption that the metallic pattern synthesizing the considered metasurface is thin and thus the tangential electrical field is continuous across the metasurface interface, then there is no part with magnetic currents.

If we would like to consider an opaque metasurface that only reflects the EM waves, then we can apply the equation (2.4) with taking into account that $\mathbf{E}_1 = \mathbf{H}_1 = 0$:

$$\begin{aligned}\hat{n} \times \mathbf{E}_2(\mathbf{r}) &= \hat{n} \times \mathbf{E}^{inc}(\mathbf{r}) + \hat{n} \times \int_S \bar{\bar{G}}^{EJ}(\mathbf{r}|\mathbf{r}') \cdot \mathbf{J}^{eq}(\mathbf{r}') dS' + \hat{n} \times \int_S \bar{\bar{G}}^{EM}(\mathbf{r}|\mathbf{r}') \cdot \mathbf{M}^{eq}(\mathbf{r}') dS' \\ \hat{n} \times \mathbf{E}_2(\mathbf{r}) &= \hat{n} \times (\bar{\bar{Z}}^E \cdot \mathbf{J}^{eq}(\mathbf{r}))\end{aligned}\quad (2.7)$$

In this case it is not possible to neglect the term containing the equivalent magnetic currents.

Modeling cascaded curved metasurfaces with homogeneous surface impedance

3.1 Introduction

The focus of this chapter is to introduce analysis approach applicable to canonical curved metasurfaces with uniform sheet impedance distribution; a detailed formulation is presented for cylindrical and spherical cascaded metasurfaces. The proposed analysis combines the concept of sheet impedances in the spectral domain with ABCD transmission matrix formulation to allow the analysis of multilayer structures. In other words, the ABCD matrix formulation for the analysis of cascaded circuit networks as well as planar, stratified electromagnetic structures is extended to cylindrical and spherical geometries, which represent the basis for developing a general code for analyzing multilayer multi-metasurface structures.

The influence of the higher order azimuthal modes is discussed in detail in this chapter. To date, only the dominant zero-order cylindrical mode was considered to obtain a required metasurface reactance (see e.g. [19]-[22]). It will be shown that a metasurface's response to higher order modes (its response to the waves with azimuthal propagation constants different from zero) helps in selecting optimal metasurface elements/textures for a given application. Furthermore, the analytical formulas for the sheet impedance of commonly used planar, metallic patterns are modified to account for curvature.

The first part of the chapter describes both the analysis of single-layer, cylindrical metasurfaces and an ABCD transmission matrix approach for cascaded, concentric structures. The proposed approach is applied to cylindrical structures with various different layers (metallic or dielectric). This is exploited in the Results section by first studying the accuracy of different methods for determining sheet impedances, followed by the investigation of situations where the dependence of sheet impedances on azimuthal modes must be taken into account. Next, two-sheet metasurface example is used to evaluate the number of cylindrical modes needed accurately model the cascaded structures. Finally, the formulation is also applied to spherical metasurface structures.

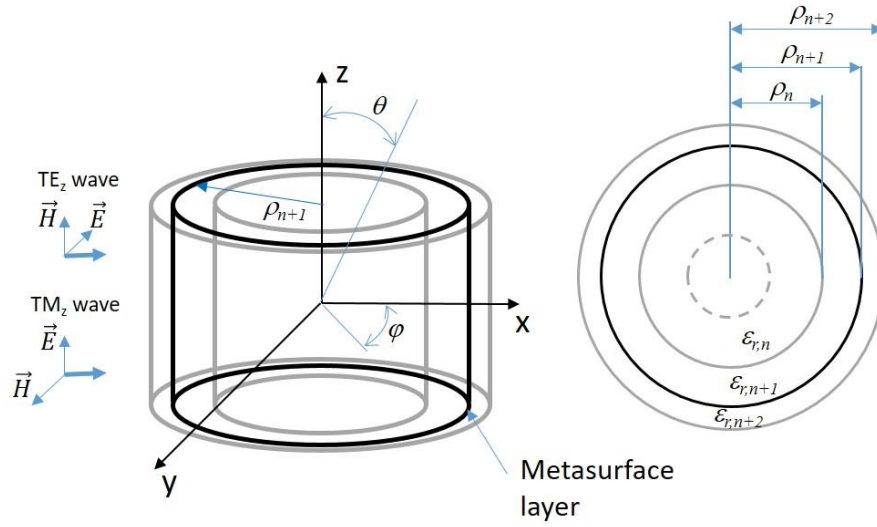


Fig. 3.1. Geometry of curved metasurface structure.

3.2 Analysis of single-layer cylindrical metasurface

Analysis will be performed in the spectral domain. That is, the electromagnetic fields are Fourier transformed along the two dimensions in which the structure is invariant. In the considered cylindrical case, we decompose the EM field into cylindrical waves (e.g. representation of the E-field):

$$\mathbf{E}(\rho, \phi, z) = \sum_{m=-\infty}^{\infty} \int_{-\infty}^{\infty} \tilde{\mathbf{E}}(\rho, m, k_z) e^{-jm\phi} e^{-jk_z z} dk_z \quad (3.1)$$

For the considered cylindrical structure of circular cross-section, one can represent the field distribution in the n th layer in the following way

$$\tilde{E}_z(\rho, m, k_z) = C_{1m} H_m^{(1)}(k_{\rho n} \rho) + C_{2m} H_m^{(2)}(k_{\rho n} \rho), \quad (3.2.a)$$

$$\tilde{H}_z(\rho, m, k_z) = C_{3m} H_m^{(1)}(k_{\rho n} \rho) + C_{4m} H_m^{(2)}(k_{\rho n} \rho). \quad (3.2.b)$$

Here $H_m^{(1)}$ and $H_m^{(2)}$ are the Hankel functions of the first and second kind (they represent inward and outward travelling cylindrical waves), and C_m are the wave amplitudes that need to be determined. The other field components are determined using the following expressions:

$$\tilde{E}_\phi(\rho, m, k_z) = -\frac{mk_z}{k_{\rho n}^2} \tilde{E}_z(\rho, m, k_z) + \frac{j\eta_n k_n}{k_{\rho n}^2} \frac{\partial}{\partial \rho} \tilde{H}_z(\rho, m, k_z) \quad (3.3.a)$$

$$\tilde{H}_\phi(\rho, m, k_z) = -\frac{mk_z}{k_{\rho n}^2} \tilde{H}_z(\rho, m, k_z) - \frac{jk_n}{\eta_n k_{\rho n}^2} \frac{\partial}{\partial \rho} \tilde{E}_z(\rho, m, k_z) \quad (3.3.b)$$

The radial component of the propagation constant is defined as $k_{\rho n}^2 = k_n^2 - k_z^2$, and k_n and η_n are wave number and wave impedance of the considered layer.

For each spectral component, the metasurface layer is modeled using a penetrable sheet impedance boundary condition (an example of geometry is shown in Fig. 3.1):

$$\hat{n} \times \tilde{\mathbf{E}} = \hat{n} \times [\bar{\bar{\mathbf{Z}}} \cdot \tilde{\mathbf{J}}_{av}] = \hat{n} \times [\bar{\bar{\mathbf{Z}}} \cdot (\hat{n} \times (\tilde{\mathbf{H}}^+ - \tilde{\mathbf{H}}^-))] \quad (3.4)$$

Here, $\tilde{\mathbf{E}}$ denotes one spectral component of the averaged electric field at a metasurface layer, $\tilde{\mathbf{H}}^+$ and $\tilde{\mathbf{H}}^-$ are the spectral components of the magnetic field at the outer and inner metasurface boundaries, $\tilde{\mathbf{J}}_{av} = \hat{n} \times (\tilde{\mathbf{H}}^+ - \tilde{\mathbf{H}}^-)$ represents the averaged surface current in the spectral-domain, $\bar{\bar{\mathbf{Z}}}$ is the sheet impedance tensor, and \hat{n} is the outward pointing unit vector, normal to the metasurface layer ($\hat{n} = \hat{\rho}$). Note that the metasurfaces (see Fig. 3.1) introduce a discontinuity in the tangential magnetic field only. In other words, the metasurface only has an electric response, and can be modeled with induced surface electric currents. The generalization to magnetic surface currents (loop or slotted metasurface elements) is straightforward.

The surface impedance tensor $\bar{\bar{\mathbf{Z}}}$ is not a constant tensor but rather depends on the properties of the impinging electromagnetic wave. That is, the nonlocal (spatially dispersive) properties of the metasurface are taken into account. For instance, in the planar case, the nonlocal properties can be characterized by varying the incidence angle of incoming plane wave. Therefore, for each spectral field component, we define the impedance tensor $\bar{\bar{\mathbf{Z}}} = \bar{\bar{\mathbf{Z}}}(m, k_z)$ that can be expressed as

$$\bar{\bar{\mathbf{Z}}}(m, k_z) = \begin{bmatrix} Z_{\phi\phi}(m, k_z) & Z_{\phi z}(m, k_z) \\ Z_{z\phi}(m, k_z) & Z_{zz}(m, k_z) \end{bmatrix}. \quad (3.5)$$

Here, the subscripts denote the corresponding components of the electric field and surface current, respectively. Note that the spectral variable m corresponds to the transverse component of the wave number, $k_t = m/\rho_n$ where ρ_n is the radius of the considered metasurface layer. Given that azimuthal modes with $m \leq k\rho_n$ are propagating, they need to be taken into account when calculating the scattered field. Since the sheet impedance depends on the azimuthal wave number, this dependency should also be taken into account in the calculation, as will be shown in the next section.

As (3.4) indicates, sheet impedances can be calculated from the calculated transverse components of the electromagnetic field on either side of the sheet. This can be done using a solver based on the Moment Method (MoM) [26] or other numerical methods. Often the cylindrical sheet impedance is approximated with the sheet impedance of an equivalent planar sheet. Alternatively, analytical sheet impedance formulas, available for commonly used planar patterns, can be used [27], [28]. In general, these two approximate approaches (note that both are planar approximations) do not account for the sheet impedance's dependence on the spectral variable m . However, the analytical sheet impedance formulas depend on the angle of incidence θ through the spectral variable $k_z = k_0 \cos \theta$. Therefore, the azimuthal dependence of the sheet impedance can also be included by defining a tangential wavenumber that is

azimuthal $k_\phi = m/\rho$. The accuracy of these two simplified methods for determining $\bar{\bar{Z}}$ will be discussed in the next section.

3.3 Analysis of cascaded cylindrical metasurface structures

In order to calculate the response of the cylindrical metasurface, consisting of a cascade of multiple layers, we will use a cylindrical ABCD transmission matrix approach [29]. This approach is a simple, yet powerful tool that allows the analysis of multilayer periodic canonical metasurfaces. One simply needs to analyze each layer separately (find the impedance tensor $\bar{\bar{Z}}$ of each cylindrical sheet and dielectric layer), and then multiply the ABCD matrices of the individual layers to obtain the overall ABCD matrix of the cascaded layers (the metasurface). This approach can also simplify the design/optimization of these cascaded metasurfaces, since it becomes possible to separate the original complex problem into several simpler sub-problems.

Let us consider the case where one wants to calculate the field scattered from an N -layer cylindrical metasurface. The spectral-domain ABCD matrix of a constitutive sheet of the metasurface is given by the following expression:

$$\begin{bmatrix} \tilde{E}_z \\ \tilde{H}_\phi^+ \\ \tilde{E}_\phi \\ \tilde{H}_z^+ \end{bmatrix} = \begin{bmatrix} 1 & 0 & 0 & 0 \\ Y_{zz} & 1 & Y_{z\phi} & 0 \\ 0 & 0 & 1 & 0 \\ -Y_{\phi z} & 0 & -Y_{\phi\phi} & 1 \end{bmatrix} \cdot \begin{bmatrix} \tilde{E}_z \\ \tilde{H}_\phi^- \\ \tilde{E}_\phi \\ \tilde{H}_z^- \end{bmatrix} \quad (3.6)$$

where $\bar{\bar{Y}} = \bar{\bar{Z}}^{-1}$. Both transverse electric (TE_z) and transverse magnetic (TM_z) waves according the z -axis are considered which leads to a 4×4 ABCD matrix [4]. It should be noted that all entries of the ABCD matrix are dependent on both azimuthal mode number m and wavenumber k_z .

The total fields in each dielectric layer can be written in terms of outward and inward travelling cylindrical waves (Hankel functions of the first and second kind, see eqs. (3.2) and (3.3)) as follows,

$$\begin{bmatrix} \tilde{E}_z(\rho) \\ \tilde{H}_\phi(\rho) \\ \tilde{E}_\phi(\rho) \\ \tilde{H}_z(\rho) \end{bmatrix} = M(\rho) \cdot \begin{bmatrix} \alpha^- \\ \alpha^+ \\ \beta^- \\ \beta^+ \end{bmatrix} \quad (3.7a)$$

$$M(\rho) = \begin{bmatrix} H_m^{(1)}(k_{\rho n}\rho) & H_m^{(2)}(k_{\rho n}\rho) & 0 & 0 \\ -\frac{jk_n}{\eta_n k_{\rho n}} H_m^{(1)}(k_{\rho n}\rho) & -\frac{jk_n}{\eta_n k_{\rho n}} H_m^{(2)}(k_{\rho n}\rho) & -\frac{mk_z}{k_{\rho n}^2 \rho} H_m^{(1)}(k_{\rho n}\rho) & -\frac{mk_z}{k_{\rho n}^2 \rho} H_m^{(2)}(k_{\rho n}\rho) \\ -\frac{mk_z}{k_{\rho n}^2 \rho} H_m^{(1)}(k_{\rho n}\rho) & -\frac{mk_z}{k_{\rho n}^2 \rho} H_m^{(2)}(k_{\rho n}\rho) & \frac{j\eta_n k_n}{k_{\rho n}} H_m^{(1)}(k_{\rho n}\rho) & \frac{j\eta_n k_n}{k_{\rho n}} H_m^{(2)}(k_{\rho n}\rho) \\ 0 & 0 & H_m^{(1)}(k_{\rho n}\rho) & H_m^{(2)}(k_{\rho n}\rho) \end{bmatrix} \quad (3.7b)$$

Here, α and β are the amplitudes of the propagating, cylindrical TM and TE waves in the considered dielectric layer (i.e. the E_z and H_z components without the radial dependence), respectively. The superscripts + and – denote outward and inward cylindrical waves. The ABCD matrix can be solved for by relating the field expressions at the two boundaries (inner with coordinate ρ_{n-1} and outer with coordinate ρ_n) of the cylindrical transmission line:

$$\begin{bmatrix} \tilde{E}_z(\rho_n) \\ \tilde{H}_\phi(\rho_n) \\ \tilde{E}_\phi(\rho_n) \\ \tilde{H}_z(\rho_n) \end{bmatrix} = M(\rho_{n+1}) \cdot M^{-1}(\rho_n) \cdot \begin{bmatrix} \tilde{E}_z(\rho_{n-1}) \\ \tilde{H}_\phi(\rho_{n-1}) \\ \tilde{E}_\phi(\rho_{n-1}) \\ \tilde{H}_z(\rho_{n-1}) \end{bmatrix}. \quad (3.8)$$

It should be noted that the resulting ABCD matrix is block-diagonal for $k_z = 0$ or for $m = 0$. In other words, under normal incidence and for the fundamental ϕ -invariant mode, the TE_z and TM_z waves are uncoupled.

The ABCD matrix of the multilayer cylindrical metasurface structure is obtained by simply multiplying the ABCD matrices of the cascaded cylindrical transmission lines (dielectric layers) and the sheets. From it, the scattered field can be easily determined. One simply needs to solve the following matrix equation:

$$\begin{bmatrix} \tilde{E}_z^{inc}(\rho_N, m, k_z) + \tilde{E}_z^{scat}(\rho_N, m, k_z) \\ \tilde{H}_\phi^{inc}(\rho_N, m, k_z) + \tilde{H}_\phi^{scat}(\rho_N, m, k_z) \\ \tilde{E}_\phi^{inc}(\rho_N, m, k_z) + \tilde{E}_\phi^{scat}(\rho_N, m, k_z) \\ \tilde{H}_z^{inc}(\rho_N, m, k_z) + \tilde{H}_z^{scat}(\rho_N, m, k_z) \end{bmatrix} = \left\{ \prod_i \begin{bmatrix} A & B \\ C & D \end{bmatrix}_i \right\} \cdot \begin{bmatrix} \tilde{E}_z(\rho_1, m, k_z) \\ \tilde{H}_\phi(\rho_1, m, k_z) \\ \tilde{E}_\phi(\rho_1, m, k_z) \\ \tilde{H}_z(\rho_1, m, k_z) \end{bmatrix}. \quad (3.9)$$

Here, the ABCD matrices of the metasurface layers and the cylindrical transmission lines are symbolically written; ρ_1 and ρ_N are the inner and outer boundaries of the entire structure. Matrix equation (3.9) represents a system of 4 equations with 4 unknowns, where the unknowns are the amplitudes of \tilde{E}_z and \tilde{H}_z components at the inner and outer boundaries of the structure. The amplitudes of the ϕ -components are calculated using (3.3). From these EM field quantities, the scattered field can be found. For the EM field in the innermost layer the standing wave representation (i.e. the Bessel function representation) is applied in the eq. (3.2), thus we have only two unknown coefficients related to that layer. Therefore, the four unknowns in the linear system (3.9) are the amplitudes of the z -components of the scattered field and of the EM field in the innermost region.

In all the considered examples, the metasurface structures were excited with an incident plane wave:

$$E_z^{inc} = E_0 \sin \theta^{inc} \cos \alpha^{inc} \sum_{m=-\infty}^{\infty} (-j)^m J_m(k_0 \rho \sin \theta^{inc}) e^{-jm\phi} e^{jzk_0 \cos \theta^{inc}} \quad (3.10.a)$$

$$H_z^{inc} = \frac{E_0}{\eta_0} \sin \theta^{inc} \sin \alpha^{inc} \sum_{m=-\infty}^{\infty} (-j)^m J_m(k_0 \rho \sin \theta^{inc}) e^{-jm\phi} e^{jzk_0 \cos \theta^{inc}} \quad (3.10.b)$$

For $\alpha^{inc} = 0^\circ$ the excitation is a TM_z plane wave and for $\alpha^{inc} = 90^\circ$ it is a TE_z plane wave. Other types of excitations, like a line source, can be implemented in a straightforward manner (see e.g. [20]).

Note that the ABCD matrix approach can also be applied to cylindrical structures with only one metasurface layer, and the first set of results will consider such structures.

3.4 Algorithm for calculating Green's functions of cascaded metasurface structures

The described approach for modeling cascaded curved metasurfaces can be implemented into the algorithms for calculating Green's functions of multilayer structures. Previously we have developed a numerical algorithm for calculating the Green's function of multilayer structures of planar, circular-cylindrical and spherical type (so-called one-dimensional (1D) structures; the considered structures are homogeneous in two dimensions and they vary in one dimension only) [30], [31]. The algorithm starts with a 3D problem including some excitation currents (e.g. a chosen current distribution on a conformal microstrip patch element) and a multilayer structure (one of the three mentioned types). Then we transform the currents in the two dimensions (using suitable variation of the two-dimensional Fourier transformation) where the structure is invariant. Doing this, the current excitation can be interpreted in space as a current sheet, tube or shell around the multilayer structure. Then, the G1DMULT algorithm can be used to calculate the field solution of the multilayer structure in the spectral domain. The 3D field solution is obtained by a 2D inverse Fourier transform of the spectral solutions. The multilayer solution process is the same for all three geometries, i.e. the G1DMULT is very general. It can handle any number of layers of materials with complex permittivity and permeability. It calculates the field at several user specified observation points, due to several independent user-specified current sources at different locations.

The theoretical background of the G1DMULT algorithm is the Huygens's principle or, more precisely, the Love's equivalence theorem. The spatial harmonic problem is subdivided into one equivalent problem per layer where the field in each region is formulated as the field radiated by equivalent currents at the layer boundaries. For example, the E-field in the layer j is expressed as

$$\tilde{\mathbf{E}}_j = \tilde{\mathbf{G}}_{EJ}^{\text{hom}} \tilde{\mathbf{J}}_{j-1}^{eq} + \tilde{\mathbf{G}}_{EJ}^{\text{hom}} \tilde{\mathbf{J}}_j^{eq} + \tilde{\mathbf{G}}_{EM}^{\text{hom}} \tilde{\mathbf{M}}_{j-1}^{eq} + \tilde{\mathbf{G}}_{EM}^{\text{hom}} \tilde{\mathbf{M}}_j^{eq} + \tilde{\mathbf{G}}_{EJ}^{\text{hom}} \tilde{\mathbf{J}}_j^{\text{exci}} + \tilde{\mathbf{G}}_{EM}^{\text{hom}} \tilde{\mathbf{M}}_j^{\text{exci}} \quad (3.11)$$

where $\tilde{\mathbf{J}}_j^{eq}$ and $\tilde{\mathbf{M}}_j^{eq}$ are equivalent electric and magnetic current sheets at boundary j , $\tilde{\mathbf{J}}_j^{\text{exci}}$ and $\tilde{\mathbf{M}}_j^{\text{exci}}$ are excitation electric and magnetic currents in layer j (if any), and $\tilde{\mathbf{G}}_{EJ}^{\text{hom}}$ and $\tilde{\mathbf{G}}_{EM}^{\text{hom}}$ are the Green's functions of the homogeneous structure. By using the equivalence principle the equation (3.11) can be expressed in terms of the unknown tangential EM field components at the boundary j between layers j and $j+1$ and known excitation currents. The boundary conditions that the tangential E - and H - fields are continuous at the layer boundaries give 4 linear equations per boundary. The tangential E - and H -fields are evaluated by solving the system of $4 \cdot N_{\text{boundary}}$ equations with $4 \cdot N_{\text{boundary}}$ unknowns, where N_{boundary} is the number of boundaries present in the multilayer structure. After they have been determined, the total E - and H -fields at any desired location can be found by using the equivalent principle.

The metasurface layers can also be included into the G1DMULT algorithm. In other words, the modified G1DMULT algorithm calculates the EM field distribution inside and outside multilayer structure that contains metasurface sheets. The boundary containing the metasurface sheet is treated as a boundary at which the equivalent currents are discontinuous. The boundary condition given by:

$$, \quad \hat{n} \times \tilde{\mathbf{E}} = \hat{n} \times \left[\bar{\bar{\mathbf{Z}}} \cdot (\hat{n} \times (\tilde{\mathbf{H}}^+ - \tilde{\mathbf{H}}^-)) \right] \quad (3.12)$$

which is transformed into the boundary condition for the equivalent currents in the spectral domain:

$$-\tilde{\mathbf{M}}_j^{eq} = \left[\bar{\bar{\mathbf{Z}}} \cdot (\tilde{\mathbf{J}}_{j+}^{eq} - \tilde{\mathbf{J}}_{j-}^{eq}) \right] \quad (3.13)$$

Note that the metasurface layer requires definition of two boundaries (with zero distance between them) at which the equivalent magnetic current is continuous and the equivalent electric current is discontinuous according the eq. (3.13). In the same way the discontinuity of the electric field (loop or slotted metasurface elements) is considered.

The opaque (reflective) metasurface can be treated as non-penetrable boundary with impedance boundary condition:

$$\hat{n} \times \tilde{\mathbf{E}}^+ = \hat{n} \times \left[\bar{\bar{\mathbf{Z}}} \cdot (\hat{n} \times \tilde{\mathbf{H}}^+) \right] \quad (3.14)$$

or, by using equivalent currents, the opaque impedance boundary condition is equal

$$\tilde{\mathbf{M}}^{eq} = -\hat{n} \times \left(\bar{\bar{\mathbf{Z}}} \cdot \tilde{\mathbf{J}}^{eq} \right) \quad (3.15)$$

According the impedance boundary condition the system of equations inside the G1DMULT algorithm is modified as shown in Figure 3.2. By this, for each spectral component only two unknowns (related to the two surface components of the equivalent magnetic current) are associated with the impedance boundary; the contribution of other two unknowns (two surface components of the equivalent electric current) are taken into account using eq. (3.15).

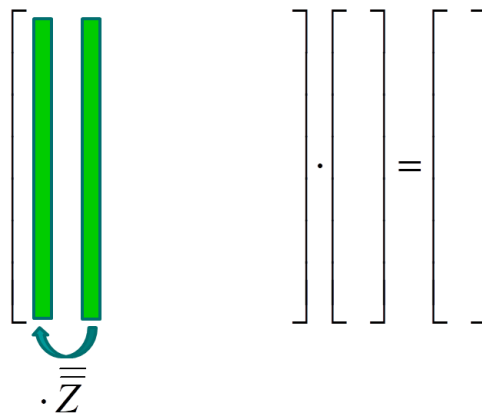


Fig 3.2. Modification of the system of equations inside the G1DMULT algorithm for EM problems containing an opaque metasurface.

3.5 Exact surface impedance vs. approximations

The first set of results compares how different ways of calculating metasurface reactance affect the overall results. We start with case 1 where we calculated the field scattered by a dielectric cylinder covered with vertical strips under TM_z incidence, as shown in Fig. 3.3. In this case, the metasurface acts as an inductive reactance.

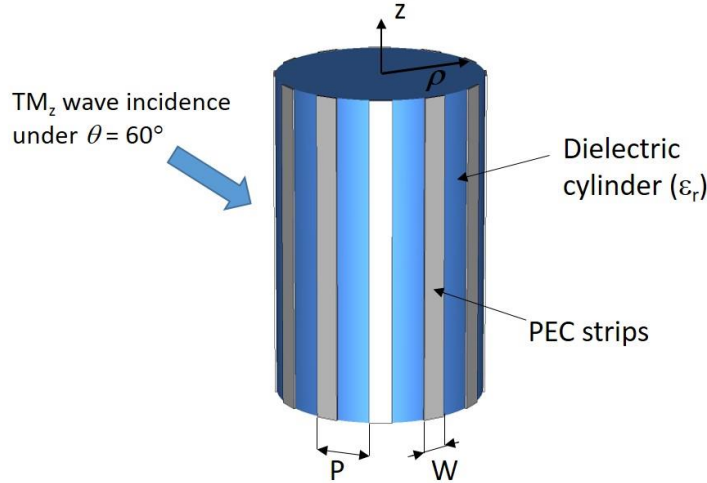


Fig. 3.3. Dielectric cylinder with periodic vertical PEC strips.

The dielectric cylinder considered is made of Teflon with $\epsilon_r = 2.1$, $\tan \delta = 0.00015$, and has a radius $\rho = 12.7$ mm. The strip width is $W = 3$ mm and the period of the strips is $P_\phi = 9.97$ mm ($0.33 \lambda_0$ at 10 GHz). The incident wave is TM_z polarized with incident angle $\theta = 60^\circ$. In the past, such cylinders were manufactured and their scattering properties measured at Chalmers University of Technology [26].

First, we tested the proposed analysis method for the case where the sheet impedance tensor $\bar{\bar{Z}}$ was calculated using a moment method code for cylindrical periodic structures [20]. As shown in Fig. 3.4 there is excellent agreement between the calculated results obtained using the proposed method and the exact MoM code for cylindrical structures. There is also good agreement with the measurements of the experimental prototype, even with its fabrication tolerances.

Further, it is valuable to compare how different approximations for the sheet impedance tensor affect the results obtained using the proposed analysis approach. Two separate approximations were considered, and compared to the results obtained for the sheet impedance tensor calculated using the cylindrical MoM code. First, a MoM code for planar (flat) periodic structures was used to extract the impedance tensor at $\theta = 60^\circ$ incidence. Next, the following approximate expression for planar strips [27] was used for a TM_z incident wave:

$$Z_{zz}^{approx}(k_z) = j \frac{k_0 \eta_0}{2\pi} P_\phi \log \left(\csc \left(\frac{\pi W}{2P_\phi} \right) \right) \left(1 - \frac{k_z^2}{k_{eff}^2} \right) \quad (3.16.a)$$

$$Z_{\phi\phi}^{approx}(k_z) = -j \frac{\pi \eta_0}{P_\phi k_0 (1 + \epsilon_r)} \left[\log \left(\csc \left(\frac{\pi W}{2P_\phi} \right) \right) \left(1 - \frac{k_z^2}{k_{eff}^2} \right) \right]^{-1} \quad (3.16.b)$$

where k_{eff} is equal $k_{eff}^2 = k_0^2 \cdot (\epsilon_r + 1)/2$. Note that the angle of incidence of the plane wave determines the spectral variable $k_z = k_0 \cos \theta$.

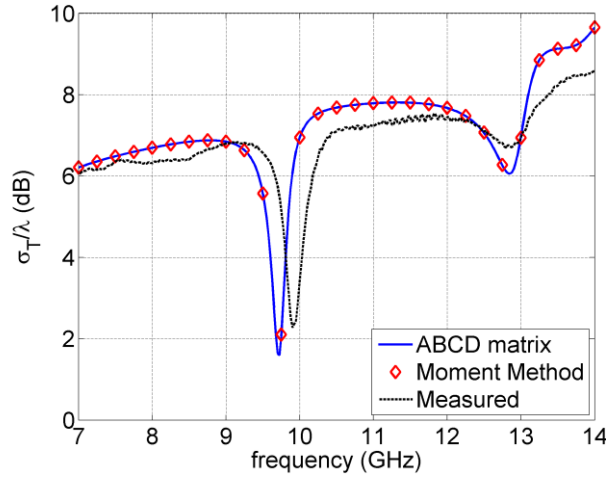


Fig. 3.4. Total scattering width of a dielectric cylinder loaded with periodic axial strips.

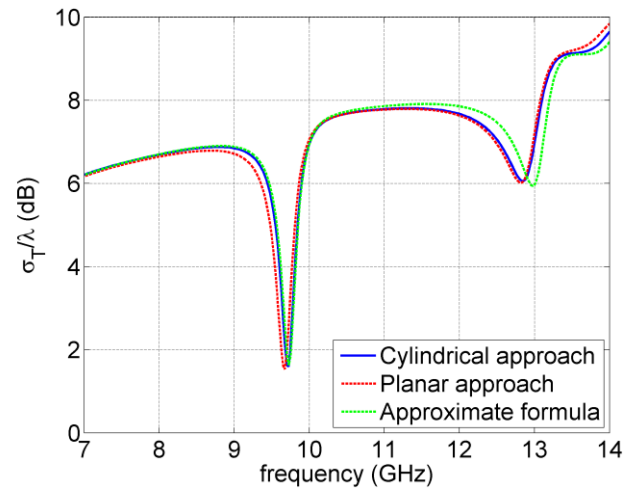
Fig. 3.5.a shows that the approximations cause a frequency shift in the calculated scattering results. This frequency shift occurs because the rigorously obtained impedance tensor depends on the azimuthal mode. In contrast, the two approximations estimate the admittance tensor to be constant with respect to mode order m . This can be seen from the calculated surface reactances given in Fig. 3.5.b. at 12 GHz.

The situation is quite different for circumferential strips (Fig. 3.6.). The periodicity of the strips is $P_z = 8$ mm ($0.27 \lambda_0$ at 10 GHz), and all other parameters are kept the same as in the previous example. The incident wave was TE_z polarized with incident angle $\theta = 60^\circ$. Since we are considering the surface impedance in the spectral domain, we can modify the approximate planar surface impedance formulas (3.16) to include the propagation constant in the ϕ -direction $k_\phi = m/\rho$:

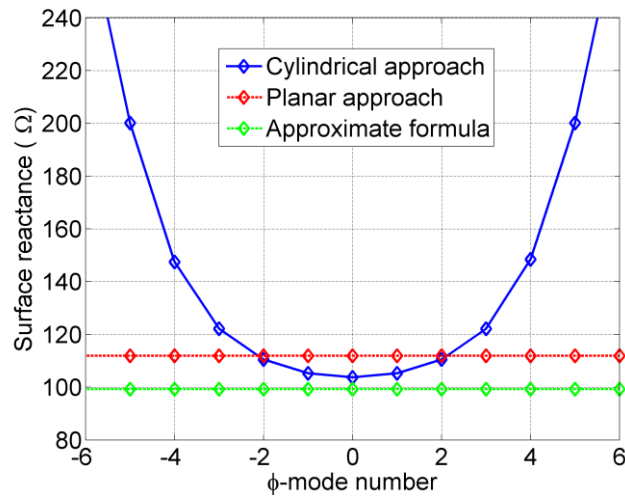
$$Z_{zz}^{approx}(m) = -j \frac{\pi \eta_0}{P_z k_0 (1 + \epsilon_r)} \left[\log \left(\csc \left(\frac{\pi W}{2P_z} \right) \right) \left(1 - \frac{m^2}{\rho_{strips}^2 k_{eff}^2} \right) \right]^{-1} \quad (3.17.a)$$

$$Z_{\phi\phi}^{approx}(m) = j \frac{k_0 \eta_0}{2\pi} P_z \log \left(\csc \left(\frac{\pi W}{2P_z} \right) \right) \left(1 - \frac{m^2}{\rho_{strips}^2 k_{eff}^2} \right) \quad (3.17.b)$$

Note that the approximate formulas only have a dependence on the phase variation along the strips. Therefore, there is no dependency on incident angle θ in eqs. (3.17).



(a)



(b)

Fig. 3.5. Comparison of calculated total scattering width of a dielectric cylinder loaded with periodic axial strips. The metasurface impedance is calculated in three different ways; (a) calculated total scattering width, (b) dependency of surface reactance Z_{zz} on angular mode at 12 GHz.

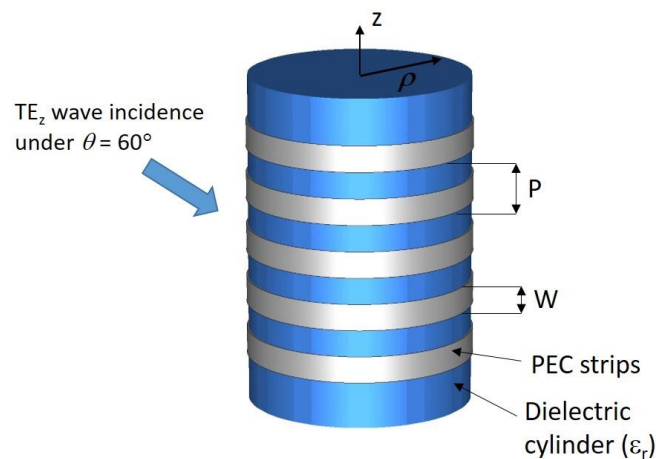
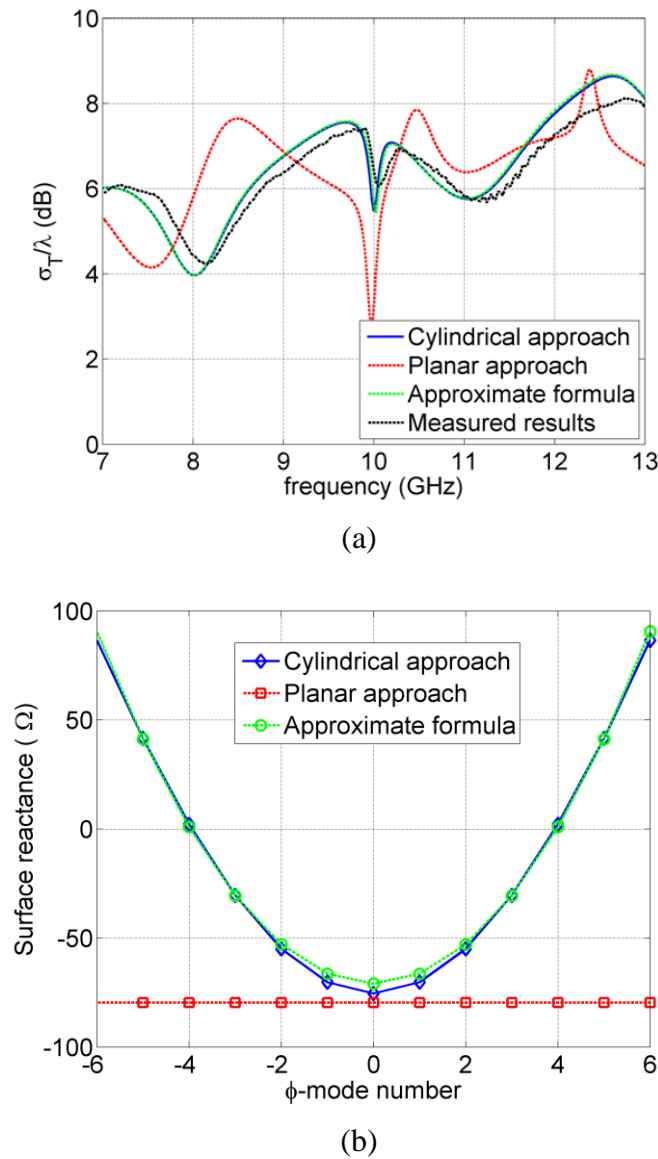


Fig. 3.6. Dielectric cylinder with periodic circumferential PEC strips.

In this case, the surface impedance varies significantly with angular mode number (see Fig. 3.7.b). Therefore, it is not possible to accurately approximate the surface impedance with the value obtained from the equivalent planar case. However, the approximate expressions (3.17.a) and (3.17.b) closely predict the azimuthal variation of surface impedance. Consequently, there is close agreement between the results in which the impedance tensor is determined using a cylindrical MoM code, the approximate expressions (3.17) in which the azimuthal variation is taken into account, and measurements (see Fig. 3.7.a). One could also include the azimuthal propagation constant into the analysis of the equivalent planar structure. However, the equivalent incident angle will be different for each frequency and spectral variable m (i.e. the equivalent incident angle is equal to $\arcsin(m/(\rho_{strips} k_0))$), so it would be extremely time consuming to calculate the surface impedance using commercial EM solvers in this way.

**Fig. 3.7.** Comparison of calculated total scattering width of a dielectric cylinder loaded with periodic circumferential strips. The metasurface impedance is calculated in three different

ways; (a) calculated total scattering width, (b) dependency of surface reactance $Z_{\phi\phi}$ on angular mode at 12 GHz.

3.6 Selection of optimal elements for cylindrical metasurfaces

To further verify the proposed method and indicate how different realizations of the metasurface effect the results we will consider the mantle cloak example discussed in [19] and [20]. The structure considered is a PEC cylinder of radius 10 mm, with a dielectric shell of outer radius 10.5 mm and permittivity $\epsilon_r = 20$ shown in Fig. 3.8. The operating frequency is 3 GHz, therefore the radius of the PEC cylinder is $0.1\lambda_0$. The first step in designing a mantle cloak is to estimate the needed metasurface impedance. Initially we assume that it has a constant value, i.e. that it does not change for different ϕ -modes. By performing a parametric sweep over sheet impedances and calculating the minimum total scattering width, it was determined that the optimal value for the metasurface reactance is -12.23Ω . This is consistent with the results presented in [19]. We considered two realizations of the capacitive metascreen. The first realization consists of square metallic patches shown in Fig. 3.8 (side width of $W = 10.6$ mm, and gap between the patches of $P - W = 0.39$ mm). The second realization consists of Jerusalem crosses (Fig.3.8) with side dimension $W_J = 9.382$ mm, line width $t_J = 0.625$ mm, T-section width $T_J = 3.127$ mm, and a gap between the crosses of $P_J - W_J = 1.61$ mm. In both cases, there are 6 elements along the ϕ -direction, i.e. period is $0.37 \lambda_0$ at the central frequency. The values of surface impedance tensor are calculated using a MoM code for cylindrical periodic structures [26]. It should be noted that the dimensions of both structures were determined by finding those that resulted in minimum total scattering width at 3 GHz.

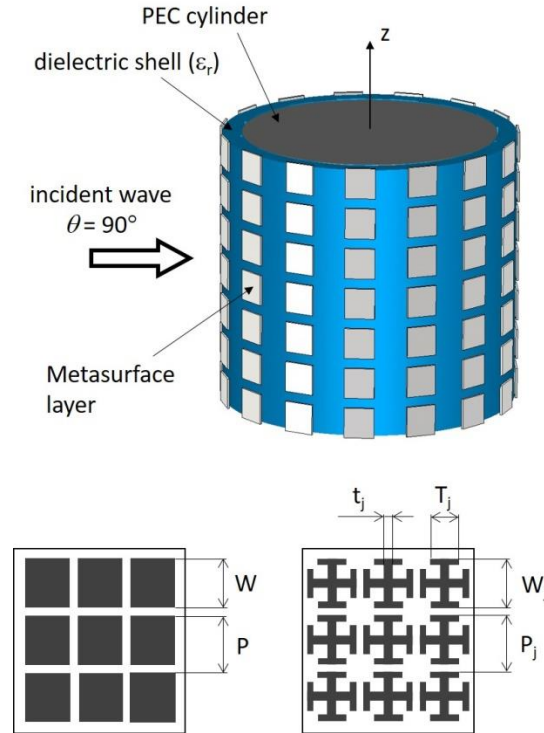


Fig. 3.8. Mantle cloak realization on a PEC cylinder with dielectric shell. Cloak is a metasurface based on square PEC patches or PEC patches in the shape of Jerusalem crosses.

We have compared in Figure 3.9 the total scattering width and the bandwidth properties of the cylindrical object with the two considered metasurface realizations. The incidence wave is a TM_z polarized normally incident plane wave (i.e. $k_z = k_0 \cos \theta = 0$). Fig. 3.9. also shows the result for a mantle cloak with constant metasurface reactance equal to $-12.23 \, \Omega$, and the total scattering width of a PEC cylinder of radius 10.0 mm (i.e. of the hidden object) in order to establish the bandwidth of the considered cloaks. It can be seen that the patch metasurface is superior since it provides higher scattering reduction and larger bandwidth of operation. In addition, the patch metasurface outperforms the metasurface cloak with a constant sheet reactance. In order to explain why the patch metasurface is superior in comparison with the other structures, we have plotted the variation of the surface reactance with mode order m for all three considered cases. From Figure 3.10, it is evident that all three cases have approximately the same reactance for the $m=0$ mode (mode with no ϕ -variation). However, the surface impedance of the Jerusalem crosses and patches differs for the higher-order m modes. Specifically, the magnitude of the reactance is larger for patches than for Jerusalem crosses with increasing m . In order to appreciate the importance of tailoring the mode order variation of the surface reactance, we have calculated an optimum ϕ -variation for the surface reactance: the reactance that gives zero total scattering width for each ϕ mode. This optimal impedance Z_{zz}^{opt} can be found by setting each spectral-domain component of the scattered field in eq. (3.9) equal to zero, which results in a characteristic equation for each spectral component of the surface impedance:

$$Z_{zz}^{opt}(m) = j\eta_0 \left(\frac{J'_m(k_0\rho_2)}{J_m(k_0\rho_2)} - \sqrt{\epsilon_{r,1}} \frac{H_m^{(1)}(k_1\rho_1)H_m'^{(2)}(k_1\rho_2) - H_m^{(2)}(k_1\rho_1)H_m'^{(1)}(k_1\rho_2)}{H_m^{(1)}(k_1\rho_1)H_m^{(2)}(k_1\rho_2) - H_m^{(2)}(k_1\rho_1)H_m^{(1)}(k_1\rho_2)} \right)^{-1} \quad (3.18)$$

The optimum profile is also plotted in Fig. 3.10. It can be seen that the impedance profile of the patch metasurface closely resembles the optimal case. This example illustrates the importance of incorporating the spectral variation of a surface impedance into the design process.

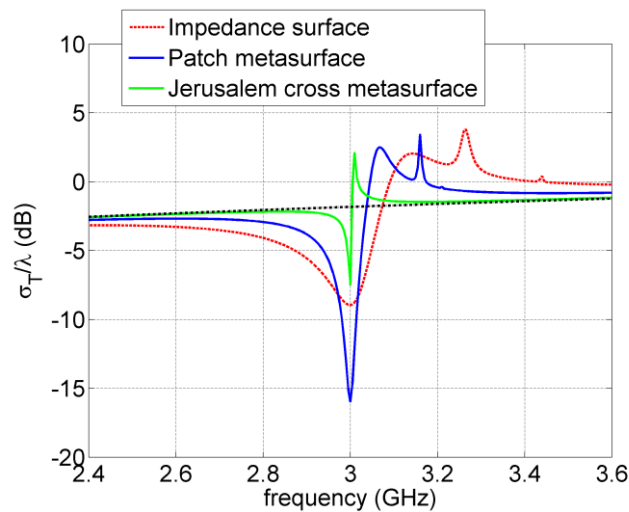


Fig. 3.9. Comparison of calculated total scattering width of a dielectric cylinder loaded with metasurface. Total scattering width of a PEC cylinder of radius 10 mm is shown with black dotted line.

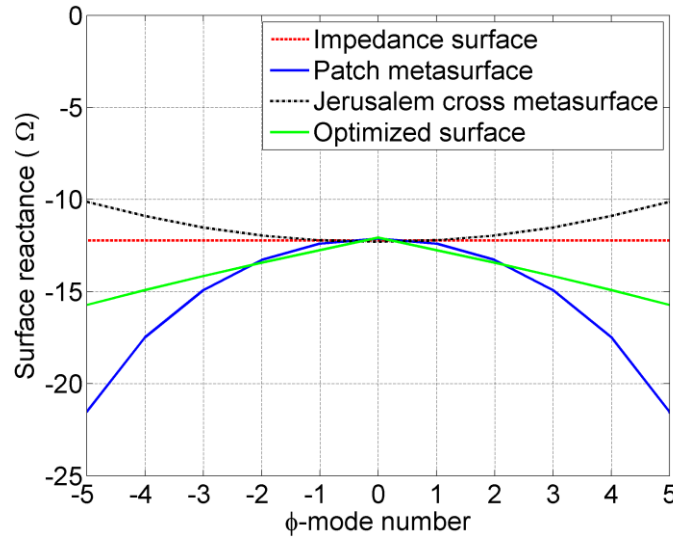


Fig 3.10. Dependency of the surface reactance of a dielectric cylinder loaded with metasurface on angular mode at 3 GHz.

3.7 Influence of mutual coupling between metasurface layers

As a final example, let us consider a two-layer cylindrical metasurface structure built from vertical strips. The intent of this example is to verify the proposed method on a multilayer design, and to investigate how close patterned sheets can be placed next to each other in order to still accurately model the structure using the ABCD transmission matrix approach. The approximation in the analysis method is that only the propagating (lowest-order) ϕ -modes are taken into account in the ABCD transmission matrix formulation. In other words, it is assumed that coupling between different metasurface layers occurs only through the considered propagating cylindrical mode with $\exp(jm\phi)$ variation, while higher-order Floquet modes (i.e. evanescence modes) are neglected. The higher-order Floquet modes are defined with azimuthal variation of the cylindrical mode $m_l = m + l \cdot N_\phi$, $l \neq 0$, where N_ϕ is the number of periodic elements in ϕ -direction (strips in this case) and l is the Floquet-mode index. An equivalent assumption is commonly used in the planar case [32], [33].

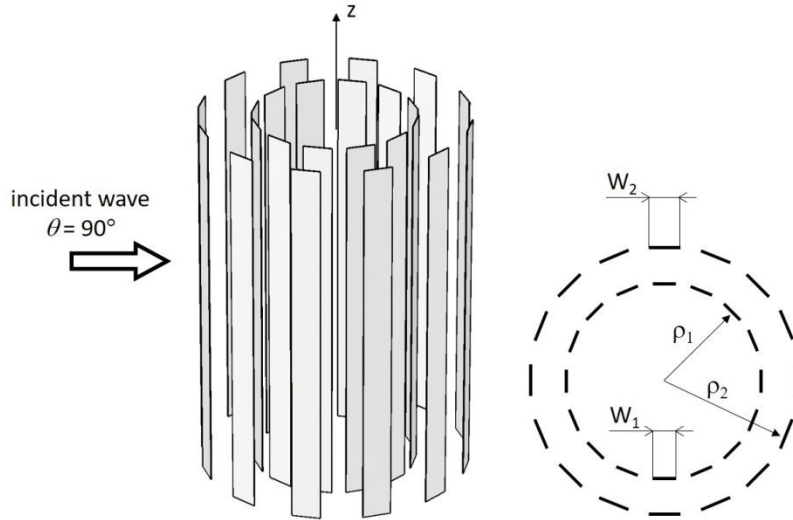
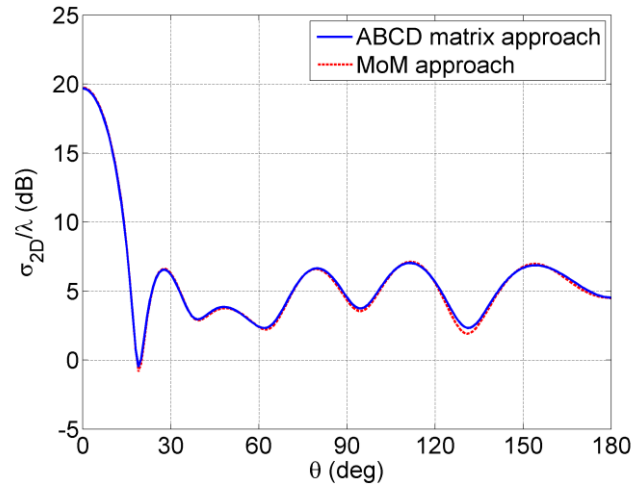


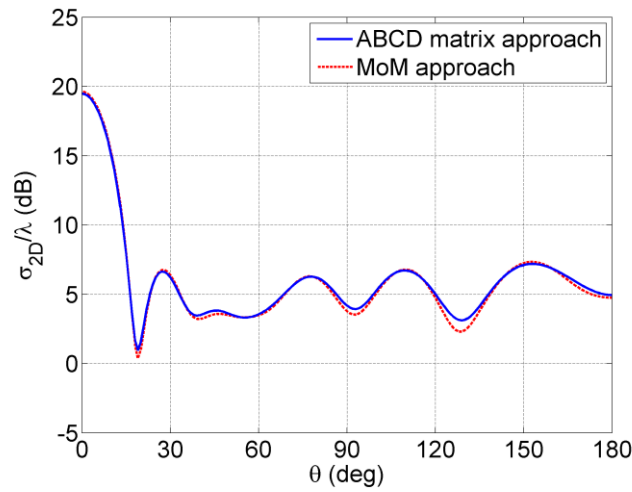
Fig. 3.11. Two-layer periodic strip-grid cylindrical structure.

In this example, we fixed the outer radius of the structure ($\rho_2 = 114.6$ mm) and the number and width of the strips in each layer ($N_{\phi,1} = N_{\phi,2} = 24$, $W_1 = W_2 = 1.15$ mm), see Fig. 3.11. The working frequency was set to $f = 4.0$ GHz (i.e. strip period is $0.4 \lambda_0$) and the excitation to a TM_z normally incident plane wave. The inner radius was selected to be 99.6 mm, 103.3 mm and 107.1 mm. Therefore, the distance between layers was 0.2λ , 0.15λ and 0.1λ , respectively. In Fig. 3.12, the calculated bistatic scattering width is plotted. There is good agreement between the two methods, the ABCD transmission matrix approach and the exact MoM code, even for close separation distances between the patterned sheets. The incoming plane wave is represented with 21 azimuthal modes, as suggested by the expression $N_{\phi}^{\max} \approx (2\pi/\lambda_0)\rho_2$.

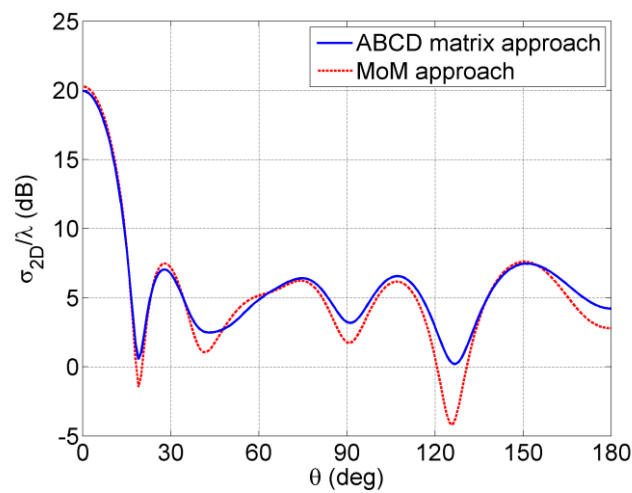
In order to estimate the distance at which higher-order evanescent modes should be taken into account, we calculated the EM field scattered by one strip layer and plotted the amplitude decay of the evanescent modes as a function of distance from the periodic strip grid (see Fig. 3.13; the radial electromagnetic field variation is calculated using eq. (3.2)). We considered the field variation in the outside region; the amplitude of each mode is calculated using the exact MoM program for cylindrical structures. The dominant $m = 0$ mode is considered, thus the higher-order Floquet modes are defined with $m = l \cdot N_{\phi}$, $l = 1, 2, 3$. A comparison of Figures 3.12 and 3.13, reveals that the analysis can be improved with the inclusion of the ABCD matrices that account for higher-order (evanescent) modes for dielectric thicknesses where the higher-order modes have relative amplitudes larger than approximately 0.1 at the position of neighboring metasurface layer. This can be done in the same way where both TE and TM modes are considered, as in the presented analysis method, see eqs. (3.6)-(3.9).



(a)



(b)



(c)

Fig. 3.12. Scattered field from the two-layer periodic strip-grid structure; distance between two metasurface layers is: (a) 0.2λ , (b) 0.15λ , (c) 0.1λ .

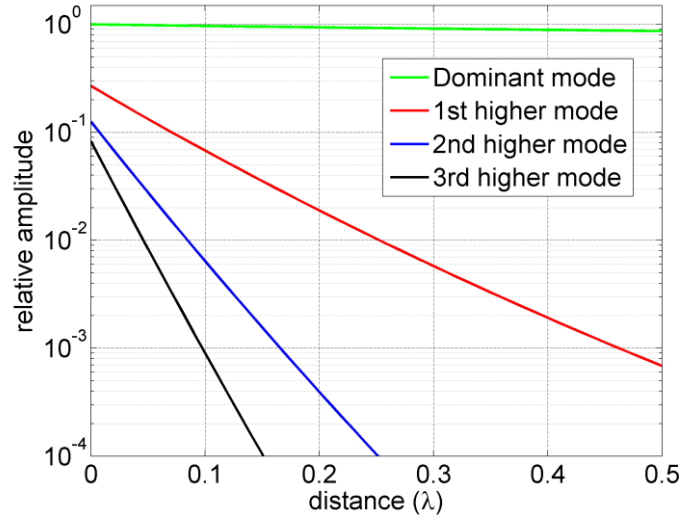


Fig. 3.13. Decay of the amplitude of evanescent modes as a function of the distance from the periodic strip grid.

3.8 Analysis of cascaded spherical metasurface structures

In this section we will give the procedure how the considered analysis method is applied to spherical metasurface structures. Like in the cylindrical case the solution procedure makes use of the Fourier transformation technique. Since the problem is described in spherical coordinate system, we use the vector Legendre transformation in θ and ϕ directions, defined by [34], [30]:

$$\tilde{\mathbf{J}}(r, n, m) = \frac{1}{\sqrt{2\pi S(n, m)}} \iint_{-\pi}^{\pi} \tilde{\mathbf{L}}(n, m, \theta) \mathbf{J}(r, \theta, \phi) \sin \theta e^{-jm\phi} d\theta d\phi \quad (3.19.a)$$

$$\mathbf{J}(r, \theta, \phi) = \sum_{m=-\infty}^{\infty} \sum_{n=|m|}^{\infty} \frac{1}{\sqrt{2\pi S(n, m)}} \tilde{\mathbf{L}}(n, m, \theta) \tilde{\mathbf{J}}(r, n, m) e^{jm\phi} \quad (3.19.b)$$

$$\tilde{\mathbf{L}}(n, m, \theta) = \begin{bmatrix} P_n^{|m|}(\cos \theta) \sqrt{n(n+1)} & 0 & 0 \\ 0 & \frac{\partial P_n^{|m|}(\cos \theta)}{\partial \theta} & -jm P_n^{|m|}(\cos \theta) \\ 0 & \frac{jm P_n^{|m|}(\cos \theta)}{\sin \theta} & \frac{\partial P_n^{|m|}(\cos \theta)}{\partial \theta} \end{bmatrix} \quad (3.19.c)$$

$$S(n, m) = \frac{2n(n+1)(n+|m|)!}{(2n+1)(n-|m|)!} \quad (3.19.d)$$

By applying the vector Legendre transformation, the 3D excitations are transformed into harmonic current shells. If the source is infinitely thin in r -direction, we get one discrete current shell per source, otherwise we get a continuous distribution of current shells in r -direction. The E- and H-fields induced by the harmonic current sources have the same harmonic variations in θ and ϕ as the source. Therefore, only the field variation in the direction perpendicular to the boundaries is unknown, and we have a harmonic one-dimensional (1D) field problem. In this way, the spectral domain problem is interpreted as a 1D spatial domain problem consisting of 1D multilayer structure and harmonic 1D sources in the form of current shells.

The expressions for the field distribution can be determined by assuming the radial component of the electric and magnetic potential in the form [35]:

$$A_r(r, \theta, \phi) = \sum_{m=-\infty}^{\infty} \sum_{n=|m|}^{\infty} B_2(n, m) \hat{H}_n^{(2)}(kr) P_n^{|m|}(\cos \theta) e^{jm\phi} \quad \text{for } r > r_s \quad (3.20.a)$$

$$F_r(r, \theta, \phi) = \sum_{m=-\infty}^{\infty} \sum_{n=|m|}^{\infty} D_2(n, m) \hat{H}_n^{(2)}(kr) P_n^{|m|}(\cos \theta) e^{jm\phi} \quad \text{for } r > r_s \quad (3.20.b)$$

$$A_r(r, \theta, \phi) = \sum_{m=-\infty}^{\infty} \sum_{n=|m|}^{\infty} A_1(n, m) \hat{J}_n(kr) P_n^{|m|}(\cos \theta) e^{jm\phi} \quad \text{for } 0 \leq r < r_s \quad (3.20.c)$$

$$F_r(r, \theta, \phi) = \sum_{m=-\infty}^{\infty} \sum_{n=|m|}^{\infty} C_1(n, m) \hat{J}_n(kr) P_n^{|m|}(\cos \theta) e^{jm\phi} \quad \text{for } 0 \leq r < r_s, \quad (3.20.d)$$

where \hat{J}_n and $\hat{H}_n^{(2)}$ denote the Schelkunoff type of the spherical Bessel and Hankel functions

$$\hat{J}_n(kr) = \sqrt{\frac{\pi kr}{2}} J_{n+1/2}(kr) \quad \hat{H}_n^{(2)}(kr) = \sqrt{\frac{\pi kr}{2}} H_{n+1/2}^{(2)}(kr). \quad (3.21)$$

Here we have assumed that the source is located at a sphere of radius r_s in a homogeneous space. It can be shown that the field distribution in the spectral domain has a form

$$\tilde{\mathbf{E}}(r, n, m) = \begin{bmatrix} \tilde{E}_r \\ \tilde{E}_\theta \\ \tilde{E}_\phi \end{bmatrix} = \begin{bmatrix} \frac{\eta \sqrt{n(n+1)}}{jkr^2} B_2(n, m) \hat{H}_n^{(2)}(kr) \\ \frac{\eta}{jr} B_2(n, m) \hat{H}_n^{(2)'}(kr) \\ \frac{1}{r} D_2(n, m) \hat{H}_n^{(2)}(kr) \end{bmatrix} \quad \text{for } r > r_s \quad (3.22.a)$$

$$\tilde{\mathbf{H}}(r, n, m) = \begin{bmatrix} \tilde{H}_r \\ \tilde{H}_\theta \\ \tilde{H}_\phi \end{bmatrix} = \begin{bmatrix} \frac{\sqrt{n(n+1)}}{j\eta kr^2} D_2(n, m) \hat{H}_n^{(2)}(kr) \\ \frac{1}{j\eta r} D_2(n, m) \hat{H}_n^{(2)'}(kr) \\ -\frac{1}{r} B_2(n, m) \hat{H}_n^{(2)}(kr) \end{bmatrix} \quad \text{for } r > r_s \quad (3.22.b)$$

$$\tilde{\mathbf{E}}(r, n, m) = \begin{bmatrix} \tilde{E}_r \\ \tilde{E}_\theta \\ \tilde{E}_\phi \end{bmatrix} = \begin{bmatrix} \frac{\eta\sqrt{n(n+1)}}{jkr^2} A_1(n, m) \hat{J}_n(kr) \\ \frac{\eta}{jr} A_1(n, m) \hat{J}_n'(kr) \\ \frac{1}{r} C_1(n, m) \hat{J}_n(kr) \end{bmatrix} \quad \text{for } 0 \leq r < r_s \quad (3.22.c)$$

$$\tilde{\mathbf{H}}(r, n, m) = \begin{bmatrix} \tilde{H}_r \\ \tilde{H}_\theta \\ \tilde{H}_\phi \end{bmatrix} = \begin{bmatrix} \frac{\sqrt{n(n+1)}}{j\eta kr^2} C_1(n, m) \hat{J}_n(kr) \\ \frac{1}{j\eta r} C_1(n, m) \hat{J}_n'(kr) \\ -\frac{1}{r} A_1(n, m) \hat{J}_n(kr) \end{bmatrix} \quad \text{for } 0 \leq r < r_s \quad (3.22.d)$$

Therefore, in order to analyze cascaded spherical metasurface structures one can modify the solution procedure for cylindrical structures in the following way. The spectral-domain ABCD matrix of a constitutive sheet of the spherical metasurface is given by the following expression:

$$\begin{bmatrix} \tilde{E}_\theta \\ \tilde{H}_\phi^+ \\ \tilde{E}_\phi \\ \tilde{H}_\theta^+ \end{bmatrix} = \begin{bmatrix} 1 & 0 & 0 & 0 \\ -Y_{\theta\theta} & 1 & -Y_{\theta\phi} & 0 \\ 0 & 0 & 1 & 0 \\ Y_{\phi\theta} & 0 & Y_{\phi\phi} & 1 \end{bmatrix} \cdot \begin{bmatrix} \tilde{E}_\theta \\ \tilde{H}_\phi^- \\ \tilde{E}_\phi \\ \tilde{H}_\theta^- \end{bmatrix}, \quad (3.23)$$

where both transverse electric (TE_r) and transverse magnetic (TM_r) waves according the radial direction are considered, which leads to a 4×4 ABCD matrix [4]. Like in the cylindrical case, the subscripts denote the corresponding components of the electric field and surface current, respectively. From the equation (3.22) it follows that the TM_r waves contain E_θ , H_ϕ and E_r spectral components, while the TE_r waves contain H_θ , E_ϕ and H_r spectral components. It should be noted that all entries of the ABCD matrix are dependent on both elevation and azimuthal mode numbers n and m .

The total fields in each dielectric layer can be written in terms of outward and inward travelling spherical waves (described with Schelkunoff Hankel functions of the first and second kind, see eq. (3.22)) as follows,

$$\begin{bmatrix} \tilde{E}_\theta(r) \\ \tilde{H}_\phi(r) \\ \tilde{E}_\phi(r) \\ \tilde{H}_\theta(r) \end{bmatrix} = M(r) \cdot \begin{bmatrix} \alpha^- \\ \alpha^+ \\ \beta^- \\ \beta^+ \end{bmatrix} \quad (3.24a)$$

$$M(r) = \begin{bmatrix} \frac{1}{r} \hat{H}_m^{(1)'}(k_n r) & \frac{1}{r} \hat{H}_m^{(2)'}(k_n r) & 0 & 0 \\ -\frac{j}{\eta_n} \frac{1}{r} \hat{H}_m^{(1)}(k_n r) & -\frac{j}{\eta_n} \frac{1}{r} \hat{H}_m^{(2)}(k_n r) & 0 & 0 \\ 0 & 0 & \frac{1}{r} \hat{H}_m^{(1)}(k_n r) & \frac{1}{r} \hat{H}_m^{(2)}(k_n r) \\ 0 & 0 & -\frac{j}{\eta_n} \frac{1}{r} \hat{H}_m^{(1)'}(k_n r) & -\frac{j}{\eta_n} \frac{1}{r} \hat{H}_m^{(2)'}(k_n r) \end{bmatrix} \quad (3.24b)$$

Here, α and β are the amplitudes of the propagating, spherical TM_r and TE_r waves in the considered dielectric layer (i.e. the E_θ and E_ϕ components without the radial dependence), respectively. The superscripts + and - denote outward and inward spherical waves. The ABCD matrix can be solved for by relating the field expressions at the two boundaries (inner with coordinate r_{n-1} and outer with coordinate r_n) of the spherical transmission line:

$$\begin{bmatrix} \tilde{E}_\theta(r_n) \\ \tilde{H}_\phi(r_n) \\ \tilde{E}_\phi(r_n) \\ \tilde{H}_\theta(r_n) \end{bmatrix} = M(r_{n+1}) \cdot M^{-1}(r_n) \cdot \begin{bmatrix} \tilde{E}_\theta(r_{n-1}) \\ \tilde{H}_\phi(r_{n-1}) \\ \tilde{E}_\phi(r_{n-1}) \\ \tilde{H}_\theta(r_{n-1}) \end{bmatrix} \quad (3.25)$$

It should be noted that the transmission-line part of the ABCD matrix is block-diagonal. In other words, if the $Y_{\theta\phi}$ and $Y_{\phi\theta}$ elements of the admittance matrix of each metasurface layer are equal to zero, then the TE_r and TM_r waves are uncoupled in the whole cascaded metasurface structure.

The ABCD matrix of the multilayer spherical metasurface structure is obtained by simply multiplying the ABCD matrices of the cascaded cylindrical transmission lines (dielectric layers) and the sheets. From it, the scattered field can be easily determined. One simply needs to solve the following matrix equation:

$$\begin{bmatrix} \tilde{E}_\theta^{inc}(r_N, n, m) + \tilde{E}_\theta^{scat}(r_N, n, m) \\ \tilde{H}_\phi^{inc}(r_N, n, m) + \tilde{H}_\phi^{scat}(r_N, n, m) \\ \tilde{E}_\phi^{inc}(r_N, n, m) + \tilde{E}_\phi^{scat}(r_N, n, m) \\ \tilde{H}_\theta^{inc}(r_N, n, m) + \tilde{H}_\theta^{scat}(r_N, n, m) \end{bmatrix} = \left\{ \prod_i \begin{bmatrix} A & B \\ C & D \end{bmatrix}_i \right\} \cdot \begin{bmatrix} \tilde{E}_\theta(r_1, n, m) \\ \tilde{H}_\phi(r_1, n, m) \\ \tilde{E}_\phi(r_1, n, m) \\ \tilde{H}_\theta(r_1, n, m) \end{bmatrix}. \quad (3.26)$$

Here, the ABCD matrices of the metasurface layers and the spherical transmission lines are symbolically written; r_1 and r_N are the inner and outer boundaries of the entire structure. Matrix equation (3.26) represents a system of 4 equations with 4 unknowns: the amplitudes of

\tilde{E}_θ and \tilde{E}_ϕ components at the inner and outer boundaries of the structure. The amplitudes of the H -components of the electromagnetic field are calculated using (3.22).

As an example, let us consider a problem of scattering of EM waves from an impedance sphere. Assumed radius of the sphere is $kr_1 = 5$, and the selected value of surface impedance is $Z = j \cdot 0.15 \eta_0$. The intent of this example is to verify the developed spherical version of the code. The results are given in Figures 3.14 and 3.15. We considered two cases – when the spherical impedance surface is described with opaque and transparent surface impedance boundary conditions, respectively. In the first case (Fig. 3.14) we also compared the results of the developed multilayer&multi-metasurface code with the analytically calculated results given in [36]. It can be seen that there is perfect agreement between two sets of calculated results (further verification of the spherical version of the code will be given in Chapter 5). Furthermore, two different versions of impedance surface, opaque and transparent, give similar scattering radiation patterns (Fig 3.15).

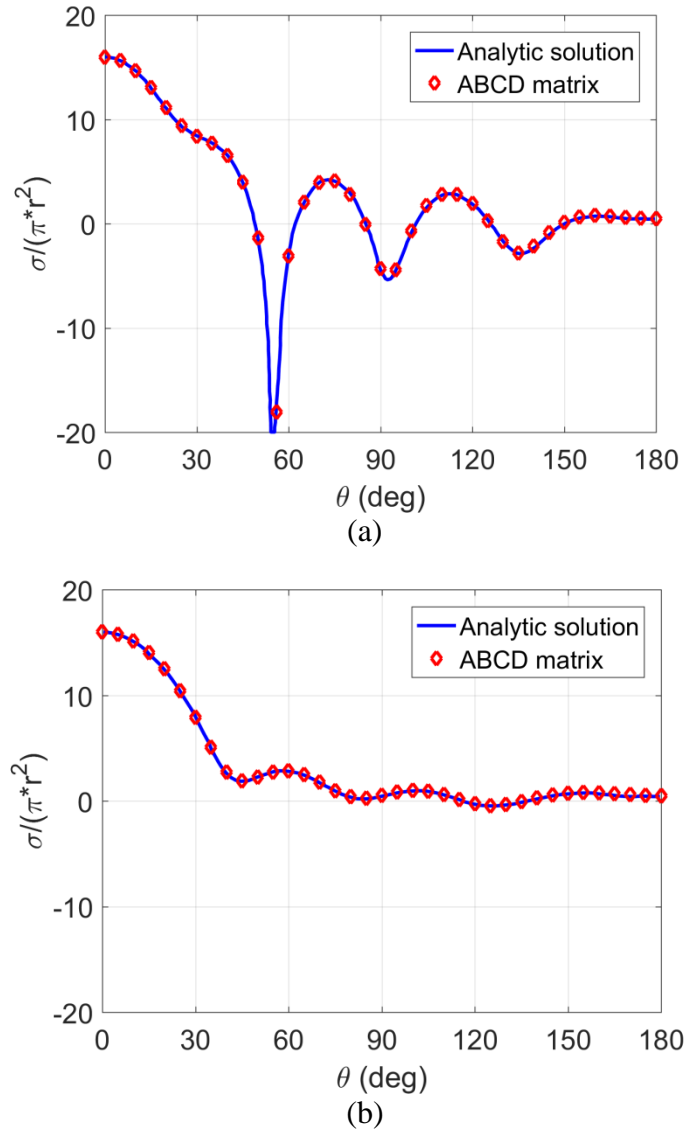


Fig. 3.14. Comparison of calculated bistatic scattering cross section of a sphere with opaque surface impedance boundary condition; (a) E-plane, (b) H-plane.

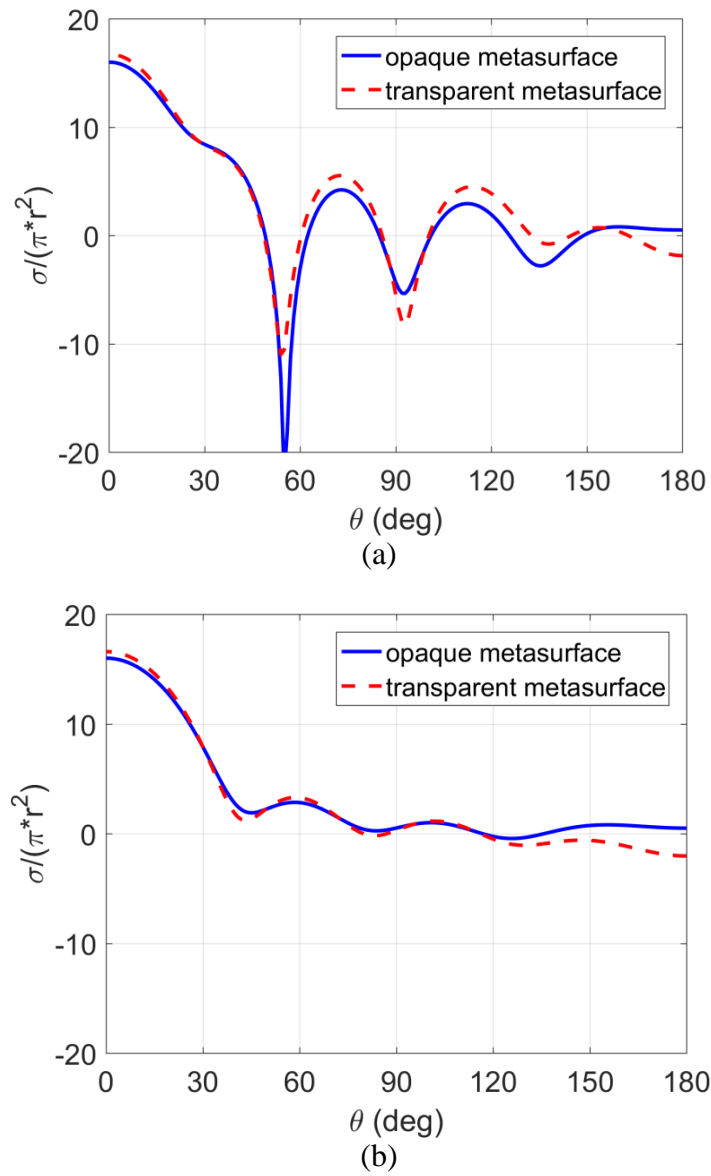


Fig. 3.15. Comparison of calculated bistatic scattering cross section of a sphere with opaque and transparent surface impedance boundary condition; (a) E-plane, (b) H-plane.

Modeling cascaded curved metasurfaces with non-homogeneous surface impedance

In the previous section we have described the method for analyzing curved metasurface structures for the cases when the value of metasurface sheet impedance do not spatially vary, (i.e. it is homogeneous). Such structures are suitable for building different devices, such as electromagnetic cloaks. However, for antenna applications, the designers would like to use metasurface sheets with spatially varying value of sheet impedance. Therefore, the proposed analysis method should be modified to include this possibility.

The importance of including spatially-varying curved metasurfaces into the analysis and design process is twofold. If the considered metasurfaces are used for manipulating the transmitted electromagnetic waves then in most of cases the value of sheet impedance is spatially varying. In other words, without this possibility it would be difficult to analyse such structures. The other reason is specific for canonical curved structures: the metasurface is usually placed on a part of the canonical surface only (e.g. on a part of a cylinder or a sphere). Such possibility is easily treated with the proposed approach (as will be explained in this chapter): at the part of a canonical surface without a metasurface layer the value of the surface sheet admittance is set to zero. Two examples of such structures are shown in Fig. 4.1. The considered dome antenna, used for correction of gain of the transmitting array can be placed concentrically around the array (i.e. the origin of the dome coordinate system is in the middle of the transmitting array), or the centre of dome antenna can be much below the centre of the transmitting array - in that case a low-profile dome antenna is obtained. Note that the correction of antenna gain can be significantly different: the metasurface dome can be used for example for flattening the gain of scanning beam (the “classical” dome design), or can be used to enhance the antenna gain.

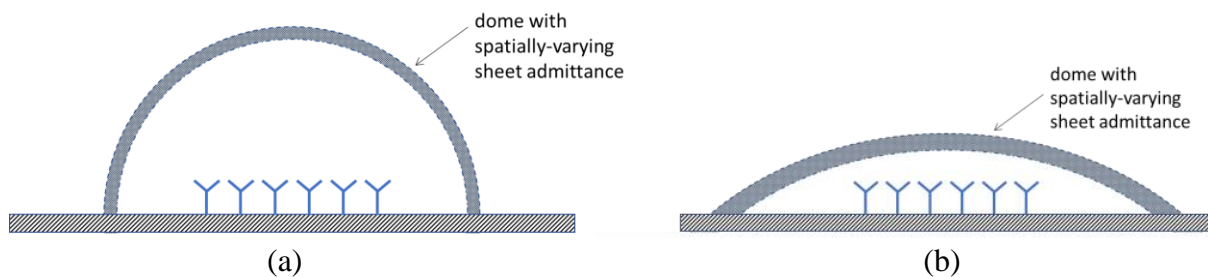


Fig. 4.1 Geometry of metasurface dome antenna; (a) concentric half-cylinder or half-sphere, (b) low-profile realization.

This section is organized as follows. First, we will consider one spatially-varying metasurface sheet in free-space and discuss four different analysis methods. Then we will generalize two methods to include multilayer dielectrics and metasurface sheets. Like in the previous section the analysis method will be given for circular-cylindrical structures, which can be easily modified for other types of geometries (spherical, BoR-type of structure, etc.)

4.1 Single-layer curved non-homogeneous metasurface sheet in free-space

The geometry of the problem is shown in Fig. 4.2. The considered metasurface is non-homogeneous in ϕ -direction and homogeneous in the axial direction (this assumption can be easily generalized in the same way the ϕ -directed non-homogeneity is analyzed). The metasurface is located in the free space and it is excited from the central axes, i.e. the excitation is a line source (the general excitation will be treated in the next section). Without losing the generality we assume that the excitation current is constant in axial direction, i.e. that the $k_z^{inc} = 0$. Therefore, the incident field is equal:

$$E_z^{inc}(\rho, \phi) = -\frac{k_0 \eta_0}{4} H_0^{(2)}(k_0 \rho) \cdot I_0 \quad (4.1.a)$$

$$H_\phi^{inc}(\rho, \phi) = -j \frac{k_0}{4} H_1^{(2)}(k_0 \rho) \cdot I_0. \quad (4.1.b)$$

Here I_0 is the amplitude of the line source. Under these assumptions we can write the field distribution in the inner and outer region:

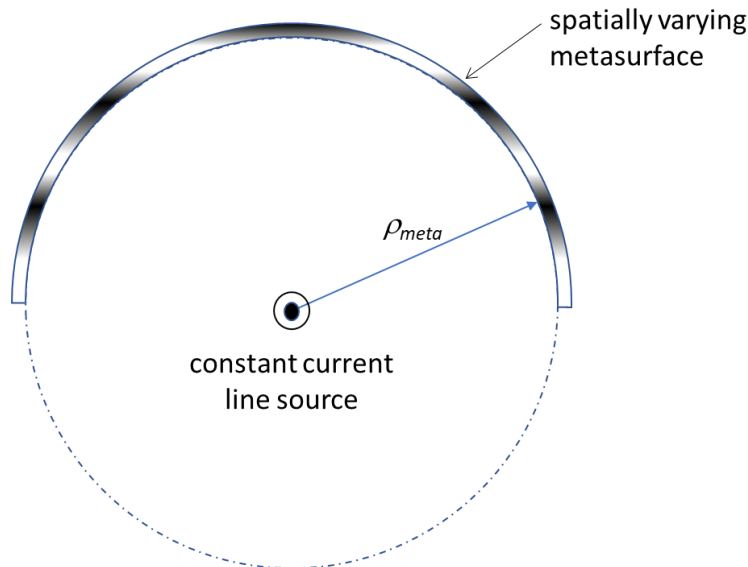


Fig. 4.2. Geometry of curved metasurface structure with spatially-varying value of surface sheet impedance.

(a) the inner region

$$E_z^{tot} = E_z^{inc} + E_z^{scat}$$

$$E_z^{tot}(\rho, \phi) = -\frac{k_0 \eta_0}{4} H_0^{(2)}(k_0 \rho) I_0 + \sum_{m=-\infty}^{\infty} a_m^{(1)} J_m(k_0 \rho) \quad (4.2.a)$$

$$H_\phi^{tot} = H_\phi^{inc} + H_\phi^{scat}$$

$$H_\phi^{tot}(\rho, \phi) = -\frac{jk_0}{4} H_1^{(2)}(k_0 \rho) I_0 + \left(\frac{-j}{\eta_0} \right) \sum_{m=-\infty}^{\infty} a_m^{(1)} J'_m(k_0 \rho) \quad (4.2.b)$$

(b) the outer region

$$E_z^{tot} = E_z^{inc} + E_z^{scat}$$

$$E_z^{tot}(\rho, \phi) = -\frac{k_0 \eta_0}{4} H_0^{(2)}(k_0 \rho) I_0 + \sum_{m=-\infty}^{\infty} a_m^{(2)} H_m^{(2)}(k_0 \rho) \quad (4.3.a)$$

$$H_\phi^{tot} = H_\phi^{inc} + H_\phi^{scat}$$

$$H_\phi^{tot}(\rho, \phi) = -\frac{jk_0}{4} H_1^{(2)}(k_0 \rho) I_0 + \left(\frac{-j}{\eta_0} \right) \sum_{m=-\infty}^{\infty} a_m^{(2)} H_0^{(2)'}(k_0 \rho) \quad (4.3.b)$$

Here $\alpha_m^{(1)}$ and $\alpha_m^{(2)}$ are the amplitudes of the spectral-domain scattered field components in the inner and outer region, respectively. Note that the H_z and E_ϕ components are equal to zero for the considered metasurface structure and line source excitation. The relation between the electric and magnetic field is derived from the following expressions (see eq. (3.3)):

$$H_\phi(\rho, \phi) = -\frac{j}{\eta_0 k_0} \frac{\partial}{\partial \rho} E_z(\rho, \phi) \quad (4.4)$$

Without losing generality we will assume that the considered metasurface has electric response only. The generalization to metasurfaces with magnetic response (loop or slotted metasurface elements) is straightforward. Under this assumption, the boundary condition needed to be satisfied is the following:

$$\hat{\rho} \times \mathbf{E}(\rho_{meta}, \phi) = \hat{\rho} \times \left[\bar{\bar{Z}}(\phi) \cdot (\hat{\rho} \times \Delta \mathbf{H}(\rho_{meta}, \phi)) \right] \quad (4.5)$$

Here we have assumed that the surface impedance is non-homogeneous in the ϕ -direction, i.e. $\bar{\bar{Z}}(\rho_{meta}, \phi, z) = \bar{\bar{Z}}(\phi)$. Therefore, we got the following system of equations to be solved (the indexes (1) and (2) denote the inner and outer region, respectively):

$$E_z^{scat,(1)}(\rho_{meta}, \phi) = E_z^{scat,(2)}(\rho_{meta}, \phi) \quad (4.6.a)$$

$$E_z^{inc}(\rho_{meta}, \phi) + E_z^{scat,(2)}(\rho_{meta}, \phi) = Z_{zz}(\phi) \left[H_z^{scat,(2)}(\rho_{meta}, \phi) - H_z^{scat,(1)}(\rho_{meta}, \phi) \right], \quad (4.6.b)$$

or in more details:

$$\frac{1}{2\pi} \sum_{m=-\infty}^{\infty} \alpha_m^{(1)} J_m(k_0 \rho_{meta}) e^{-jm\phi} = \frac{1}{2\pi} \sum_{m=-\infty}^{\infty} \alpha_m^{(2)} H_m^{(2)}(k_0 \rho_{meta}) e^{-jm\phi} \quad (4.7.a)$$

$$\begin{aligned} & -\frac{k_0 \eta_0}{4} H_0^{(2)}(k_0 \rho_{meta}) I_0 + \frac{1}{2\pi} \sum_{m=-\infty}^{\infty} \alpha_m^{(2)} H_m^{(2)}(k_0 \rho_{meta}) e^{-jm\phi} \\ & = Z_{zz}^{surf}(\phi) \left(\frac{-j}{\eta_0} \right) \left[\frac{1}{2\pi} \sum_{m=-\infty}^{\infty} \alpha_m^{(2)} H_m^{(2)'}(k_0 \rho_{meta}) e^{-jm\phi} - \frac{1}{2\pi} \sum_{m=-\infty}^{\infty} \alpha_m^{(1)} J_m'(k_0 \rho_{meta}) e^{-jm\phi} \right]. \end{aligned} \quad (4.7.b)$$

The first equation (boundary condition) can also be expressed in the spectral domain – the amplitude of each spectral component should be matched at the boundary:

$$\alpha_m^{(1)} J_m(k_0 \rho_{meta}) = \alpha_m^{(2)} H_m^{(2)}(k_0 \rho_{meta}) \quad (4.8)$$

The cylindrical metasurface can be placed only at the part of the cylindrical tube (the rest can be just air). Therefore, for that part of cylindrical tube we can impose the following boundary condition:

$$\hat{\rho} \times \Delta H(\rho_{meta}, \phi) = 0 \quad (4.9)$$

or

$$\frac{1}{2\pi} \sum_{m=-\infty}^{\infty} \alpha_m^{(2)} H_m^{(2)'}(k_0 \rho_{meta}) e^{-jm\phi} - \frac{1}{2\pi} \sum_{m=-\infty}^{\infty} \alpha_m^{(1)} J_m'(k_0 \rho_{meta}) e^{-jm\phi} = 0 \quad (4.10)$$

Both boundary conditions can be merged into one boundary condition by assuming that the surface sheet admittance is equal to zero at the part of the cylindrical tube without metasurface:

$$\hat{\rho} \times \left[\bar{\bar{Y}}(\phi) \cdot \mathbf{E}(\rho_{meta}, \phi) \right] = \hat{\rho} \times \left[\hat{\rho} \times \Delta \mathbf{H}(\rho_{meta}, \phi) \right] \quad (4.11)$$

This solution procedure can be rewritten using the Green's function approach that is suitable for multilayer structures containing cascaded metasurface sheets. The question is what type of Green's function has the unit (i.e. desired) value of the electric field and introduce the discontinuity in the magnetic field. The solution is that we need to use two separate Green's functions, one for the inner region, and another for the outer region. The inner/outer region should be bounded with the PEC-cylinder (PEC - perfect electric conductor) and the excitation will be the tangential magnetic current just above/below the PEC-cylinder

$$\mathbf{M}_{eq}(\phi) = -\hat{n} \times \mathbf{E}^{scat}(\rho_{meta}, \phi), \quad \hat{n} = \pm \hat{\rho} \quad (4.12)$$

Using notation $\alpha_m = \alpha_m^{(1)} J_m(k_0 \rho_{meta}) = \alpha_m^{(2)} H_m^{(2)}(k_0 \rho_{meta})$ we can express the z -component of the tangential E -field as:

$$E_z(\rho_{meta}, \phi) = \frac{1}{2\pi} \sum_{m=-\infty}^{\infty} \alpha_m e^{-jm\phi} \quad (4.13)$$

The solution procedure can be rewritten using the Green's functions as:

$$\begin{aligned} E_z(\rho_{meta}, \phi) &= \frac{1}{2\pi} \sum_{m=-\infty}^{\infty} \alpha_m e^{-jm\phi} \\ &= -\frac{1}{2\pi} \sum_{m=-\infty}^{\infty} \alpha_m \tilde{G}_{z\phi}^{EM,in}(m, \rho_{meta}^- | \rho_{meta}) e^{-jm\phi} = \frac{1}{2\pi} \sum_{m=-\infty}^{\infty} \alpha_m \tilde{G}_{z\phi}^{EM,out}(m, \rho_{meta}^+ | \rho_{meta}) e^{-jm\phi} \end{aligned} \quad (4.14.a)$$

$$\begin{aligned} Y_{zz}(\phi) \cdot \left[-\frac{k_0 \eta_0}{4} H_0^{(2)}(k_0 \rho_{meta}) I_0 + \frac{1}{2\pi} \sum_{m=-\infty}^{\infty} \alpha_m e^{-jm\phi} \right] \\ = \frac{1}{2\pi} \sum_{m=-\infty}^{\infty} \alpha_m \tilde{G}_{\phi\phi}^{HM,out}(m, \rho_{meta}^+ | \rho_{meta}) e^{-jm\phi} + \frac{1}{2\pi} \sum_{m=-\infty}^{\infty} \alpha_m \tilde{G}_{\phi\phi}^{HM,in}(m, \rho_{meta}^- | \rho_{meta}) e^{-jm\phi} \end{aligned} \quad (4.14.b)$$

Here ρ_{meta}^+ and ρ_{meta}^- denote the radial coordinate slightly larger and smaller than the metasurface radial coordinate, respectively. In general case the above equations can be written as:

$$\mathbf{E}(\rho_{meta}, \phi) = \hat{\phi} \frac{1}{2\pi} \sum_{m=-\infty}^{\infty} \alpha_m^\phi e^{-jm\phi} + \hat{z} \frac{1}{2\pi} \sum_{m=-\infty}^{\infty} \alpha_m^z e^{-jm\phi} \quad (4.15.a)$$

$$\begin{aligned} \bar{\bar{Y}}(\phi) \cdot \left[\mathbf{E}(\phi, \rho_{meta}) + \hat{\phi} \frac{1}{2\pi} \sum_{m=-\infty}^{\infty} \alpha_m^\phi e^{-jm\phi} + \hat{z} \frac{1}{2\pi} \sum_{m=-\infty}^{\infty} \alpha_m^z e^{-jm\phi} \right] \\ = \frac{1}{2\pi} \sum_{m=-\infty}^{\infty} \left[\tilde{\tilde{G}}^{HM,out}(m, \rho_{meta}^+ | \rho_{meta}) + \tilde{\tilde{G}}^{HM,in}(m, \rho_{meta}^- | \rho_{meta}) \right] \cdot \left[-\hat{z} \alpha_m^\phi + \hat{\phi} \alpha_m^z \right] e^{-jm\phi} \end{aligned} \quad (4.15.b)$$

Equation (4.14) is the basis for the first proposed analysis method. The unknowns in eq. (4.14) are the spectral-domain values α_m of the E -field at the metasurface. If we determine the limit in summation as M_{max} then we need to select $2 \cdot M_{max} + 1$ observation points to obtain a linear system of $2 \cdot M_{max} + 1$ equations with $2 \cdot M_{max} + 1$ unknowns. The minimum number for M_{max} is $\text{int}(k_0 \rho_{meta})$, more accurate results are obtained with $M_{max} = 2 \cdot \text{int}(k_0 \rho_{meta})$. Usually, one

observation point is located at each metasurface cell; however, if the selected M_{\max} is large, more than one observation point can be located at each metasurface cell. Therefore, the first proposed analysis method can be described with the following equation

$$\begin{aligned}
 Y_{zz}(\phi_n) \cdot & \left[-\frac{k_0 \eta_0}{4} H_0^{(2)}(k_0 \rho_{\text{meta}}) I_0 + \frac{1}{2\pi} \sum_{m=-M_{\max}}^{M_{\max}} \alpha_m e^{-jm\phi_n} \right] \\
 &= \frac{1}{2\pi} \sum_{m=-M_{\max}}^{M_{\max}} \alpha_m \tilde{G}_{\phi\phi}^{\text{HM,out}}(m, \rho_{\text{meta}}^+ | \rho_{\text{meta}}) e^{-jm\phi_n} + \frac{1}{2\pi} \sum_{m=-M_{\max}}^{M_{\max}} \alpha_m \tilde{G}_{\phi\phi}^{\text{HM,in}}(m, \rho_{\text{meta}}^- | \rho_{\text{meta}}) e^{-jm\phi_n}, \\
 n &= 1, \dots, 2 \cdot M_{\max} + 1.
 \end{aligned} \tag{4.16}$$

The boundary condition (4.11) can be fulfilled in the spectral domain as well. Using the convolution property of Fourier transformation, we obtain

$$\hat{\rho} \times \left[\tilde{\tilde{Y}} * (\tilde{\mathbf{E}}^{\text{scat}} + \tilde{\mathbf{E}}^{\text{inc}}) \right] = \hat{\rho} \times \left[\hat{n} \times \Delta \tilde{\mathbf{H}}^{\text{scat}} \right], \tag{4.17}$$

or

$$\begin{aligned}
 \frac{1}{2\pi} \sum_{m=-\infty}^{\infty} \tilde{Y}_{zz}(n-m) \cdot & \left[-\frac{\pi k_0 \eta_0}{2} H_0^{(2)}(k_0 \rho_{\text{meta}}) I_0 \delta_{0,m} + \alpha_m \right] \\
 &= \alpha_n \tilde{G}_{\phi\phi}^{\text{HM,out}}(n, \rho_{\text{meta}}^+ | \rho_{\text{meta}}) + \alpha_n \tilde{G}_{\phi\phi}^{\text{HM,in}}(n, \rho_{\text{meta}}^- | \rho_{\text{meta}}).
 \end{aligned} \tag{4.18}$$

Therefore, the second proposed analysis method is described with the following equation:

$$\begin{aligned}
 \frac{1}{2\pi} \sum_{m=-M_{\max}}^{M_{\max}} \tilde{Y}_{zz}(n-m) \cdot & \left[-\frac{\pi k_0 \eta_0}{2} H_0^{(2)}(k_0 \rho_{\text{meta}}) I_0 \delta_{0,m} + \alpha_m \right] \\
 &= \alpha_n \tilde{G}_{\phi\phi}^{\text{HM,out}}(n, \rho_{\text{meta}}^+ | \rho_{\text{meta}}) + \alpha_n \tilde{G}_{\phi\phi}^{\text{HM,in}}(n, \rho_{\text{meta}}^- | \rho_{\text{meta}}), \\
 n &= -M_{\max}, \dots, M_{\max}.
 \end{aligned} \tag{4.19}$$

Again, we have a linear system of $2 \cdot M_{\max} + 1$ equations with $2 \cdot M_{\max} + 1$ unknowns; the unknowns are again the spectral-domain values α_m of the E-field at the metasurface.

The proposed two analysis methods are not so practical if we want to generalize it for multilayer case with cascaded metasurfaces with both electric and magnetic responses due to large number of different geometries for which we need to determine the Green's functions (for magnetic response the inner/outer region should be bounded with the PMC-cylinder). Therefore, we would like to simplify the procedure (if possible).

Metasurfaces with electric response introduce the discontinuity in the tangential magnetic field, therefore it can be modeled with induced surface electric currents:

$$\mathbf{J}_{av} = \hat{n} \times (\mathbf{H}^+ - \mathbf{H}^-) = \hat{\rho} \times \Delta \mathbf{H}. \tag{4.20}$$

The boundary condition (4.11) now can be rewritten in the following way

$$\hat{\rho} \times \left[\bar{\bar{Y}}(\phi) \cdot \mathbf{E}(\rho_{meta}, \phi) \right] = \hat{\rho} \times [\mathbf{J}_{av}(\phi)], \quad (4.21)$$

or in more details

$$\hat{\rho} \times \left[\bar{\bar{Y}}(\phi) \cdot \left[\mathbf{E}^{inc}(\phi) + \frac{1}{2\pi} \sum_{m=-\infty}^{\infty} \bar{\bar{G}}^{EJ}(m, \rho_{meta} | \rho_{meta}) \cdot \tilde{\mathbf{J}}_{av}(m) e^{-jm\phi} \right] \right] = \hat{\rho} \times \left[\frac{1}{2\pi} \sum_{m=-\infty}^{\infty} \tilde{\mathbf{J}}_{av}(m) e^{-jm\phi} \right]. \quad (4.22)$$

Now the unknowns are the spectral-domain components of the averaged surface current. The used Green's function is "the normal one", i.e. the E-field due to electric current in considered multilayer structure without metasurface sheets (free space in this case). For the considered metasurface structure and line source excitation the upper equation can be written (the third proposed analysis method):

$$\begin{aligned} Y_{zz}(\phi_n) \cdot \left[-\frac{k_0 \eta_0}{4} H_0^{(2)}(k_0 \rho_{meta}) I_0 + \frac{1}{2\pi} \sum_{m=-M_{max}}^{M_{max}} \tilde{G}_{zz}^{EJ}(m, \rho_{meta} | \rho_{meta}) \cdot \tilde{J}_{z,av}(m) e^{-jm\phi_n} \right] \\ = \frac{1}{2\pi} \sum_{m=-M_{max}}^{M_{max}} \tilde{J}_{z,av}(m) e^{-jm\phi_n}, \\ n = 1, \dots, 2 \cdot M_{max} + 1. \end{aligned} \quad (4.23)$$

The boundary condition (4.20) can also be written in the spectral domain:

$$\hat{\rho} \times \left[\bar{\bar{Y}}(m) * \tilde{\mathbf{E}}(\rho_{meta}, m) \right] = \hat{\rho} \times [\tilde{\mathbf{J}}_{av}(m)], \quad (4.24)$$

or in more details

$$\hat{\rho} \times \left[\frac{1}{2\pi} \sum_{n=-\infty}^{\infty} \bar{\bar{Y}}(n-m) \cdot \left[\tilde{\mathbf{E}}^{inc}(m) + \bar{\bar{G}}^{EJ}(m, \rho_{meta} | \rho_{meta}) \cdot \tilde{\mathbf{J}}_{av}(m) \right] \right] = \hat{\rho} \times [\tilde{\mathbf{J}}_{av}(n)]. \quad (4.25)$$

For the considered metasurface structure and line source excitation, the upper equation can be written (the fourth proposed analysis method) as:

$$\begin{aligned} \frac{1}{2\pi} \sum_{m=-M_{max}}^{M_{max}} \tilde{Y}_{zz}(n-m) \cdot \left[-\frac{\pi k_0 \eta_0}{2} H_0^{(2)}(k_0 \rho_{meta}) I_0 \delta_{0,m} + \tilde{G}_{zz}^{EJ}(m, \rho_{meta} | \rho_{meta}) \cdot \tilde{J}_{z,av}(m) \right] \\ = \tilde{J}_{z,av}(n), \\ n = -M_{max}, \dots, M_{max}. \end{aligned} \quad (4.25)$$

Let us illustrate all four proposed methods on one example. Let us consider a single-layer cylindrical metasurface printed on a thin substrate ($\epsilon_r = 2.55$, $h = 0.13$ mm). The metasurface contains 24 inductive cells that are in practice realized using stripes or meander lines. The radius of the cylinder is 6 cm and the width of each cell is 7.854 mm, i.e. only half of the cylinder is covered with the metasurface structure. The variation of the surface sheet impedance and the practical realization is shown in Figure 4.3. The detailed description and measurement results will be given in the Section 6. Measured results.

The comparison of radiated field, calculated using different computational methods, is given in Fig. 4.4.a. The excitation was the omnidirectional line source (in practice, a monopole antenna was used as an excitation). All four methods give almost identical results that are not possible to distinguish. Therefore, we have shown only the comparison of the two methods in which the unknown is the surface sheet current in the spectral domain, and where the boundary conditions are tested in the spatial and spectral domains (named *combined-domain method* and *spectral-domain method*, respectively). As additional comparison the results calculated by CST Microwave Studio [37] and measured results are given in Fig. 4.4.b. Note that with the CST MS we have modeled the “real” structure from Fig. 4.3.b, i.e. with no simplification of metasurface structure using sheet impedance approach. The agreement of the two calculation methods with both CST calculations and measurements is very good.

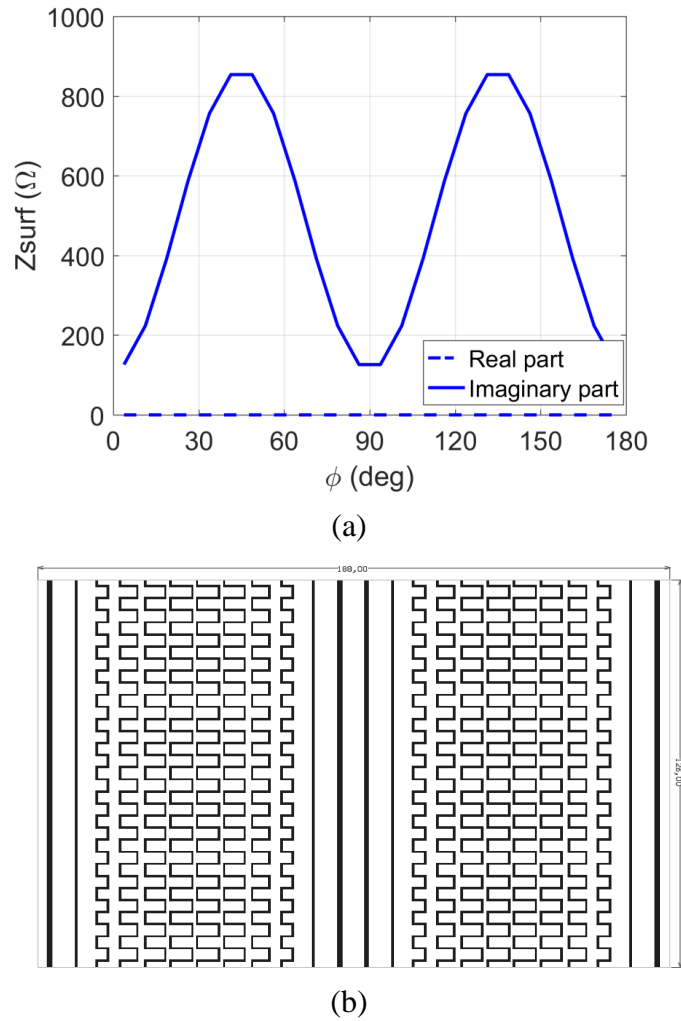


Fig. 4.3. Single-layer metasurface; (a) variation of the surface sheet impedance, (b) practical realization.

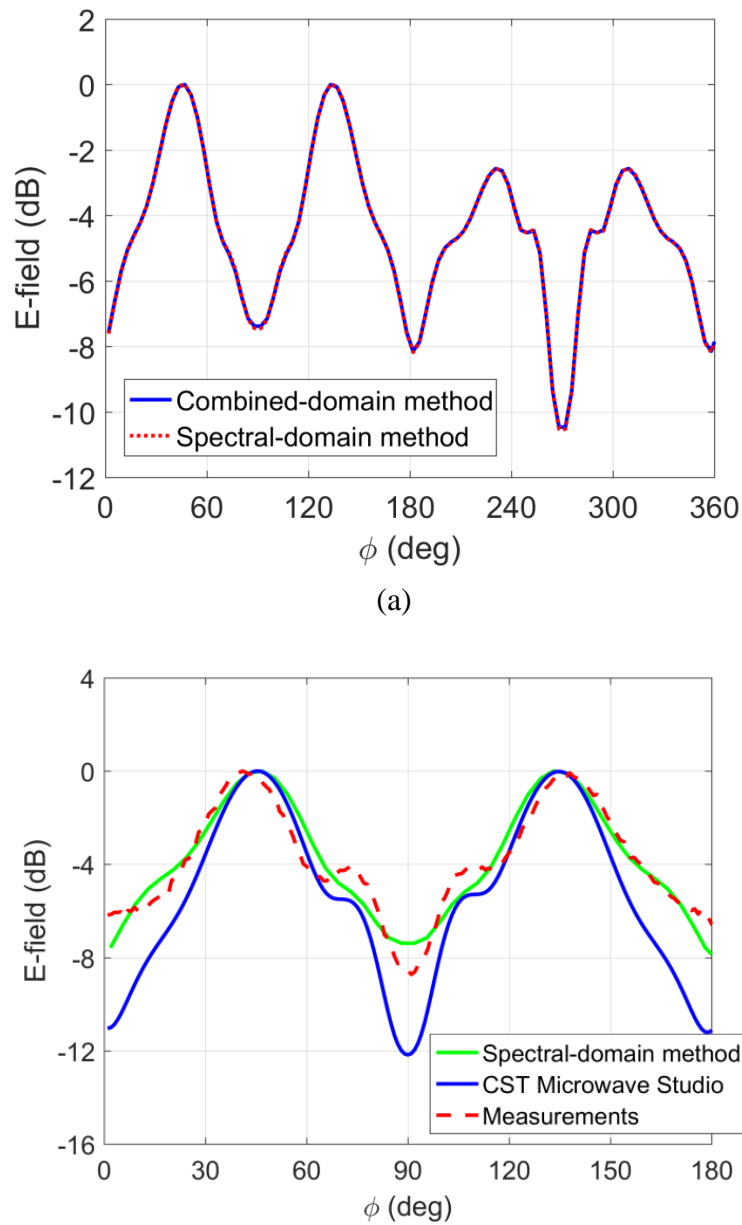


Fig. 4.4. (a) Comparison of the considered spectral domain methods in which the boundary conditions are tested in the spatial and spectral domains (named combined-domain method and spectral-domain method, respectively); (b) Comparison of the spectral-domain method (all four versions) and the calculated results obtained by CST Microwave Studio and measured results. In the last two cases the “real” structure shown in Fig. 4.3.b was modelled and measured.

4.2 Cascaded curved non-homogeneous metasurface sheets embedded into a multilayer structure

The single-layer formulation based on the surface current approach (i.e. the third and fourth analysis method presented in the previous section) is suitable for generalization to be able to analyze cascaded non-homogeneous metasurface structures. The approach based on the fulfilling the boundary conditions in the spatial domain, for the cascaded case is the following:

$$\begin{aligned} \hat{\rho} \times & \left[\bar{\bar{Y}}(\rho_{meta}^j, \phi_n) \cdot \left[\mathbf{E}^{inc}(\rho_{meta}^j, \phi_n) + \frac{1}{2\pi} \sum_{i=1}^{N_{layer}} \sum_{m=-M_{max}}^{M_{max}} \tilde{\tilde{G}}^{EJ}(m, \rho_{meta}^j | \rho_{meta}^i, i) \cdot \tilde{\mathbf{J}}_{av}^i(m) e^{-jm\phi_n} \right] \right] \\ & = \hat{\rho} \times \left[\frac{1}{2\pi} \sum_{m=-M_{max}}^{M_{max}} \tilde{\mathbf{J}}_{av}^j(m) e^{-jm\phi_n} \right] \quad n=1, \dots, 2 \cdot M_{max} + 1; \quad j=1, \dots, N_{layer} \end{aligned} \quad (4.26)$$

Here the superscript j in the quantities ρ_{meta}^j and $\tilde{\mathbf{J}}_{av}^j$ denotes the number of the cascaded metasurface layer (the total number of metasurface layers is N_{layer}). In the matrix form the equation (4.26) looks like (e.g. in total for three metasurface layers and for the case when the excitation and the surface currents are in the z-direction):

$$\begin{bmatrix} \begin{bmatrix} Z^{11} \\ Z^{21} \\ Z^{31} \end{bmatrix} & \begin{bmatrix} Z^{12} \\ Z^{22} \\ Z^{32} \end{bmatrix} & \begin{bmatrix} Z^{13} \\ Z^{23} \\ Z^{33} \end{bmatrix} \end{bmatrix} \cdot \begin{bmatrix} \begin{bmatrix} I^1 \\ I^2 \\ I^3 \end{bmatrix} \end{bmatrix} = \begin{bmatrix} \begin{bmatrix} V^1 \\ V^2 \\ V^3 \end{bmatrix} \end{bmatrix} \quad (4.27)$$

Again, the superscript denotes the metasurface layer where we test the boundary condition and where the surface current is located. The elements of the Z sub-matrices and of the excitation vector are equal:

$$Z_{n, m+M_{max}+1}^{ji} = \bar{\bar{Y}}_{zz}(\rho_{meta}^j, \phi_n) \cdot \left[\frac{1}{2\pi} \tilde{\tilde{G}}^{EJ}(m, \rho_{meta}^j | \rho_{meta}^i) e^{-jm\phi_n} \right] - \frac{1}{2\pi} \delta_{j,i} e^{-jm\phi_n} \quad (4.28.a)$$

$$V_n^j = Y_{zz}(\rho_{meta}^j, \phi_n) \cdot E_z^{inc}(\rho_{meta}^j, \phi_n) \quad (4.28.b)$$

The result is the spectral-domain amplitudes of the surface current: $I_m^i = \tilde{\mathbf{J}}_{z,av}^i(m)$.

The approach based on the fulfilling the boundary conditions in the spectral domain, for the cascaded case is the following:

$$\begin{aligned}
& \hat{\rho} \times \left[\frac{1}{2\pi} \sum_{m=-M_{\max}}^{M_{\max}} \tilde{\tilde{Y}}(\rho_{\text{meta}}^j, n-m) \cdot \left[\tilde{\mathbf{E}}^{\text{inc}}(\rho_{\text{meta}}^j, m) + \sum_{i=1}^{N_{\text{layer}}} \tilde{\tilde{G}}^{EJ}(m, \rho_{\text{meta}}^j | \rho_{\text{meta}}^i) \cdot \tilde{\mathbf{J}}_{\text{av}}^i(m) \right] \right] \\
& = \hat{\rho} \times \left[\tilde{\mathbf{J}}_{\text{av}}^j(n) \right], \\
& n = -M_{\max}, \dots, M_{\max}; \quad j = 1, \dots, N_{\text{layer}}.
\end{aligned} \tag{4.29}$$

The matrix form of the equation (4.29) is the following (e.g. for totally three metasurface layers and for the case when the excitation and the surface currents are in the z-direction):

$$\begin{bmatrix} \begin{bmatrix} Z^{11} \\ Z^{21} \\ Z^{31} \end{bmatrix} & \begin{bmatrix} Z^{12} \\ Z^{22} \\ Z^{32} \end{bmatrix} & \begin{bmatrix} Z^{13} \\ Z^{23} \\ Z^{33} \end{bmatrix} \end{bmatrix} \cdot \begin{bmatrix} \begin{bmatrix} I^1 \\ I^2 \\ I^3 \end{bmatrix} \end{bmatrix} = \begin{bmatrix} \begin{bmatrix} V^1 \\ V^2 \\ V^3 \end{bmatrix} \end{bmatrix} \tag{4.30}$$

The elements of the Z sub-matrices of and of the excitation vector are now:

$$Z_{n+M_{\max}+1, m+M_{\max}+1}^{ji} = \frac{1}{2\pi} \tilde{Y}_{zz}(\rho_{\text{meta}}^j, n-m) \cdot \tilde{\tilde{G}}^{EJ}(m, \rho_{\text{meta}}^j | \rho_{\text{meta}}^i) e^{-jm\phi_n} - \delta_{j,i} \tag{4.31.a}$$

$$V_n^j = -\frac{1}{2\pi} \sum_{m=-M_{\max}}^{M_{\max}} \tilde{\tilde{Y}}(\rho_{\text{meta}}^j, n-m) \cdot \tilde{\mathbf{E}}^{\text{inc}}(\rho_{\text{meta}}^j, m) \tag{4.32.b}$$

Like in the previous case the result is the spectral-domain amplitudes of the surface current: $I_m^i = \tilde{J}_{z, \text{av}}^i(m)$.

The excitation incident field can be determined using the equivalence principle. For example, if the source is located inside the metasurface structure (e.g. at the axis of the structure) then we can surround the source with an equivalent cylindrical surface with a radius smaller than the metasurface structure (see Fig. 4.5.). Then we can define the equivalent excitation currents at that surface using the fields radiated by the feed antenna into the free space (by this we do not take into account the coupling between the excitation antenna and the metasurface, but usually this coupling is small and thus it is not needed to be taken into account). Note that the arbitrary feed antenna for which we want to find the excitation incident field can be characterized either by measurements (often performed by the manufacturer) or by analysis using e.g. a general EM solver. Quite often we have only the E-field of the excitation field – in that case we need to use PEC equivalence principle. Therefore, for such a case the excitation incident field is equal:

$$\begin{aligned}
\tilde{\mathbf{M}}(\rho_{\text{eq}}^{\text{inc}}, m) &= \int_0^{2\pi} (-\hat{\rho} \times \mathbf{E}_{\text{free space}}^{\text{inc}}(\rho_{\text{eq}}^{\text{inc}}, \phi)) e^{jm\phi} d\phi, \\
\tilde{\mathbf{E}}^{\text{inc}}(\rho, m) &= \tilde{\tilde{G}}^{EM, \text{out}}(m, \rho | \rho_{\text{eq}}^{\text{inc}}) \cdot \tilde{\mathbf{M}}(\rho_{\text{eq}}^{\text{inc}}, m).
\end{aligned} \tag{4.33}$$

Here $\tilde{\tilde{G}}^{EM,out}$ is the Green's function of the considered metasurface structure with additional symmetrically located PEC cylinder of radius ρ_{eq}^{inc} .

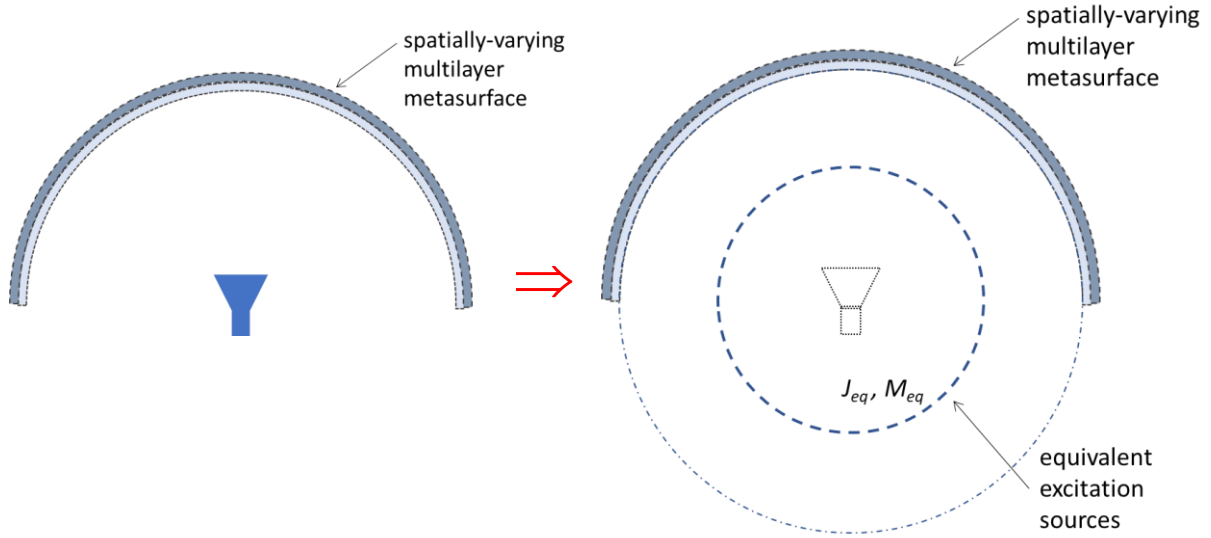


Fig. 4.5. Sketch of the excitation model based on the equivalence principle.

4.3 Comparison of two approaches of calculating metasurface sheet impedance

In this section we would like to compare two approaches to define sheet impedance of a metasurface, both of them related to the spectral domain. In the first approach, when the surface is homogenous (i.e. not spatially-varying) the surface impedance is defined via response to different impinging cylindrical waves. In other words, for each cylindrical harmonic of excitation we need to solve one-dimensional problem – variation of the EM field in the radial direction (both the ϕ and axial variations are defined with the source variation). In the second case, when considering the spatially-varying metasurface, we need to determine the variation of the sheet impedance with ϕ -coordinate. If we use the convolution approach the sheet impedance in the spectral domain is part of formulation, i.e. we need to perform the Fourier series of the sheet impedance in the spatial domain. Although both expressions are related with the spectral domain, they are fundamentally different. That can be seen in the example of longitudinal strips placed at the dielectric rod (the example described in Fig. 3.2).

We started the comparison with the response on impinging cylindrical waves (Figure 4.6.a; the way how it is calculated is explained in Chapter 3). The considered example is the same as the one described in Figures 3.2 – 3.4; the working frequency is 10 GHz. The spatial variation of the surface impedance (and therefore the value of the effective surface impedance) can be determined by transforming E - and H -field back to the spatial domain. In Figure 4.6.b. it can be seen that in the first case of longitudinal strips there is in principle no variation of surface impedance and its value is similar to the response to the zero-mode cylindrical harmonic ($Z_{zz}(m=0) = 83.76 \Omega$; also shown in the Figures 4.6.a and 4.6.b). However, if we calculate the spectral-domain surface impedance we will get only the strong zero-order mode since practically there is no ϕ -variation of the surface sheet impedance (Fig. 4.6.c). This shows the

difference between surface impedance in spectral domain and surface impedance calculated as a response to one spectral component of impinging field.

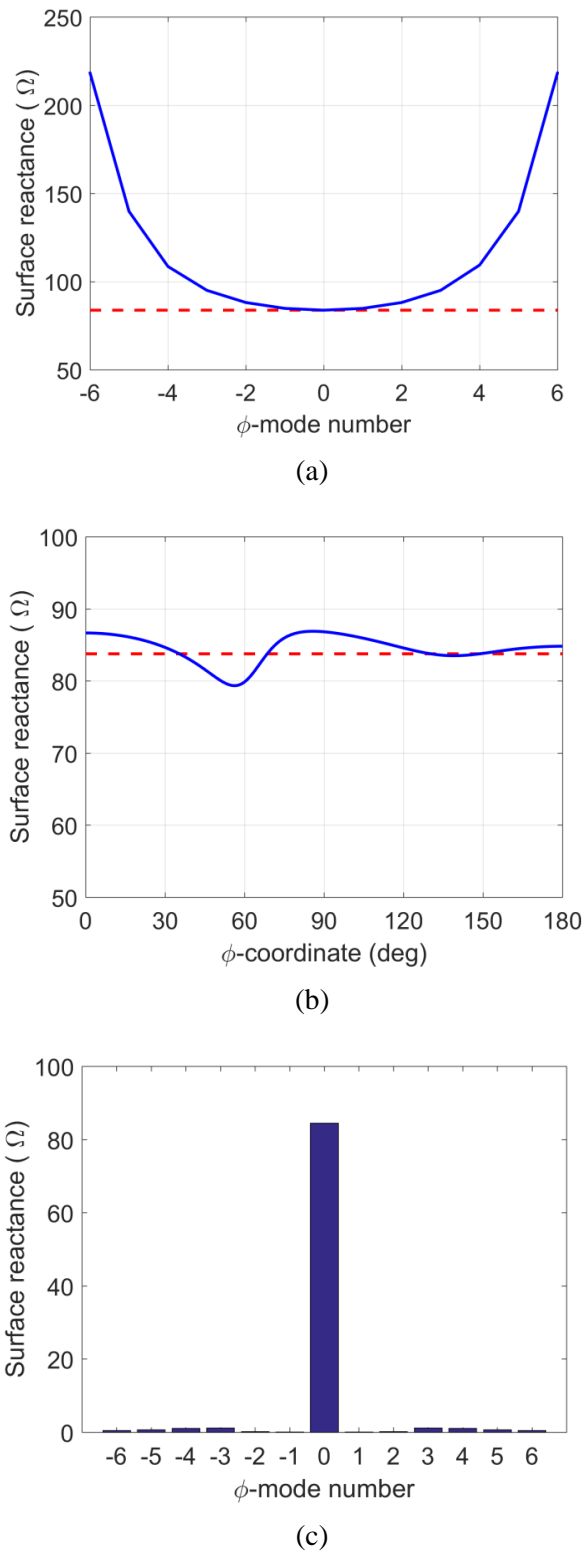


Fig. 4.5. Comparison of two approaches of calculating metasurface sheet impedance: (a) response to the different mode of impinging cylindrical wave; (b) spatial variation of metasurface sheet impedance; (c) Fourier transformation of spatial variation of metasurface sheet impedance (spectral-domain metasurface sheet impedance).

Analysis of Body-of-Revolution (BoR) metasurface structures

The rigorous numerical analysis of axially-symmetric metasurface components will be performed using the Electric Field Integral Equation (EFIE). Although this report will focus on axially-symmetric metasurface structures, presented formulation can be applied to other axially-symmetric geometries (e.g., cylindrical antennas and scatterers, metallic spheres, etc.). The axially-symmetric configurations are commonly referred to as Bodies of Revolution (BoR), i.e. these geometries are obtained by rotating generating curves about a single axis of symmetry, as illustrated in Fig. 5.1. The analysis and design of BoR structures is inspired by the work of Andreasen [38], Harrington and Mautz [39]-[41], Wu and Tsai [42], Wilton and Glisson [43]-[44], and Moreira [45].

5.1 Geometry of the BoR problem

The BoR surface is defined by its generating curve rotated about the BOR axis of symmetry, as shown in Fig. 5.1. We shall assume that the axis of symmetry coincides with the z -axis of the principal coordinate system. Also we shall define an orthogonal curvilinear coordinate system over the BoR surface. This coordinate system has the orthonormal base vectors \hat{t} , $\hat{\phi}$ and \hat{n} , where \hat{t} is the unit vector tangent to the surface and pointing along the generating curve, $\hat{\phi}$ is the unit vector tangent to the surface and pointing along the circumferential direction, and \hat{n} is the unit vector normal to the BoR surface, such that $\hat{n} = \hat{\phi} \times \hat{t}$ (see Fig. 5.1). Note that \hat{n} points outwards a closed BoR surface (i.e., towards the region where the excitation sources are located). The connection between these unit directions and the cylindrical coordinates of the principal coordinate is given with

$$\hat{t} = \sin u \hat{\rho} + \cos u \hat{z}, \quad (5.1)$$

$$\hat{n} = \hat{\phi} \times \hat{t} = \cos u \hat{\rho} - \sin u \hat{z}, \quad (5.2)$$

where u is the angle between \hat{t} and \hat{z} , as illustrated in Fig. 5.1.

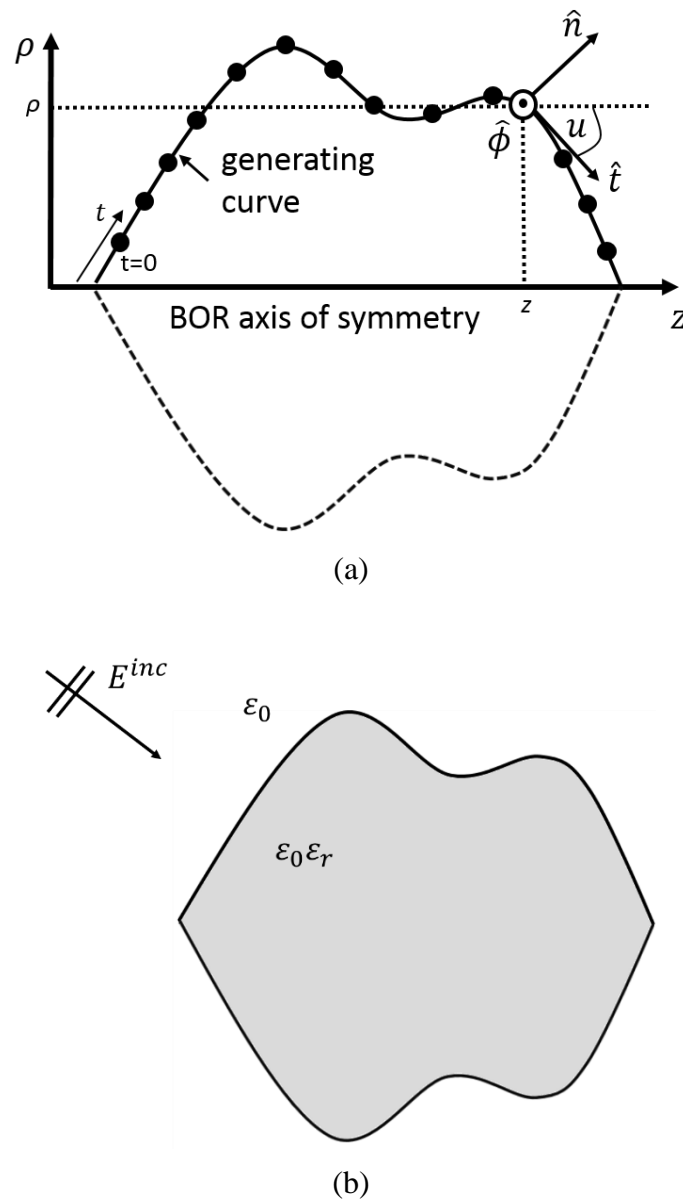


Fig. 5.1. The BoR geometry. (a) 2D view of generating curve with segmentation points; (b) scattering from a BoR dielectric body.

5.2 Formulation of the Electric Field Integral Equation

In order to find the appropriate numerical formulation let us first consider the basic BoR structure shown in Figure 5.1.b, i.e. the basic electromagnetic problem we would like to solve is to determine the scattered field from a rotationally symmetric dielectric body. We will assume a linear, homogeneous, and isotropic medium from which the dielectric body is realized. For this case the electromagnetic field at a given observation point outside a closed and finite region can be entirely determined by the prior knowledge of the electromagnetic behavior over the closed-region surface plus the radiation characteristics of any source located

outside the region (according to the Love's equivalence principle [35]). This is given by the Stratton-Chu formula [46], where the BoR surface defines the closed region. If we write this for the electric field we shall obtain the Electric Field Integral Equation (EFIE) which is given by:

(a) if the observation point \vec{r} is in the outside region:

$$\vec{E}^{total}(\vec{r}) = \vec{E}^{inc}(\vec{r}) - \frac{j}{4\pi\omega\epsilon_0} \oint_{S'} \{k_0^2 \vec{J}(\vec{r}') \Psi_0 - j\omega\epsilon \vec{M}(\vec{r}') \times \nabla' \Psi_0 - [\nabla' \vec{J}(\vec{r}')] \nabla' \Psi_0\} dS' \quad (5.3.a)$$

(b) if the observation point \vec{r} is in the inside region:

$$\vec{E}^{total}(\vec{r}) = \frac{j}{4\pi\omega\epsilon_0\epsilon_r} \oint_{S'} \{k_1^2 \vec{J}(\vec{r}') \Psi_1 - j\omega\epsilon_0\epsilon_r \vec{M}(\vec{r}') \times \nabla' \Psi_1 - [\nabla' \vec{J}(\vec{r}')] \nabla' \Psi_1\} dS'. \quad (5.3.b)$$

where S' represents the BoR closed surfaces, \vec{r} locates the observation point, \vec{r}' locates the source point over S' , and Ψ is the scalar Green's function:

$$\Psi_i = \frac{e^{-jk_i R}}{R}, \quad (5.3)$$

where $R = |\vec{r} - \vec{r}'|$ and $k_i = \frac{2\pi}{\lambda} = \omega\sqrt{\mu_0\epsilon_0\epsilon_{r,i}}$ with λ being the wavelength in the medium of interest. Here, the configurations to be analyzed are always surrounded by the homogeneous space described with relative permittivity $\epsilon_{r,i}$. Furthermore, in the equivalent problems, the equivalent electric and magnetic equivalent currents are defined using the values of the electromagnetic field at the boundary as

$$\hat{n} \times \vec{H}(\vec{r}') = \vec{J}(\vec{r}'), \quad (5.4)$$

$$\hat{n} \times \vec{E}(\vec{r}') = -\vec{M}(\vec{r}'), \quad (5.5)$$

respectively. Here \hat{n} is the unit surface normal at \vec{r}' pointing outwards. By using these equivalent currents the original electromagnetic problem is transferred into two equivalent problems, such that the electromagnetic field in the considered BoR region is identical to the one in the original problem. Therefore, in the case of basic two-region BoR problem (see Fig. 5.1.b) the EFIE results from the continuity of the tangential component of the E-field at the BoR boundary:

$$\begin{aligned}
\hat{n} \times \vec{E}^{inc}(\vec{r}) &= \frac{j}{4\pi\omega\epsilon_0} \hat{n} \times \oint_{S'} \{k_0^2 \vec{J}(\vec{r}') \Psi_0 - j\omega\epsilon_0 \vec{M}(\vec{r}') \times \nabla' \Psi_0 - [\nabla' \vec{J}(\vec{r}')] \nabla' \Psi_0\} dS' \\
&+ \frac{j}{4\pi\omega\epsilon_0\epsilon_r} \hat{n} \times \oint_{S'} \{k_1^2 \vec{J}(\vec{r}') \Psi_1 - j\omega\epsilon_0\epsilon_r \vec{M}(\vec{r}') \times \nabla' \Psi_1 - [\nabla' \vec{J}(\vec{r}')] \nabla' \Psi_1\} dS'.
\end{aligned} \tag{5.7}$$

Here Ψ_0 and Ψ_1 are the scalar Green's functions for homogeneous space with permittivity ϵ_0 and $\epsilon_0\epsilon_r$, respectively. Using the duality principle a similar equation can be derived for the magnetic field (MFIE):

$$\begin{aligned}
\hat{n} \times \vec{H}^{inc}(\vec{r}) &= \frac{j}{4\pi\omega\mu_0} \hat{n} \times \oint_{S'} \{k_0^2 \vec{M}(\vec{r}') \Psi_0 + j\omega\mu_0 \vec{J}(\vec{r}') \times \nabla' \Psi_0 - [\nabla' \vec{M}(\vec{r}')] \nabla' \Psi_0\} dS' \\
&+ \frac{j}{4\pi\omega\mu_0\mu_r} \hat{n} \times \oint_{S'} \{k_1^2 \vec{M}(\vec{r}') \Psi_1 + j\omega\mu_0\mu_r \vec{J}(\vec{r}') \times \nabla' \Psi_1 - [\nabla' \vec{M}(\vec{r}')] \nabla' \Psi_1\} dS'.
\end{aligned} \tag{5.8}$$

The unknown quantities in the eqs. (5.7) and (5.8) are the equivalent electric and magnetic currents $\vec{J}(\vec{r})$ and $\vec{M}(\vec{r})$ that can be determined using e.g. the moment method (MoM) technique. Since the MFIE can always be simply derived from EFIE using the duality principle, we will give in the rest of the section the expressions only for EFIE part of formulation.

The presence of a metasurface can be included by modifying the EFIE in the following way. Without losing the generality we assume that the metasurface is located in a homogeneous space. As explained in the Introduction we will focus our analysis to metasurfaces that have only an electric response, and they can be modelled with induced surface electric currents. The generalization to magnetic surface currents (loop or slotted metasurface elements) is straightforward.

The metasurface layer is modeled using a transparent surface impedance formulation (the geometry of the problem is shown in Fig. 5.1):

$$\hat{n} \times \vec{E}(\vec{r}) = \hat{n} \times [\bar{\bar{Z}}(\vec{r}) \cdot (\hat{n} \times (\vec{H}^+(\vec{r}) - \vec{H}^-(\vec{r})))] \tag{5.9}$$

Here, \vec{E} denotes the average electric field at the metasurface layer, \vec{H}^+ and \vec{H}^- are the average magnetic fields at the outer and inner metasurface boundaries, $\bar{\bar{Z}}$ is the surface impedance tensor, and \hat{n} is the outward pointing unit vector, normal to the metasurface layer. In the considered coordinate system, the surface impedance tensor can be expressed as

$$\bar{\bar{Z}}(\vec{r}) = \begin{bmatrix} Z_{tt}(\vec{r}) & Z_{t\phi}(\vec{r}) \\ Z_{\phi t}(\vec{r}) & Z_{\phi\phi}(\vec{r}) \end{bmatrix} \tag{5.10}$$

where the subscripts denote the corresponding components of the electric and magnetic field, respectively. $\bar{\bar{Z}}$ is not a constant tensor but rather depends on the spatial coordinate and on the properties of the impinging electromagnetic wave. For instance, in the planar case, it depends on the angle of incidence of the impinging electromagnetic wave.

The EFIE for a structure with a metasurface sheet in a homogeneous space is given by

$$\begin{aligned} \hat{n} \times \vec{E}^{inc}(\vec{r}) = \hat{n} \times \left(\bar{\bar{Z}}(\vec{r}) \cdot \vec{J}_{av}(\vec{r}) \right) + \frac{j}{4\pi\omega\epsilon_0} \hat{n} \\ \times \oint_{S'} \{ k_0^2 \vec{J}_{av}(\vec{r}') \Psi - j\omega\epsilon_0 \vec{M}_{av}(\vec{r}') \times \nabla' \Psi - [\nabla' \vec{J}_{av}(\vec{r}')] \nabla' \Psi \} dS'. \end{aligned} \quad (5.11)$$

Here the averaged electric and magnetic current densities take into account the discontinuity of the EM field due to presence of the transparent metasurface sheet:

$$\vec{J}_{av}(\vec{r}) = \hat{n} \times \left(\vec{H}^+(\vec{r}) - \vec{H}^-(\vec{r}) \right) \quad (5.12)$$

$$\vec{M}_{av}(\vec{r}) = -\hat{n} \times \left(\vec{E}^+(\vec{r}) - \vec{E}^-(\vec{r}) \right). \quad (5.13)$$

For the case of a metasurface electric response only the magnetic current is equal to zero, i.e. the tangential E-field is continuous at the metasurface ($\vec{M}_{av}(\vec{r}) \approx 0$). If the opaque metasurface sheet is present then the electric and magnetic current densities take into account the discontinuity of the EM field are equal:

$$\vec{J}_{av}(\vec{r}) = \hat{n} \times \vec{H}^+(\vec{r}) \quad (5.14)$$

$$\vec{M}_{av}(\vec{r}) = -\hat{n} \times \vec{E}^+(\vec{r}). \quad (5.15)$$

5.3 The Method of Moments (MoM)

In this section, the MoM technique is applied to the numerical solution of Eq. (5.7) or (5.10). The considered technique is basically based on transforming the integral equation into a system of linear algebraic equations.

First the unknown electric and magnetic currents $\vec{J}(\vec{r}')$ and $\vec{M}(\vec{r}')$ are represented by a finite summation of known basis functions $\vec{J}_j(\vec{r}')$ and $\vec{M}_j(\vec{r}')$, respectively:

$$\vec{J}(\vec{r}') = \sum_j^N \alpha_j \vec{J}_j(\vec{r}'), \quad \vec{M}(\vec{r}') = \sum_j^N \beta_j \vec{M}_j(\vec{r}'), \quad (5.16)$$

Here α_j and β_j are the unknown coefficients (complex amplitudes) that need to be determined. The substitution of Eq. (5.16) into Eq. (5.7) yields

$$\hat{n} \times \vec{E}^{inc}(\vec{r}) = \sum_j^N \alpha_j L^J(\vec{J}_j) + \sum_j^N \beta_j L^M(\vec{M}_j), \quad (5.17)$$

where

$$L^J(\vec{J}_j) = \frac{j}{4\pi\omega\epsilon_0} \hat{n} \times \int_{S'} \left\{ k_0^2 \vec{J}_j(\vec{r}') \Psi_0 + k_0^2 \vec{J}_j(\vec{r}') \Psi_1 - [\nabla' \vec{J}_j(\vec{r}')] \nabla' \Psi_0 - \frac{1}{\epsilon_1} [\nabla' \vec{J}_j(\vec{r}')] \nabla' \Psi_1 \right\} dS' \quad (5.18)$$

$$L^M(\vec{M}_j) = -\frac{1}{4\pi} \hat{n} \times \oint_{S'} \{ \vec{M}(\vec{r}') \times \nabla' \Psi_0 + \vec{M}(\vec{r}') \times \nabla' \Psi_1 \} dS' \quad (5.19)$$

To obtain the unknown coefficients α_j and β_j , the boundary condition (5.17) is enforced over S by means of weighting the equation with the test functions $\vec{W}_i(\vec{r})$:

$$\begin{aligned} \int_S \vec{W}_i(\vec{r}) \cdot [\hat{n} \times \vec{E}^{inc}(\vec{r})] dS \\ = \sum_j^N \alpha_j \int_S \vec{W}_i(\vec{r}) \cdot L^J(\vec{J}_j) dS + \sum_j^N \beta_j \int_S \vec{W}_i(\vec{r}) \cdot L^M(\vec{M}_j) dS. \end{aligned} \quad (5.20)$$

The MoM matrix equation is finally obtained

$$[V] = [Z][I], \quad (5.21)$$

where the i -th element of the column matrix $[V]$ is given by:

$$V_i = \int_S \vec{W}_i(\vec{r}) \cdot \vec{E}^{inc}(\vec{r}) dS \quad (5.22)$$

and the elements of the MoM matrix are given by

$$Z_{ij} = \int_S \vec{W}_i(\vec{r}) \cdot L^J(\vec{J}_j) dS \quad \text{or} \quad Z_{ij} = \int_S \vec{W}_i(\vec{r}) \cdot L^M(\vec{M}_j) dS. \quad (5.23)$$

The correct choice of the basis and weighting functions influences the convergence properties of the MoM. Here, the used basis and weighting functions are the local triangle and pulse functions. The \hat{t} -oriented electric currents are represented by triangle basis functions (by this the continuity of the current in \hat{t} -direction is ensured), while the $\hat{\phi}$ -directed electric currents are represented by pulse basis functions (the continuity the $\hat{\phi}$ -directed current is ensured by applying the Fourier series in the $\hat{\phi}$ -direction, see below). For example, the electric current can be represented as (see Figure 5.2.):

$$\vec{J}_j(\vec{r}') = \sum_{n=-\infty}^{\infty} \left\{ \sum_{j=1}^{N_T} \alpha_{nj}^T \frac{T_j(t')}{\rho'} e^{jn\phi'} \hat{t}' + \sum_{j=1}^{N_P} \alpha_{nj}^P \frac{P_j(t')}{\rho_j} e^{jn\phi'} \hat{\phi}' \right\}, \quad (5.24)$$

where \hat{t}' and $\hat{\phi}'$ are the unit vectors at the source point \vec{r}' over the surface S' , $T_j(t')$ and $P_j(t')$ are the triangle and pulse basis functions, respectively, N_T and N_P are the total number of triangle and pulse basis functions, respectively, and α_{nj}^T and β_{nj}^P are the unknown complex coefficients associated with $T_j(t')$ and $P_j(t')$, respectively.

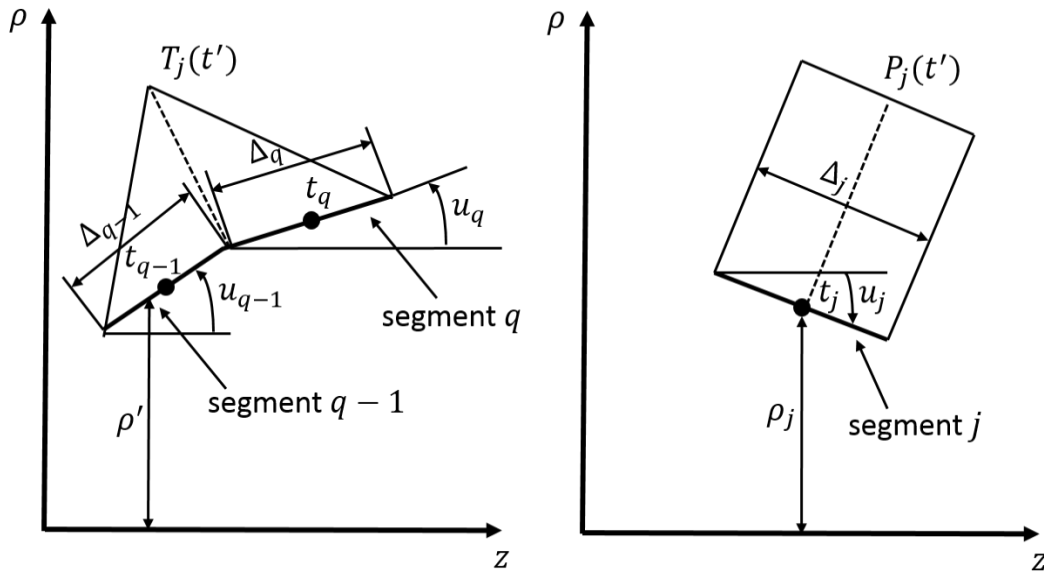


Fig. 5.2. Triangle and pulse basis functions

Triangle basis function $T_j(t')$ is defined over two consecutive source segments. For each $T_j(t')$ the subscript $q - 1$ is used to identify the associated source segment where $T_j(t')$ has a positive first derivative, while the subscript q identifies the remaining source segment where

the derivative is negative. In Eq. (5.24), the division of $T_j(t')$ by ρ' avoids numerical problems whenever ρ' is close to zero. The pulse function $P_j(t')$ is defined over a single source segment, which is simply represented by the subscript j . In Eq. (5.24), the division of $P_j(t')$ by ρ_j is used to maintain the same unit for both \hat{t} - and $\hat{\phi}$ -current representations (no numerical singularity is introduced by this division since ρ_j will never be zero). By applying the Fourier series in Eq. (5.24), a sinusoidal behavior is chosen for the azimuthal variation on both current elements $T_j(t')$ and $P_j(t')$, where n is an integer number.

From numerical point of view it is convenient to introduce a parameter τ , defined in the interval $[-1,1]$, used to express the source coordinates t' , ρ' and z' :

$$t' = t_l + \tau \frac{\Delta_l}{2} \quad (5.25)$$

$$\rho' = \rho_l + \tau \frac{\Delta_l}{2} \sin u_l \quad (5.26)$$

$$z' = z_l + \tau \frac{\Delta_l}{2} \cos u_l. \quad (5.27)$$

The triangular basis functions and their derivatives are expressed as:

$$T_j(t') = \begin{cases} \frac{1+\tau}{2} & t' \in \text{segment } q-1 \\ \frac{1-\tau}{2} & t' \in \text{segment } q \end{cases} \quad (5.28.a)$$

$$T_j'(t') = \begin{cases} \frac{1}{\Delta_{q-1}} & t' \in \text{segment } q-1 \\ -\frac{1}{\Delta_q} & t' \in \text{segment } q \end{cases} \quad (5.28.b)$$

where Δ_q is the length of the source segment q . Furthermore, the pulse basis function is simply given by $P_j(t') = 1$.

When selecting the test functions $\vec{W}_i(\vec{r})$ Galerkin's approach is employed. In our case:

$$\vec{W}_i(\vec{r}) = \sum_{m=-\infty}^{\infty} \left[\frac{T_i(t)}{\rho} \hat{t} + \frac{P_i(t)}{\rho_i} \hat{\phi} \right] e^{-jm\phi}. \quad (5.29)$$

As two different basis functions $[T_j(t')$ and $P_j(t')]$ and two different weighting functions $[T_i(t)$ and $P_i(t)]$ are used, and we are testing the continuity of tangential components of both the electric and magnetic field, the matrix equation of Eq. (5.21) is written as

$$\begin{bmatrix} V^{T,E} \\ V^{P,E} \\ V^{T,H} \\ V^{T,H} \end{bmatrix} = \begin{bmatrix} Z^{EE,TT} & Z^{EE,TP} & Z^{EH,TT} & Z^{EH,TP} \\ Z^{EE,PT} & Z^{EE,PP} & Z^{EH,PT} & Z^{EH,PP} \\ Z^{HE,TT} & Z^{HE,TP} & Z^{HH,TT} & Z^{HH,TP} \\ Z^{HE,PT} & Z^{HE,PP} & Z^{HH,PT} & Z^{HH,PP} \end{bmatrix} \begin{bmatrix} \alpha^T \\ \alpha^P \\ \beta^T \\ \beta^P \end{bmatrix}, \quad (5.30)$$

where from Eqs. (5.22) and (5.29), the elements of the sub-matrices V^T and V^P are given by (e.g. for the electric field):

$$V_i^{T,E} = \int_S \frac{T_i(t)}{\rho} e^{-jm\phi} \hat{t} \cdot \vec{E}^{inc}(\vec{r}) dS, \quad i = 1, \dots, N_T, \quad (5.31)$$

$$V_i^{P,E} = \int_S \frac{P_i(t)}{\rho_i} e^{-jm\phi} \hat{\phi} \cdot \vec{E}^{inc}(\vec{r}) dS, \quad i = 1, \dots, N_P, \quad (5.32)$$

and the elements of submatrices of matrix Z (e.g. submatrices related to the E-field: $Z^{TT,EE}, Z^{TP,EE}, Z^{PT,EE}, Z^{PP,EE}$) are given by:

$$\begin{aligned} Z_{ij}^{TT,EE} = \frac{j\eta}{4\pi k} \int_S \int_{S'} \left\{ k^2 \frac{T_i(t)}{\rho} \frac{T_j(t')}{\rho'} e^{j(n\phi' - m\phi)} \hat{t} \cdot \hat{t}' - \nabla \left[\frac{T_i(t)}{\rho} e^{-jm\phi} \hat{t} \right] \right. \\ \left. \times \nabla' \cdot \left[\frac{T_j(t')}{\rho'} e^{jn\phi'} \hat{t}' \right] \right\} \Psi dS dS' \end{aligned} \quad (5.33)$$

$$\begin{aligned} Z_{ij}^{TP,EE} = \frac{j\eta}{4\pi k} \int_S \int_{S'} \left\{ k^2 \frac{T_i(t)}{\rho} \frac{P_j(t')}{\rho_j} e^{j(n\phi' - m\phi)} \hat{t} \cdot \hat{\phi}' - \nabla \left[\frac{T_i(t)}{\rho} e^{-jm\phi} \hat{t} \right] \right. \\ \left. \times \nabla' \cdot \left[\frac{P_j(t')}{\rho_j} e^{jn\phi'} \hat{\phi}' \right] \right\} \Psi dS dS' \end{aligned} \quad (5.34)$$

$$\begin{aligned} Z_{ij}^{PT,EE} = \frac{j\eta}{4\pi k} \int_S \int_{S'} \left\{ k^2 \frac{P_i(t)}{\rho_i} \frac{T_j(t')}{\rho'} e^{j(n\phi' - m\phi)} \hat{\phi} \cdot \hat{t}' - \nabla \left[\frac{P_i(t)}{\rho_i} e^{-jm\phi} \hat{\phi} \right] \right. \\ \left. \times \nabla' \cdot \left[\frac{T_j(t')}{\rho'} e^{jn\phi'} \hat{t}' \right] \right\} \Psi dS dS', \end{aligned} \quad (5.35)$$

$$\begin{aligned} Z_{ij}^{PP,EE} = \frac{j\eta}{4\pi k} \int_S \int_{S'} \left\{ k^2 \frac{P_i(t)}{\rho_i} \frac{P_j(t')}{\rho_j} e^{j(n\phi' - m\phi)} \hat{\phi} \cdot \hat{\phi}' - \nabla \left[\frac{P_i(t)}{\rho_i} e^{-jm\phi} \hat{\phi} \right] \right. \\ \left. \times \nabla' \cdot \left[\frac{P_j(t')}{\rho_j} e^{jn\phi'} \hat{\phi}' \right] \right\} \Psi dS dS'. \end{aligned} \quad (5.36)$$

The evaluation of the surface integrals (5.33) – (5.36) is accomplished using the following change of coordinates and the vector calculus:

$$dS = \rho \, dt \, d\phi \quad (5.37)$$

$$\hat{t} \cdot \hat{t}' = \sin u \sin u' \cos(\phi - \phi') + \cos u \cos u', \quad (5.38)$$

$$\hat{t} \cdot \phi' = \sin u \sin(\phi - \phi'), \quad (5.39)$$

$$\hat{\phi} \cdot \hat{t}' = -\sin u' \sin(\phi - \phi'), \quad (5.40)$$

$$\hat{\phi} \cdot \hat{\phi}' = \cos(\phi - \phi'), \quad (5.41)$$

$$\nabla \cdot \vec{F} = \frac{1}{\rho} \frac{\partial}{\partial t} (\rho F_t) + \frac{1}{\rho} \frac{\partial}{\partial \phi} (F_\phi), \quad (5.42)$$

$$R = \left[(\rho - \rho')^2 + (z - z')^2 + 4\rho\rho' \sin^2 \left(\frac{\phi - \phi'}{2} \right) \right]^{\frac{1}{2}}, \quad (5.43)$$

$$\frac{1}{R} \frac{d\Psi}{dR} = -\frac{(1 + jkR)}{R^3} e^{-jkR} \quad (5.44)$$

Equations (5.33) – (5.36), as well as other elements of the MoM matrix (Eq. (5.30)), can be rewritten as

$$Z_{ij}^{TT,EE} = j\eta \int_t \int_{t'} \left\{ k^2 T_i(t) T_j(t') [\sin u \sin u' G_1(t, t') + \cos u \cos u' G_3(t, t')] - T'_i(t) T'_j(t') G_3(t, t') \right\} dt' dt, \quad (5.45)$$

$$Z_{ij}^{TP,EE} = \eta \int_t \int_{t'} \frac{P_j(t')}{\rho_j} [k^2 T_i(t) \rho' \sin u G_2(t, t') + m T'_i(t) G_3(t, t')] dt' dt, \quad (5.46)$$

$$Z_{ij}^{TT,EH} = j \int_t \int_{t'} \left\{ k T_i(t) T_j(t') [\rho' \sin u \cos u' - \rho \cos u \sin u' + (z - z') \sin u \sin u'] G_5(t, t') \right\} dt' dt, \quad (5.47)$$

$$Z_{ij}^{TP,EH} = - \int_t \int_{t'} \left\{ k T_i(t) \frac{P_j(t')}{\rho_j} [\rho' \cos u G_6(t, t') - \rho \cos u G_4(t, t') + (z - z') \sin u G_4(t, t')] \right\} \rho' dt' dt, \quad (5.48)$$

$$Z_{ij}^{PT,EE} = -\eta \int_t \int_{t'} \frac{P_i(t)}{\rho_i} [k^2 T_j(t') \rho \sin u' G_2(t, t') + m T_j'(t') G_3(t, t')] dt' dt, \quad (5.49)$$

$$Z_{ij}^{PP,EE} = j\eta \int_t \int_{t'} \frac{P_i(t)}{\rho_i} \frac{P_j(t')}{\rho_j} [k^2 \rho \rho' \sin u' G_1(t, t') - m^2 G_3(t, t')] dt' dt, \quad (5.50)$$

$$Z_{ij}^{PT,EH} = - \int_t \int_{t'} \left\{ k \frac{P_i(t)}{\rho_i} T_j(t') [\rho \cos u' G_6(t, t') - \rho' \cos u' G_4(t, t') - (z - z') \sin u' G_4(t, t')] \right\} \rho dt' dt, \quad (5.51)$$

$$Z_{ij}^{PP,EH} = j \int_t \int_{t'} k \frac{P_i(t)}{\rho_i} \frac{P_j(t')}{\rho_j} (z - z') G_5(t, t') \rho \rho' dt' dt, \quad (5.52)$$

where the integrals with respect to the ϕ are given by

$$G_1(t, t') = \frac{1}{2} \int_0^{2\pi} \cos \phi e^{-jm\phi} \frac{e^{-jk_0 R}}{k_0 R} d\phi = \int_0^\pi \cos \phi \cos m\phi \frac{e^{-jk_0 R}}{k_0 R} d\phi, \quad (5.53)$$

$$G_2(t, t') = \frac{j}{2} \int_0^{2\pi} \sin \phi e^{-jm\phi} \frac{e^{-jk_0 R}}{k_0 R} d\phi = \int_0^\pi \sin \phi \sin m\phi \frac{e^{-jk_0 R}}{k_0 R} d\phi, \quad (5.54)$$

$$G_3(t, t') = \frac{1}{2} \int_0^{2\pi} e^{-jm\phi} \frac{e^{-jk_0 R}}{k_0 R} d\phi = \int_0^\pi \cos m\phi \frac{e^{-jk_0 R}}{k_0 R} d\phi. \quad (5.55)$$

$$\begin{aligned} G_4(t, t') &= \frac{1}{2} \int_0^{2\pi} \cos \phi e^{-jm\phi} \frac{1}{R} \frac{d}{dR} \left(\frac{e^{-jk_0 R}}{k_0 R} \right) d\phi \\ &= \int_0^\pi \cos \phi \cos m\phi \frac{1}{R} \frac{d}{dR} \left(\frac{e^{-jk_0 R}}{k_0 R} \right) d\phi, \end{aligned} \quad (5.56)$$

$$\begin{aligned}
G_5(t, t') &= \frac{j}{2} \int_0^{2\pi} \sin \phi e^{-jm\phi} \frac{1}{R} \frac{d}{dR} \left(\frac{e^{-jk_0 R}}{k_0 R} \right) d\phi \\
&= \int_0^{\pi} \sin \phi \sin m\phi \frac{1}{R} \frac{d}{dR} \left(\frac{e^{-jk_0 R}}{k_0 R} \right) d\phi,
\end{aligned} \tag{5.57}$$

$$\begin{aligned}
G_6(t, t') &= \frac{1}{2} \int_0^{2\pi} e^{-jm\phi} \frac{1}{R} \frac{d}{dR} \left(\frac{e^{-jk_0 R}}{k_0 R} \right) d\phi \\
&= \int_0^{\pi} \cos m\phi \frac{1}{R} \frac{d}{dR} \left(\frac{e^{-jk_0 R}}{k_0 R} \right) d\phi.
\end{aligned} \tag{5.58}$$

The other elements of the MoM matrix can be easily found by using the duality principle.

As it is already mentioned, the metasurface layers are implemented into the BoR code through the sheet impedance approach, i.e. by considering the EFIE for a structure with metasurface sheets. If we assume that the considered metasurface sheets have electric response only, i.e. if we assume that the tangential E-field is continuous at the metasurface, then the boundary condition that we will solve using the EFIE-MoM approach is

$$\hat{n} \times \vec{E}^{inc}(\vec{r}) + \hat{n} \times \vec{E}^{scat}(\vec{r}) = \hat{n} \times \left(\vec{\bar{Z}}(\vec{r}) \cdot \vec{J}_{av}(\vec{r}) \right), \tag{5.59}$$

where \vec{E}^{scat} represents the scattered E-field from the metasurface sheet. The modified EFIE for a structure with a metasurface sheet in a homogeneous space is given by

$$\begin{aligned}
\hat{n} \times \vec{E}^{inc}(\vec{r}) &= \hat{n} \times \left(\vec{\bar{Z}}(\vec{r}) \cdot \vec{J}_{av}(\vec{r}) \right) \\
&+ \frac{j}{4\pi\omega\epsilon_0} \times \oint_{S'} \{ k_0^2 \vec{J}_{av}(\vec{r}') \Psi - [\nabla' \cdot \vec{J}_{av}(\vec{r}')] \nabla' \Psi \} dS'.
\end{aligned} \tag{5.60}$$

Comparing to “classical” implementation of the MoM the presence of the metasurface sheets results in new type of terms:

$$\int_S \vec{W}_i(\vec{r}) \cdot \vec{\bar{Z}}(\vec{r}) \cdot \vec{J}_j(\vec{r}) dS \tag{5.61}$$

The value of these integrals is different from zero only in the case when the basis and test functions are in the same direction (\hat{t} - or $\hat{\phi}$ -directed) and when they share at least part of domain where they are defined. For example, in the case of $\hat{\phi}$ -directed basis and test functions, the result is different from zero only in the case when the basis and test function are coincident. The value of additional integral term is equal:

$$\int_S Z_{\phi\phi} \left(\frac{P_i(t)}{\rho_i} \right)^2 \rho d\rho d\phi = \int_0^{2\pi} \int_{-1}^1 Z_{\phi\phi} \left(\frac{\Delta_i}{2\rho_i^2} \right) \left(\rho_i + \tau \frac{\Delta_i}{2} \sin u_i \right) d\tau d\phi = 2\pi Z_{\phi\phi} \Delta_i / \rho_i$$

(5.62)

In the case of \hat{t} -directed basis and test functions, they can only be partly coincident (on one segment), or they can be fully coincident (on both segments). In the second case, the additional integral term is equal:

$$\begin{aligned} & \int_S Z_{tt} \left(\frac{T_i(t)}{\rho} \right)^2 \rho \, d\rho d\phi \\ &= \int_0^{2\pi} \int_{-1}^1 Z_{tt} \frac{(1+\tau)^2}{\rho_i + \tau \frac{\Delta_i}{2} \sin u_i} \left(\frac{\Delta_i}{2} \right) d\tau d\phi + \int_0^{2\pi} \int_{-1}^1 Z_{tt} \frac{(1-\tau)^2}{\rho_i + \tau \frac{\Delta_i}{2} \sin u_i} \left(\frac{\Delta_i}{2} \right) d\tau d\phi \end{aligned} \quad (5.63)$$

These two integrals can be analytically calculated using the following formulas:

$$X = ax + b \quad (5.64)$$

$$\int \frac{dx}{X} = \frac{1}{a} \ln X \quad (5.65)$$

$$\int \frac{xdx}{X} = \frac{x}{a} - \frac{b}{a^2} \ln X \quad (5.66)$$

$$\int \frac{x^2 dx}{X} = \frac{1}{a^3} \left(\frac{1}{2} X^2 - 2bX + b^2 \ln X \right). \quad (5.67)$$

5.4 Numerical algorithm for calculating Green's functions of 2D multiregion structures

In this section we will describe an algorithm for calculating Green's functions of 2D multiregion structures. The algorithm represents modification of previously developed numerical algorithm for calculating the Green's function of 1D multilayer structures of planar, circular-cylindrical and spherical type (named the G1DMULT algorithm). Here one-dimensional (1D) structures denote structures that are homogeneous in two dimensions and they vary in one dimension only. Similarly, two-dimensional (2D) structures denote structures that are homogeneous in one dimensions and they vary in two dimensions (we are in particular interested in BoR type of 2D structures).

In order to understand the newly developed algorithm, first we will describe the previously developed G1DMULT algorithm (see Fig.5.3). The algorithm starts with a 3D problem including some excitation currents (e.g. a chosen current distribution on a microstrip patch

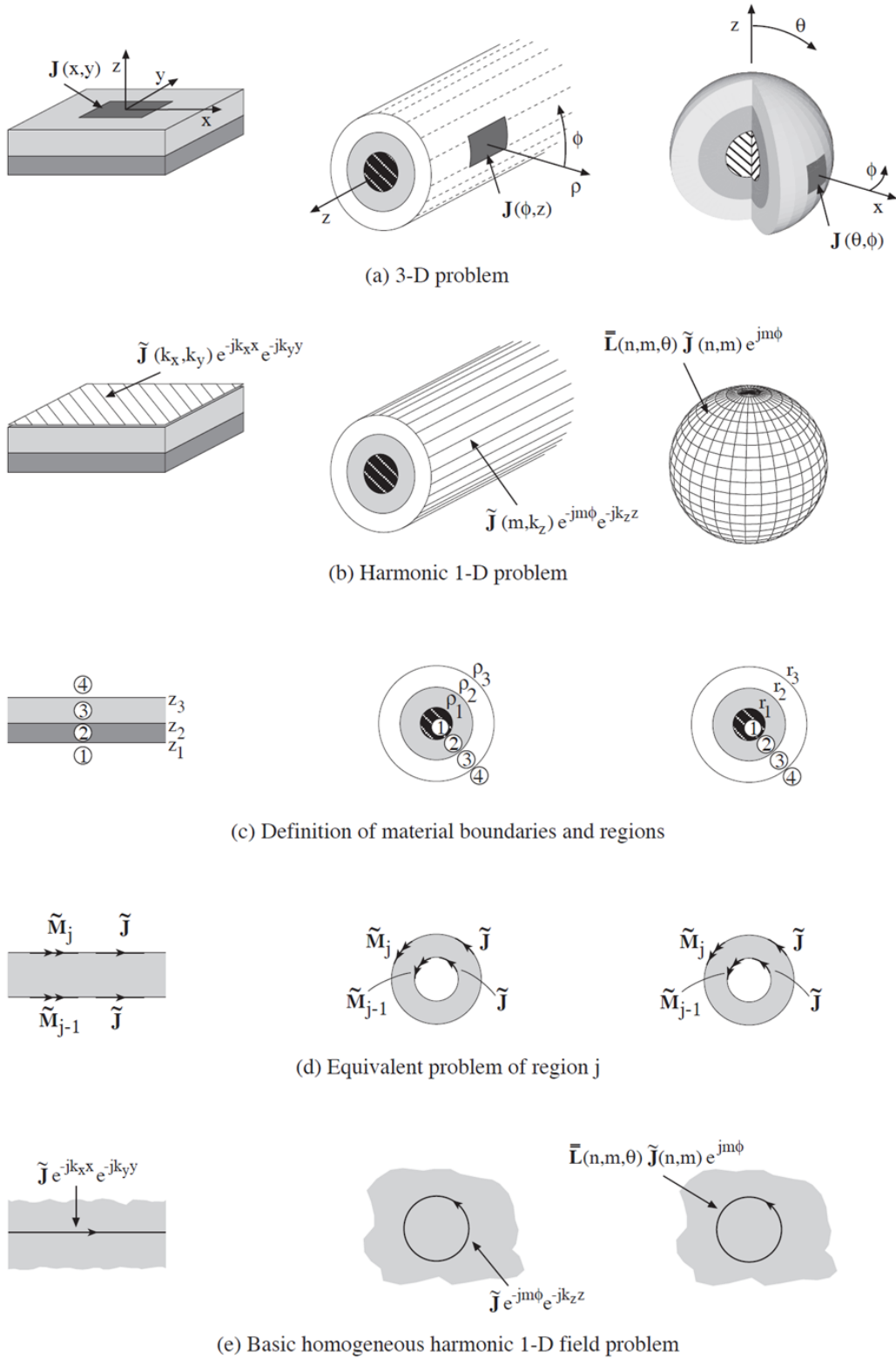


Fig. 5.3. Illustration of how a 3D problem with 1D boundary conditions of planar (left), circular cylindrical (middle) and spherical (right) type can be solved in the spectral domain by Fourier transformation of the 3D excitation currents. The spectral domain problem is illustrated in space in (b), showing the spectral excitation currents as current sheets, tubes and shells. The homogenous region Green's function used to solve the multilayer spectral problem is the field due to a current sheet, tube or shell in a homogenous region [see (c)].

element) and a multilayer structure (one of the three mentioned types), see Figure 5.3.a. Then we transform the currents in the two dimensions (using suitable variation of the two-dimensional Fourier transformation) where the structure is invariant. Doing this, the current excitation can be interpreted in space as a current sheet, tube or shell around the multilayer structure (Fig. 5.3.b). The theoretical background of the algorithm is the Love's equivalence theorem [35]. The spatial harmonic problem is subdivided into one equivalent problem per layer (Figs 5.3.c and 5.3.d) where the field in each region is formulated as the field radiated by equivalent currents at the layer boundaries. For example, the E-field in the layer j is expressed as

$$\vec{E}_j = \vec{\mathbf{G}}_{\text{EJ}}^{\text{homo}} \vec{j}_{j-1}^{\text{eq}} + \vec{\mathbf{G}}_{\text{EJ}}^{\text{homo}} \vec{j}_j^{\text{eq}} + \vec{\mathbf{G}}_{\text{EM}}^{\text{homo}} \vec{M}_{j-1}^{\text{eq}} + \vec{\mathbf{G}}_{\text{EM}}^{\text{homo}} \vec{M}_j^{\text{eq}} + \vec{\mathbf{G}}_{\text{EJ}}^{\text{homo}} \vec{j}_j^{\text{exci}} + \vec{\mathbf{G}}_{\text{EM}}^{\text{homo}} \vec{M}_j^{\text{exci}} \quad (5.68)$$

where \vec{j}_j^{eq} and \vec{M}_j^{eq} are equivalent electric and magnetic current sheets at boundary j , \vec{j}_j^{exci} and \vec{M}_j^{exci} are excitation electric and magnetic currents in layer j (if any), and $\vec{\mathbf{G}}_{\text{EJ}}^{\text{homo}}$ and $\vec{\mathbf{G}}_{\text{EM}}^{\text{homo}}$ are the Green's functions of the homogeneous structure. By using $\vec{j}_j^{\text{eq}} = \pm \hat{n} \times \vec{H}_j$ and $\vec{M}_j^{\text{eq}} = \mp \hat{n} \times \vec{E}_j$ Eq. (5.68) can be expressed in terms of the unknown tangential EM field components \vec{E}_j and \vec{H}_j at the boundary j between layers j and $j+1$ and known excitation currents. The boundary conditions that the tangential E - and H - fields are continuous at the layer boundaries give 4 linear equations per boundary. The tangential E - and H -fields are evaluated by solving the system of $4 \cdot N_{\text{boundary}}$ equations with $4 \cdot N_{\text{boundary}}$ unknowns, where N_{boundary} is the number of boundaries present in the multilayer structure. After they have been determined, the total E - and H -fields at any desired location can be found by using the equivalent problem in Fig 5.3.d. Note that the calculated EM field values are in the spectral domain, thus the 3D field solution is obtained by a 2D inverse Fourier transform of the spectral solutions. Note also that the multilayer solution process is the same for all three types of geometry; it can handle any number of layers of materials with complex permittivity and permeability. More details about the G1DMULT algorithm can be found in [30] and [31].

The BoR structures belong to the 2D class of structures, i.e. they are homogeneous only in $\hat{\phi}$ -direction. Therefore, we need perform a 1D Fourier transformation (for BoR structures we have to perform the Fourier series in $\hat{\phi}$ -direction), and by this we arrive into a spectral domain problem which is two-dimensional (2D) in space coordinates. Such spectral domains are used to analyze antennas on multiregion 2D structures which are rotationally symmetric (i.e. BoR structures), or which are infinitely long in the axial direction. The incremental sources in this spectral domain can be interpreted in space as ring currents with harmonic variation or line currents with harmonic variation, see Figure 5.4. Consequently, the Green's function is the field due to a single ring (or line) current.

We have developed a numerical algorithm called G2DMULT for calculating the Green's function of multiregion 2D structures with rotational symmetry (i.e. of multilayer BoR structures) by using the Method of Moments. The algorithm makes use of the above homogenous region Green's functions in the spectral domain in the core subroutines. A typical analysis procedure in terms of G2DMULT is illustrated in Figs. 5.4 and 5.5. We start with a 3D problem including some excitation currents (e.g. a chosen current distribution on a conformal patch element) and a multiregion 2D structure with rotational symmetry, see Fig.

5.4.a. We Fourier transform the currents in the dimensions where the structure is invariant. Doing this, the current excitation can be interpreted in space as a ring current with harmonic variation on the multilayer structure. Then, G2DMULT can be used to calculate the field solution of the multiregion structure in this spectral domain. The homogenous region Green's functions used to construct this field solution is the field of a line or ring current (Fig. 5.4.c). The 3D field solution is obtained by a 1D inverse Fourier transform of the spectral solutions.

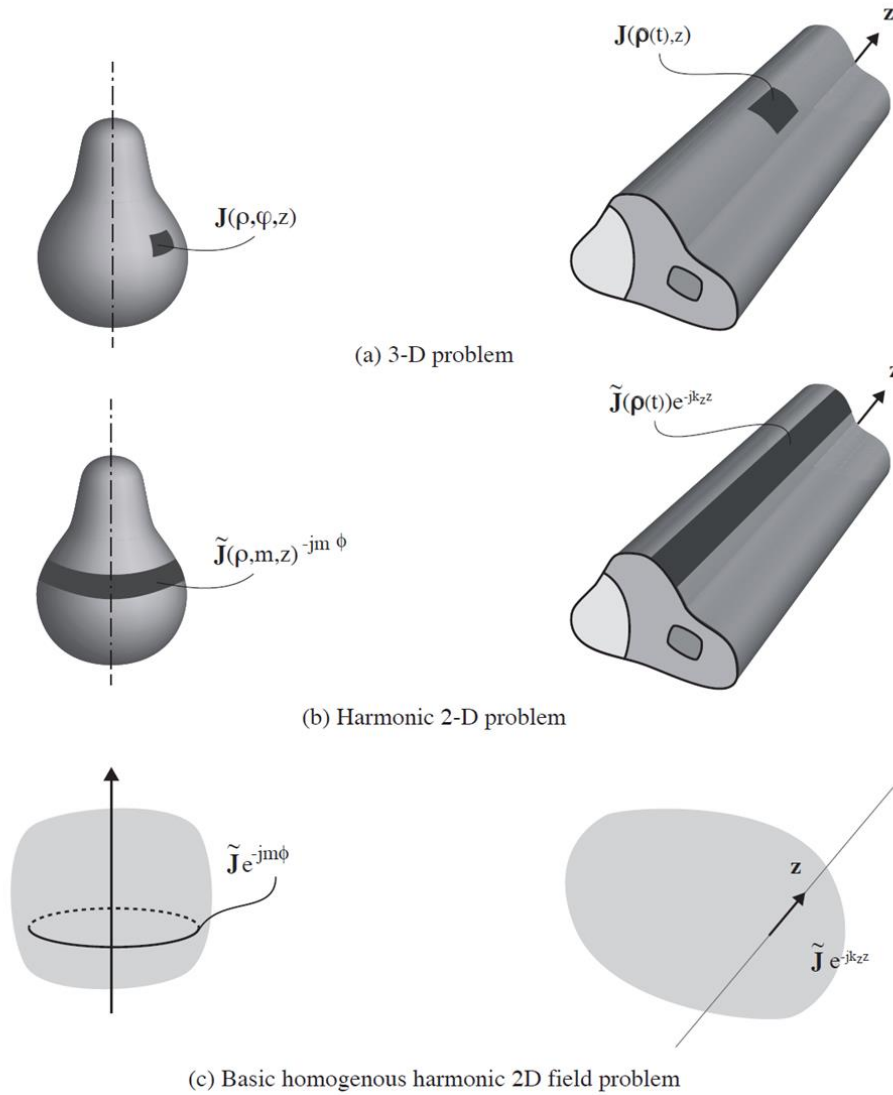


Fig. 5.4. Illustration of how a 3D problem with 2D boundary conditions or rotationally symmetric (left) and cylindrical (right) type can be solved in the spectral domain by Fourier transformation of the 3D excitation currents. The spectral domain problem is illustrated in space in (b), showing the spectral excitation currents as line and ring currents. The homogenous region Green's function used to solve the multiregion spectral problem is the field due to a ring or line current in a homogenous region [see (c)].

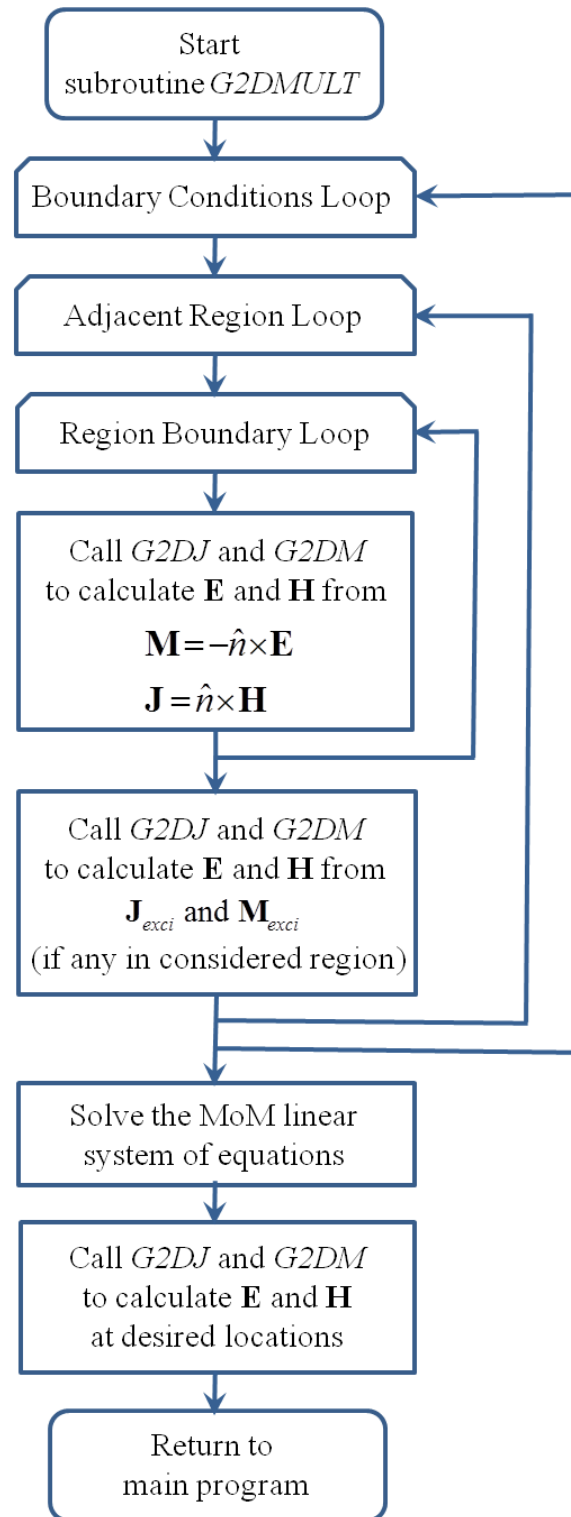


Fig. 5.5. Flowchart of the subroutine *G2DMULT*.

Fig. 5.5 shows the flow chart of the routine *G2DMULT*. The program consists of three loops inside each other. The first loop is taken over all layer boundaries, referred to as the boundary condition loop, in order to generate the 4 sets of equations per each boundary. The second loop is referred to as the adjacent region loop; it takes into account that each boundary

is surrounded by two regions. The tangential E - and H -fields components at each boundary are given by a sum of contributions from the equivalent currents from two boundaries of both adjacent regions. Therefore, the inner third loop goes over the lower and upper boundary of the considered adjacent region below or above the boundary for which the tangential E - and H -fields components are calculated. This third loop is referred to as the region boundary loop. The tangential E - and H -fields are calculated by using the two core subroutines G2DJ and G2DM. At the end of G2DMULT algorithm the MoM linear system of equations is solved by using LU decomposition, and then the output E - and H -fields are evaluated at the desired locations.

The basis of the G2DMULT algorithm can be found in [31] and the details about the cylindrical version can be found in [47]. It should be noted that the BoR version of the G2DMULT algorithm has not been developed so far.

5.5 Numerical results

We have tested the accuracy of the developed BoR program on several canonical cases. As an illustration first we have calculated the current distribution induced on a PEC cylindrical rod with hemispherical caps at the ends. The rod has $0.4 \lambda_0$ diameter and is $1.5 \lambda_0$ long, and the excitation is axially-polarized plane wave with normal incidence. The sketch of the structure and the calculated current distribution is given in Fig. 5.6. It can be seen that the calculated current distribution complies perfectly with calculation in [38]. Note that the θ -component current distribution has oscillations due to reflection from the end of the rod and has a period of $1/2 \lambda_0$ (as expected).

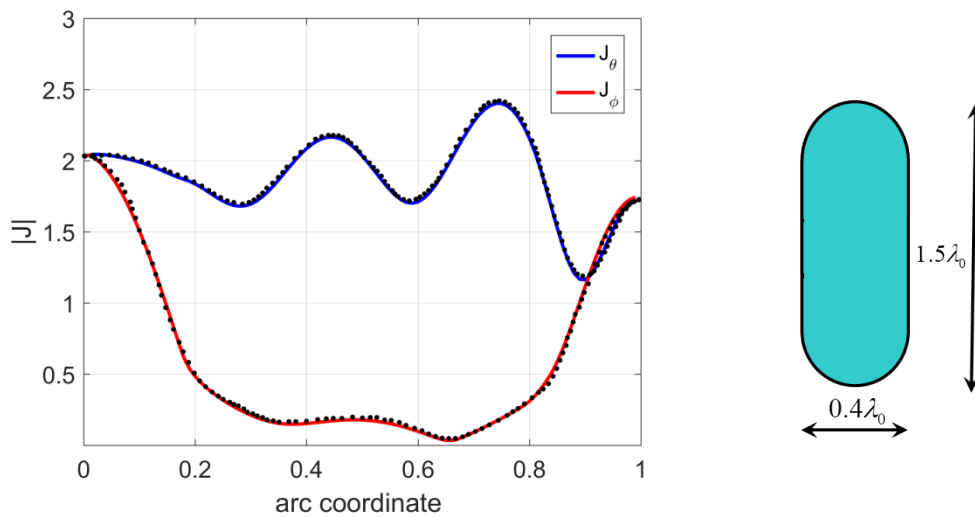


Fig. 5.6. Calculated current distribution induced on a PEC cylindrical rod; full line – results calculated with G2DMULT-BoR code, dotted line – results from [38].

As a next example let us compare the codes for 1D and 2D-BoR structures; the body that is common in both structure classes is a sphere. Therefore, let us consider a problem of scattering of EM waves from an impedance sphere (already discussed in the section 3.8). The assumed radius of the sphere is $kr_1 = 5$, and the selected value of surface impedance is $Z = j \cdot 0.15 \eta_0$. The spherical impedance surface is described with the transparent surface

impedance boundary conditions. The comparison of calculated bistatic scattering cross section using the BoR and spherical ABCD matrix programs is given in Fig. 5.7. It can be seen that there is perfect agreement between two sets of calculated results.

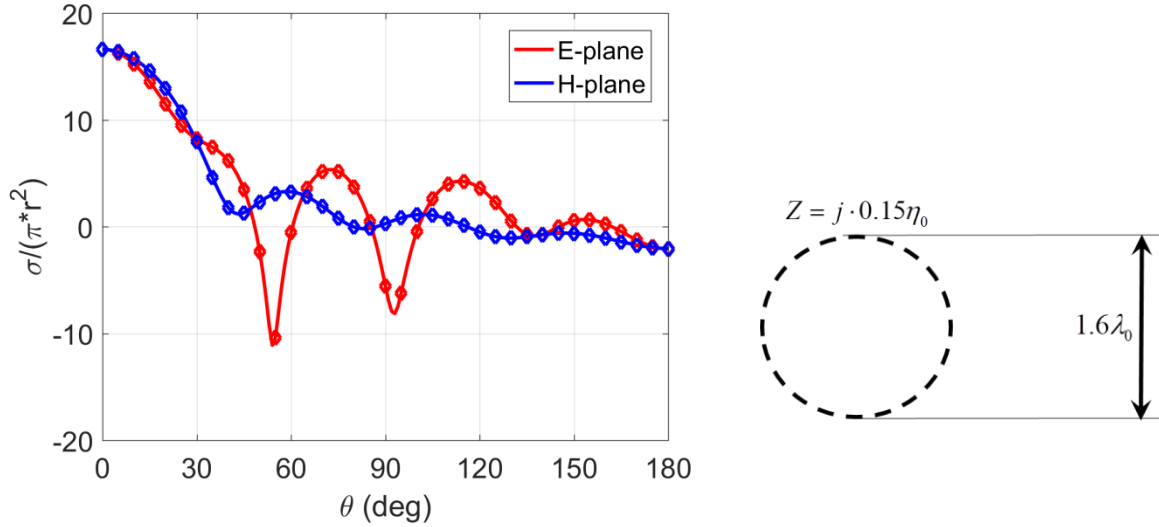


Fig. 5.7. Comparison of calculated bistatic scattering cross sections using the G2DMULT-BoR program (solid line) and the spherical ABCD matrix program (diamonds).

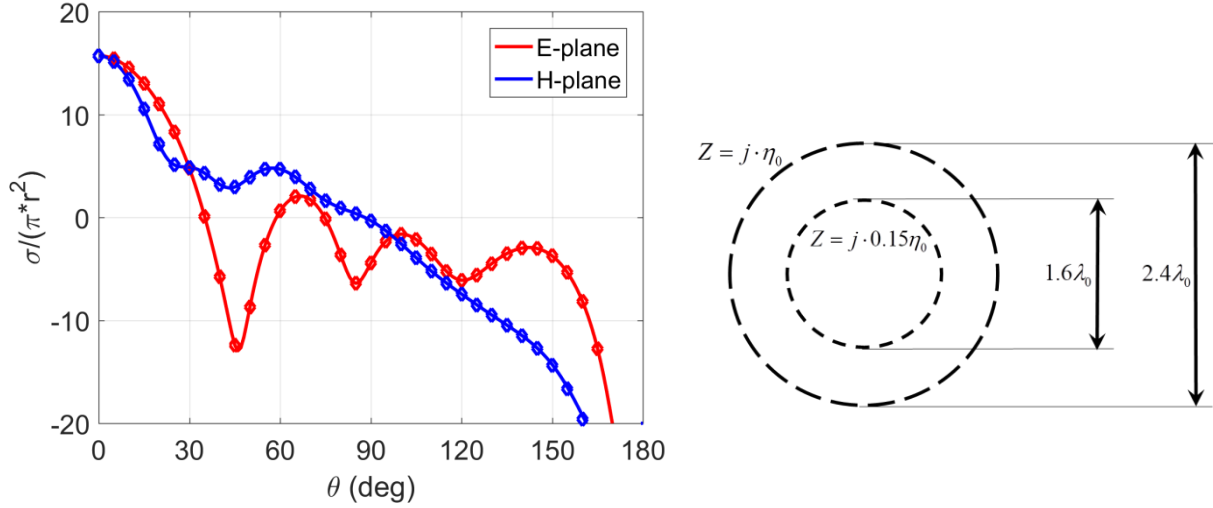


Fig. 5.8. Comparison of calculated bistatic scattering cross section using the G2DMULT-BoR program (solid line) and the spherical ABCD matrix program (diamonds).

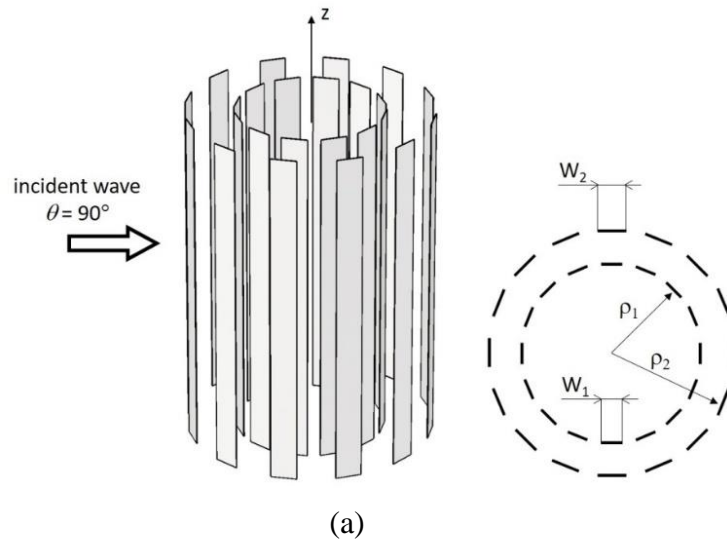
To further test the BoR code, i.e. to test the part of the code that combines equivalent sub-problems of a multiregion structure into a global electromagnetic problem, we added additional metasurface layer to previously described spherical structure in order to reduce the back-scattered field. We selected the value of surface impedance of the outer layer to be $Z = j \cdot \eta_0$, and by simple optimization procedure we determined the radius of the outer layer that gives negligible back-scattered field: $kr_2 = 7.6$. The comparison of calculated bistatic

scattering cross section using the BoR and spherical ABCD matrix programs is given in Fig. 5.8. It can be seen that again there is perfect agreement between two sets of calculated results.

As the final example let us consider the two-layer cylindrical metasurface structure described in the subsection 3.7 *Influence of mutual coupling between metasurface layers*, see Fig. 3.11 and Fig. 5.9. The outer radius of the structure ($\rho_2 = 114.6$ mm) was fixed and the inner radius was selected to be 99.6 mm and 107.1 mm, respectively. For the BoR program the length of cylinder was selected to be 1125 mm. The working frequency was set to $f = 4.0$ GHz and the excitation to a TM_z normally incident plane wave. The values of the surface sheet impedance were calculated using the MoM code for cylindrical structures [26], and the calculated values depend on the used spectral-domain component (i.e. on the Fourier harmonic) of the impinging field. In Fig. 5.9, the calculated scattering pattern is plotted. The bistatic radar cross section σ_{3D} and the bistatic scattering width σ_{2D} are connected using the approximate formula for long cylindrical structures [48]:

$$\sigma_{3D} \approx \sigma_{2D} \frac{2L^2}{\lambda_0} \quad (5.69)$$

where L is the length of the structure (15 wavelengths in the considered case). There is excellent agreement between the two methods, the ABCD transmission matrix approach and the BoR code, despite the fact that the BoR program analyzes three-dimensional structures while the ABCD transmission matrix program analyzes two-dimensional structures.



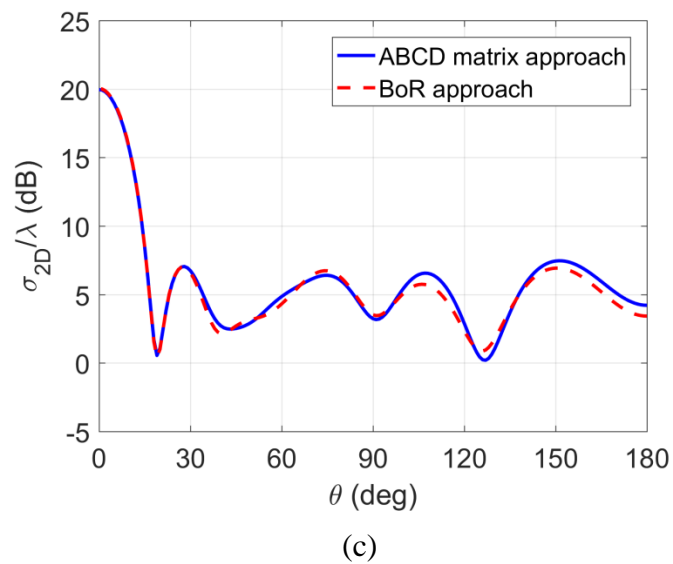
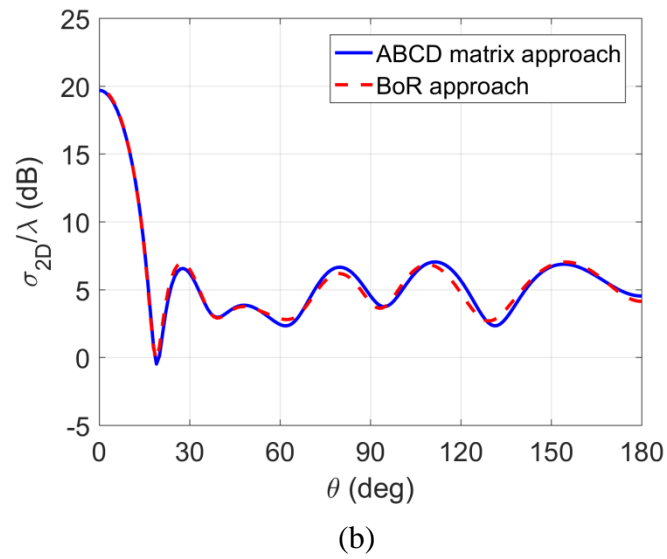


Fig. 5.9. Scattering pattern of two-layer cylindrical metasurface; (a) sketch of the analyzed structure, distance between two metasurface layers is: (b) 0.2λ , and (c) 0.1λ .

Measured results

In this chapter we will present design and measurements of several prototypes of curved metasurface structures. The common goal behind all considered prototypes is to reshape the radiation pattern of the feed antenna and by this to act as a metasurface lens. The considered metasurfaces work in transmitting mode, i.e. the radiation pattern is formed by transmitting the EM waves, originating from the feed antenna, through the curved metasurface.

6.1 Single-layer cylindrical metasurface

The first prototype consists of a single-layer cylindrical metasurface printed on a thin substrate. The metasurface substrate is curved then to cylindrical shape of desired radius (6 cm). Only the half of considered cylindrical surface is covered with the metasurface. If the feed antenna has an omnidirectional radiation pattern, such as a monopole or a dipole, the reshaped pattern should have two maximums at $\pm 45^\circ$ and the broadside radiated pattern should be reduced for approximately 10 dB comparing to the maximum at $\pm 45^\circ$. If the feed antenna is more directive (like a waveguide opening or a horn) the modified radiation pattern will have a broader main beam, i.e. the beamwidth will be enlarged.

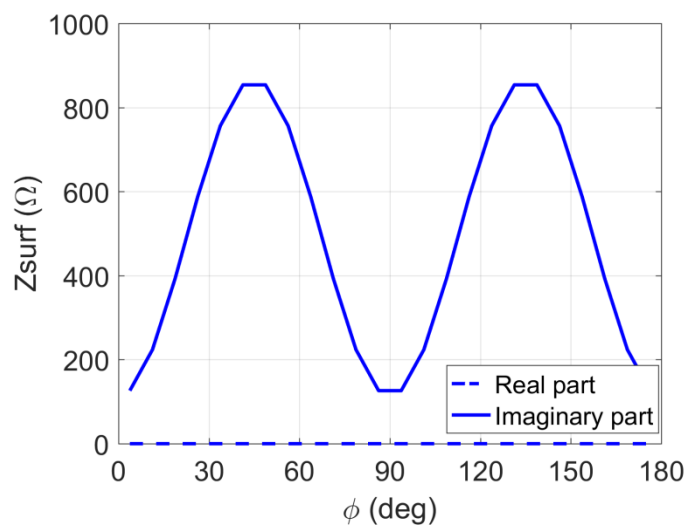
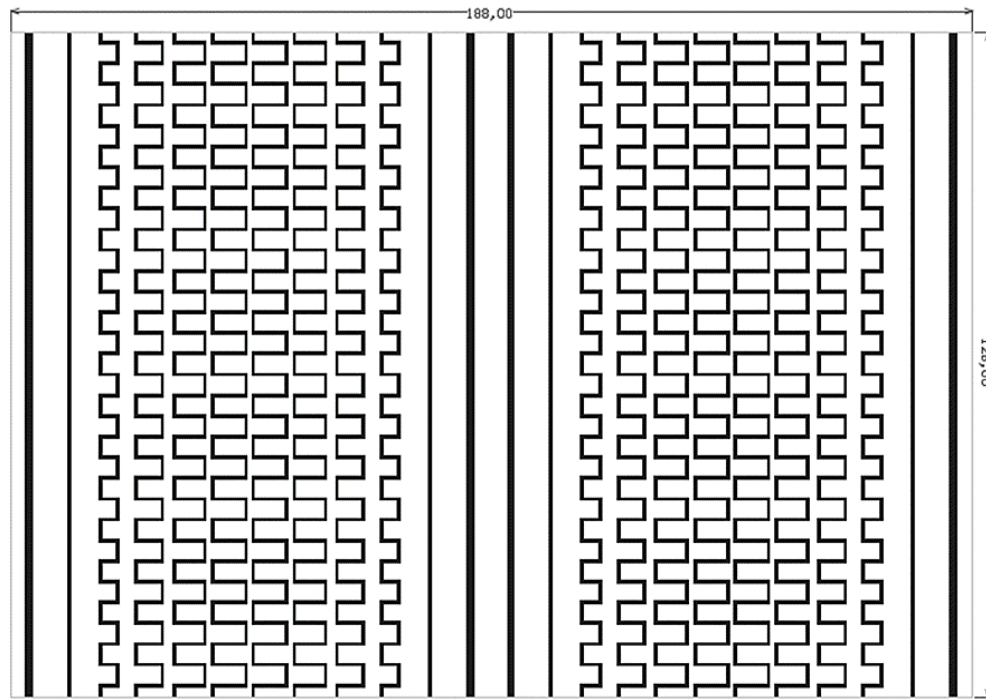
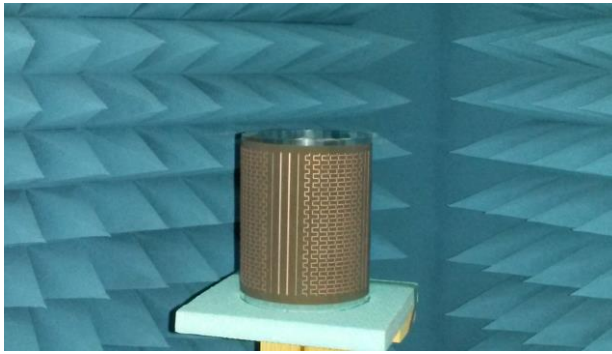


Fig. 6.1. Surface impedance profile for the cylindrical metasurface

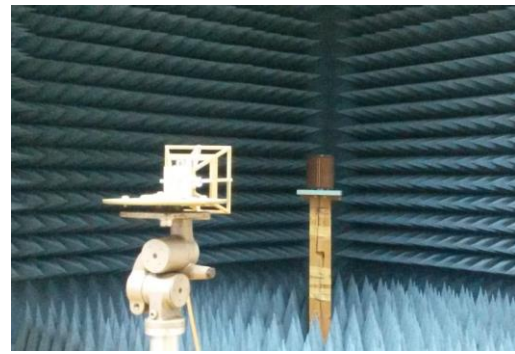
The required impedance profile for a half-cylinder is given in Fig. 6.1. In this single-layer design the impedance profile is fully inductive throughout the surface and it can be simply realized using printed metallization based on printed straight and meander lines, see Fig 6.2.



(a)



(b)



(c)

Fig. 6.2. Realization of the single-layer printed metasurface; (a) Layout of the metallization, (b) image of the cylindrical metasurface mounted on a dielectric support, (c) measurement setup.

The design of the structure is based on modulating the surface impedance to comply with the required impedance profile using inductive impedance lines as shown in Fig. 6.2.a. Using a standard PCB technology this profile is printed on a flexible substrate ($\epsilon_r = 2.55$, $h = 0.13$ mm) and curved to shape a half-cylinder with a radius of 60 mm. All the geometry details are given in the Table 6.1 below and the photos of the structure mounted on a support dielectric cylinder and the measurement setup are shown in Figs. 6.2.b and 6.2.c.

TABLE 6.1 DETAILS OF THE DESIGN OF SINGLE-LAYER CYLINDRICAL METASURFACE STRUCTURE CONTAINING 24 SEGMENTS: THE STRAIGHT STRIPLINES HAVE VARIABLE LINE WIDTH AND THE MEANDER LINES HAVE FIXED LINE WIDTH AND VARIABLE TOTAL WIDTH. THE RADIUS OF THE CYLINDRICAL METASURFACE STRUCTURE IS 60 MM AND THE CENTRAL WORKING FREQUENCY IS 10 GHz. DUE TO SYMMETRY ONLY $\frac{1}{4}$ OF THE STRUCTURE IS DESCRIBED

Segment No.	Type of the metasurface structure	Width of the stripline	Total width of the meander line	Calculated surface sheet impedance (spectral-domain approach)	Calculated surface sheet impedance (CST Microwave Studio)
1	stripline	$w = 1.3 \text{ mm}$	-	$j \cdot 126.16 \Omega$	$j \cdot 129.99 \Omega$
2	stripline	$w = 0.5 \text{ mm}$	-	$j \cdot 223.66 \Omega$	$j \cdot 215.33 \Omega$
3	meanderline	$w = 0.5 \text{ mm}$	$h = 3.5 \text{ mm}$	$j \cdot 392.53 \Omega$	$j \cdot 398.53 \Omega$
4	meanderline	$w = 0.5 \text{ mm}$	$h = 5.15 \text{ mm}$	$j \cdot 587.52 \Omega$	$j \cdot 590.92 \Omega$
5	meanderline	$w = 0.5 \text{ mm}$	$h = 6.1 \text{ mm}$	$j \cdot 756.39 \Omega$	$j \cdot 756.71 \Omega$
6	meanderline	$w = 0.5 \text{ mm}$	$h = 6.5 \text{ mm}$	$j \cdot 853.89 \Omega$	$j \cdot 858.34 \Omega$

It can be seen that the required surface sheet impedance can be realized using the “classical” single-line straight strips (lower values of surface reactance) and meander lines that fit into the selected segment representing one metasurface cell (higher values of surface reactance; the selected width of each segment was 7.85 mm). The desired value of the surface reactance was obtained by changing the width of the stripline and the total width of the meander line structure (see Appendix 1 where we will discuss typical values of surface impedance that can be achieved with different metasurface patterns).

In the following part of the section the properties of this design will be investigated through measurements and simulations, confirming the validity of the design and the modeling approach. For the measurements, different excitation feeds were used and the setup was mounted in our laboratory with mobile anechoic walls.

6.1.1. Monopole feed - curved metasurface printed on a thin substrate with no support layer

We start the presentation of the results related to this test structure by showing the pattern which the designed metasurface produces when excited by a simple monopole feed. The metasurface itself is printed on a very thin dielectric substrate which can be easily manipulated and curved to exactly form a cylinder with 60 mm radius. The measured radiation pattern in polar coordinates for the monopole itself mounted on our rotational stage enclosed by anechoic walls is shown in Fig. 6.3.a. These results verified the expected omnidirectional pattern and ensured us that there are no spurious reflections that could affect the results when the metasurface was added. The measured pattern with the metasurface for the frequency range of interest is shown in Fig. 6.3.b. The varying surface impedance of the metasurface produces amplitude and phase modulation which in effect reshape the radiation pattern as desired.

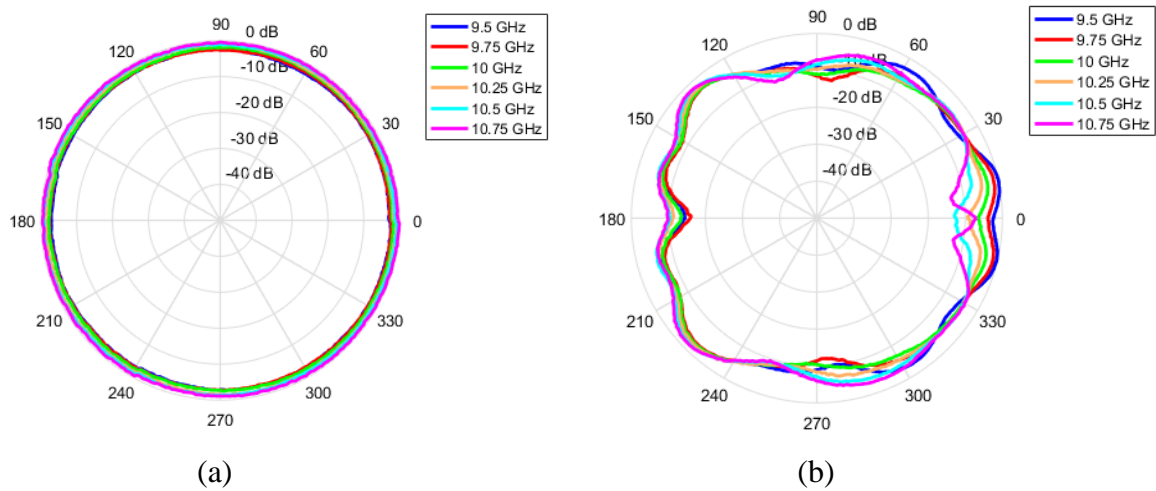


Fig. 6.3. Measured radiation patterns for; (a) monopole feed, (b) monopole feed with single layer metasurface.

A more detailed look at the measured results at 10 GHz is shown in Fig. 6.4.a with a direct comparison of the pattern with and without the metasurface showing the potential of this “a posteriori” control of the pattern. Note that the measured pattern of the metasurface structure is normalized with the measured gain of monopole feeding antenna.

The measured results are further compared with the results of the developed spectral-domain analysis method and the results obtained with CST Microwave Studio [37] used as commercial reference tool. Note that the spectral-domain method uses the surface sheet impedance approach, while the CST Microwave Studio results are calculated by considering the developed metasurface geometry with all details (i.e. without the intermediate step of using the surface sheet impedance). Consequently, the needed computer time is several orders of magnitude larger when using the commercial software package. Both analysis tools predict well the main lobes although there is a few degrees shift probably due to small prototype manufacturing or alignment offset. In the null of the pattern both methods deviate from the measurements, but still recreate the main shape.

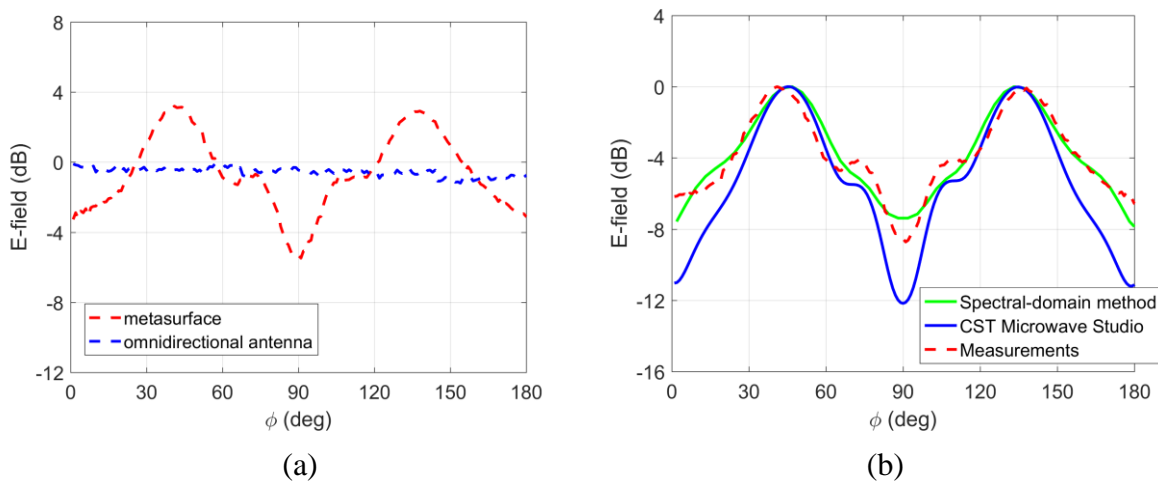


Fig. 6.4. Radiation pattern for the designed metasurface; (a) measured patterns without and with the metasurface, (b) comparison between measurements, developed spectral-domain method results and CST MS results.

These results are shown in more details in Fig. 6.5 where one-to-one comparison of both methods with the measurements is shown. Spectral-domain method as seen agrees very well with the measured results in the front segment, however it doesn't recreate the backward radiation so well. This is due to complicate reflection mechanism within a cylindrical metasurface concave reflector. Direct comparison of the measurements with CST MS results also reveals similar problems with the inaccurate prediction of backward radiation, but it also shows that the results for the forward direction have a more significant reduction in the radiation pattern in broadside direction compared to developed spectral-domain method.

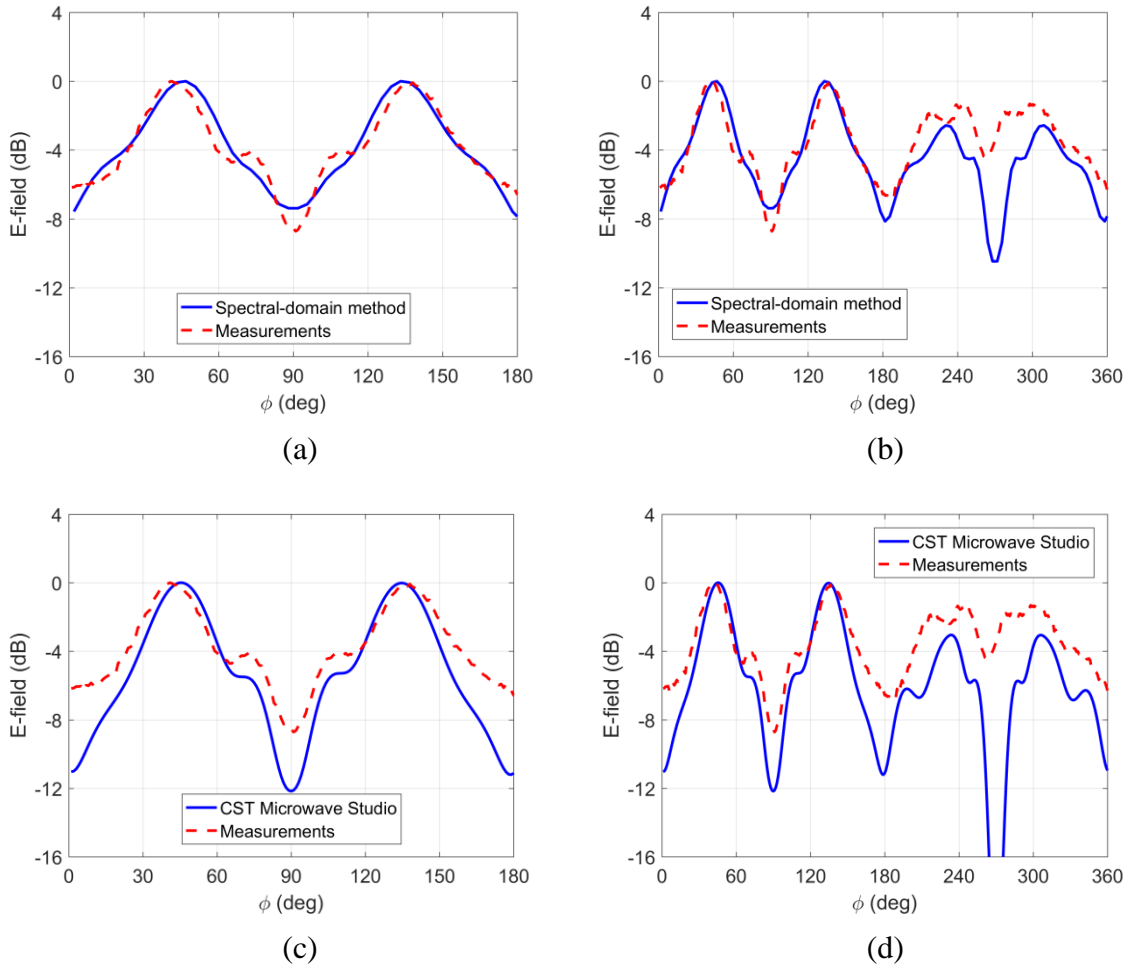
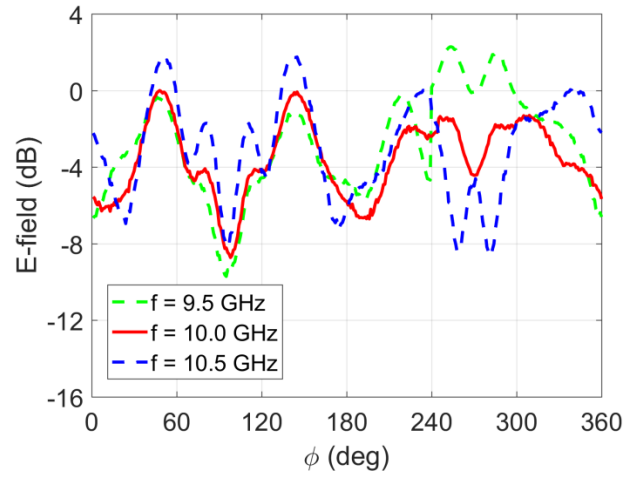
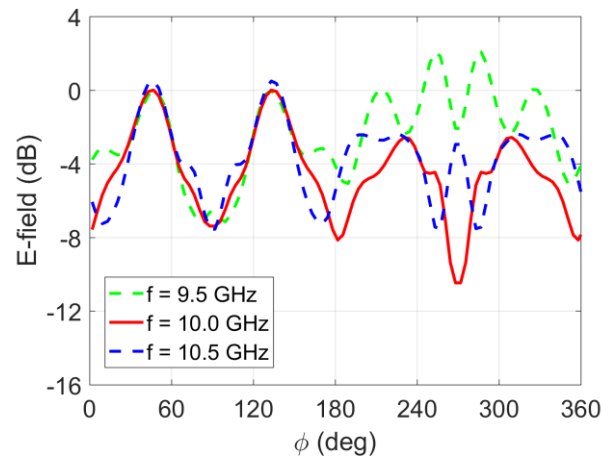


Fig. 6.5. Radiation patterns for the designed metasurface; (a) comparison of measured results and developed SD method for forward direction, (b) comparison of measured results and developed SD method for the entire angular range, (c) comparison of measured results and CST MS results for forward direction, (d) comparison of measured results and CST MS results for the entire angular range.

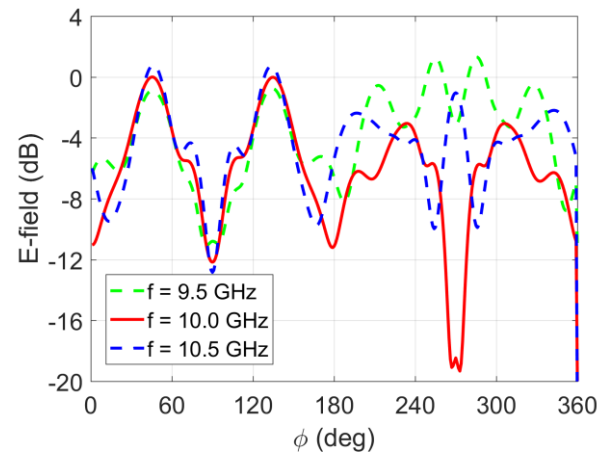
Finally, the frequency dependence for all three sets of results (measurements, spectral-domain, CST MS) is shown in Fig. 6.6. It shows that the pattern in the forward direction is reasonably stable, but in the backward direction it significantly varies with frequency due to reflections from the front metasurface sheet (the angular area occupied with the metasurface sheet is 180°).



(a)



(b)



(c)

Fig .6.6. Frequency dependence of radiation pattern; (a) measurements, (b) spectral-domain approach, (c) CST Microwave Studio.

6.1.2. Monopole feed - curved metasurface is printed on a thick substrate support layer

The second set of results for this design of the metasurface investigates how an additional dielectric support layer with parameters $\epsilon_r = 2.6$, $h = 3.0$ mm will affect the radiation properties of the metasurface. As in the first case, we start by observing the radiation patterns in polar coordinate system (Fig.6.7) of the monopole itself without a supporting dielectric structure and with the metasurface around it for different frequencies and expand on these results to gain more insight into the details at the operating frequency of 10 GHz.

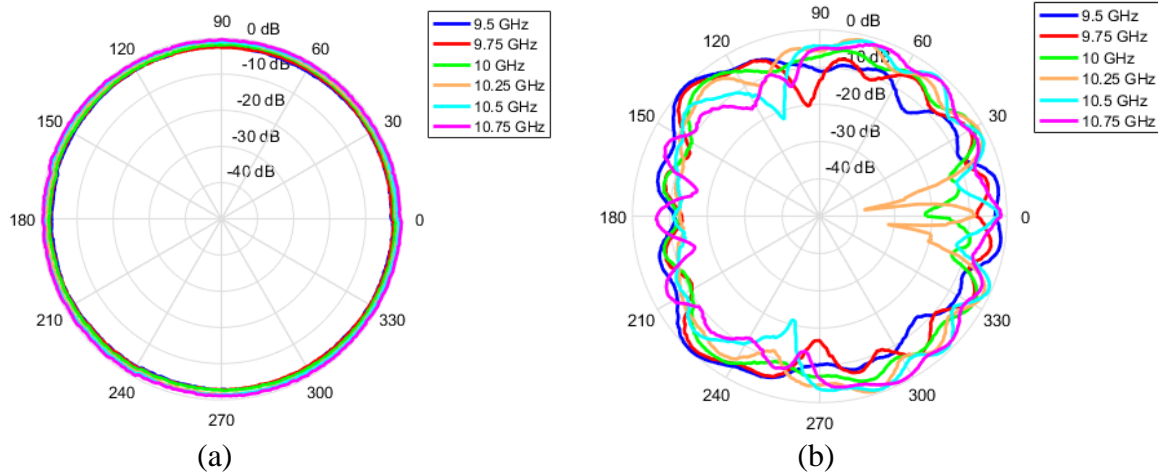


Fig. 6.7. Measured radiation patterns for; (a) monopole feed, (b) monopole feed with single-layer metasurface and supporting dielectric layer.

Compared to previous set of results the radiation pattern has more pronounced minor lobes (Fig. 6.8.) in the forward direction, but the main lobes remained at 45 degrees. Both analysis methods predict well the positions of the peaks with only minor deviations which become more pronounced as we move towards the backward radiation. Also, from direct comparisons with measurements (Fig. 6.9.) we see that the spectral-domain method predicts the amplitude levels more precisely than CST MS.

As expected, this case due to thicker dielectric with higher permittivity introduces more pronounced resonances in the pattern due to reflections inside the metasurface cylinder, but although the amplitudes of these are not well predicted, the positions are quite accurately estimated with the spectral-domain method. This shows that the developed approach is robust enough to handle quite complex metasurface structures.

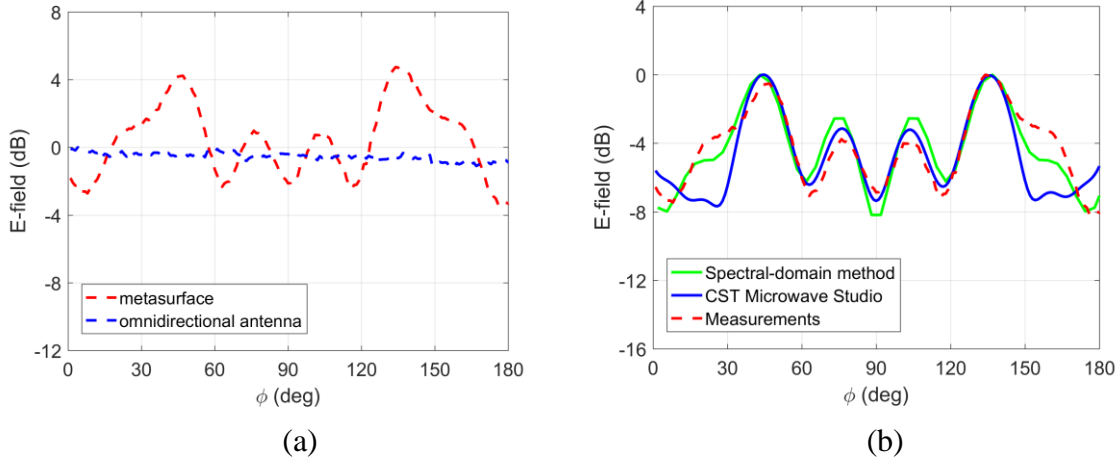


Fig. 6.8. Radiation pattern for the designed metasurface with dielectric supporting structure; (a) measured patterns without and with the metasurface, (b) comparison between measurements, developed spectral-domain method results and CST MS results.

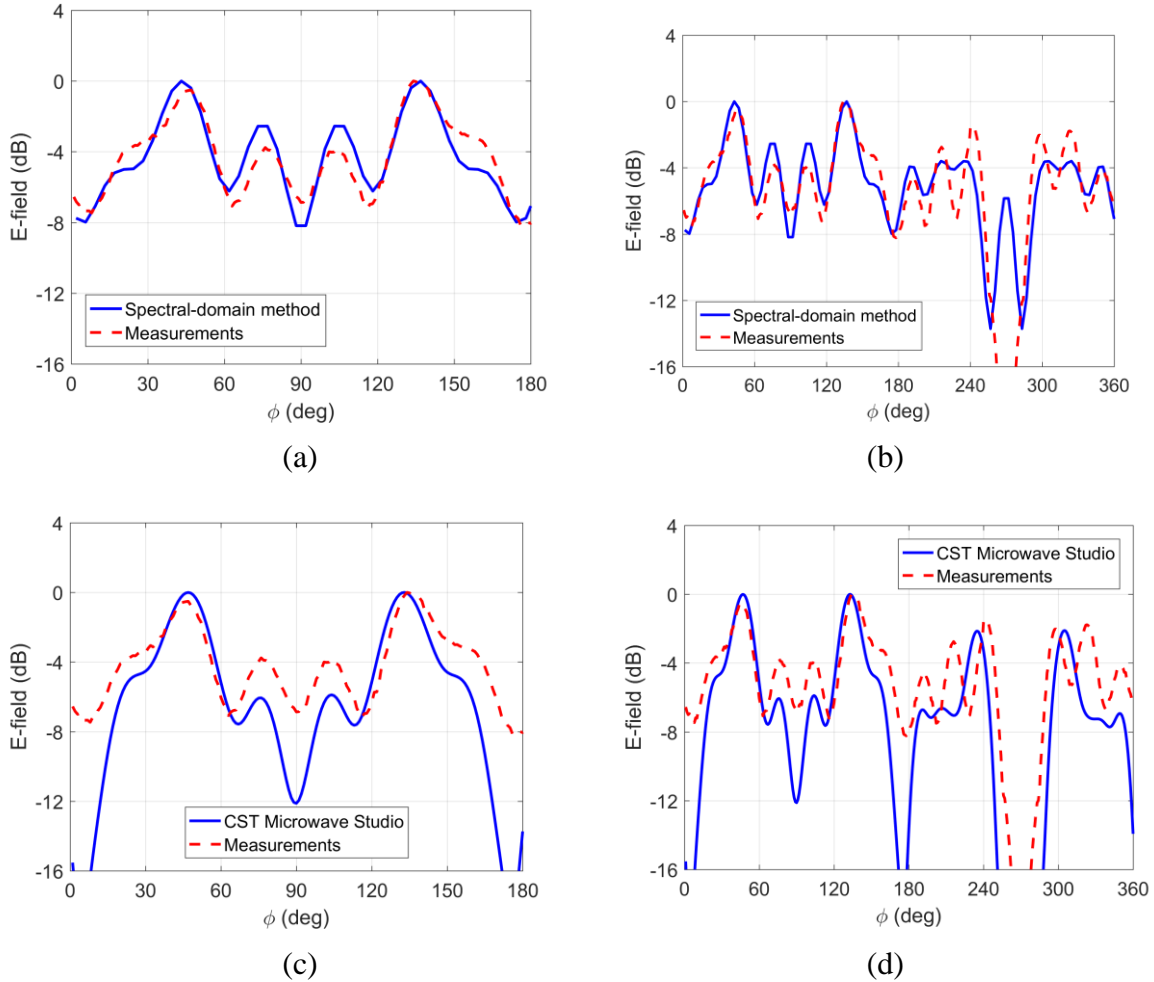


Fig. 6.9. Radiation patterns for the designed metasurface with dielectric support; (a) comparison of measured results and developed SD method for forward direction, (b) comparison of measured results and developed SD method for the entire angular range, (c) comparison of measured results and CST MS results for forward direction, (d) comparison of measured results and CST MS results for the entire angular range.

6.1.3. Waveguide feed - curved metasurface printed on a thin substrate with no support layer

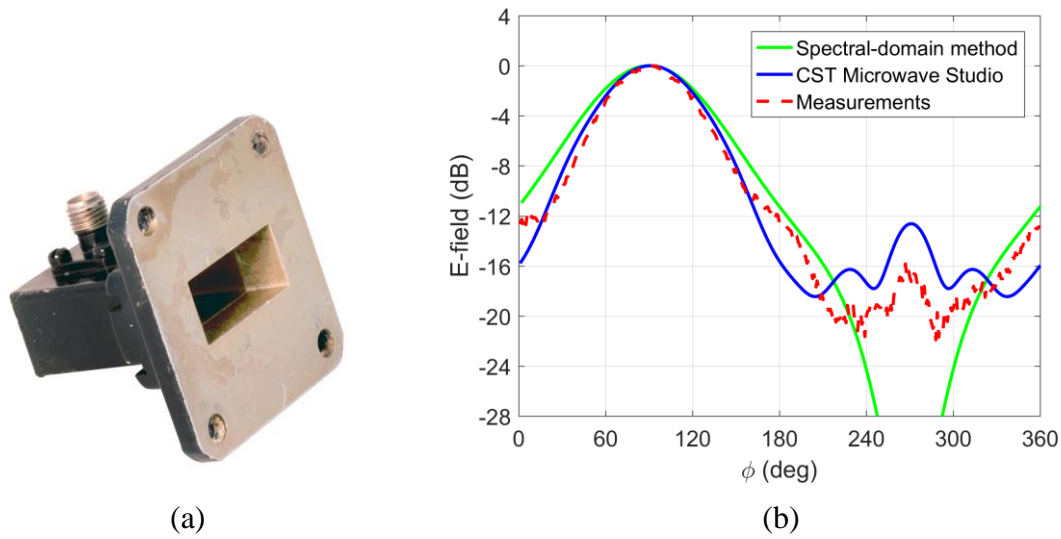


Fig. 6.10. Used waveguide feed and its radiation pattern; (a) photo of the WR-90 feed, (b) comparison of measured, SD method and CST MS computed radiation patterns.

The same metasurface structure (without the thick dielectric support layer) is excited in this case with WR-90 waveguide to verify the developed method for a more complex feed situation. The waveguide and its radiation pattern in free space are shown in Fig.6.10. While measurements and CST MS results agree very well, the spectral domain method cannot accurately predict the backward radiation from the realistic feed. This is due to simple feed model of an open waveguide – we simply applied the Love equivalence principle to the EM field distribution at the waveguide opening. This however is not a critical issue from the modeling perspective since the effect of this backward radiation will be negligible compared to metasurface reflection as it will be shown.

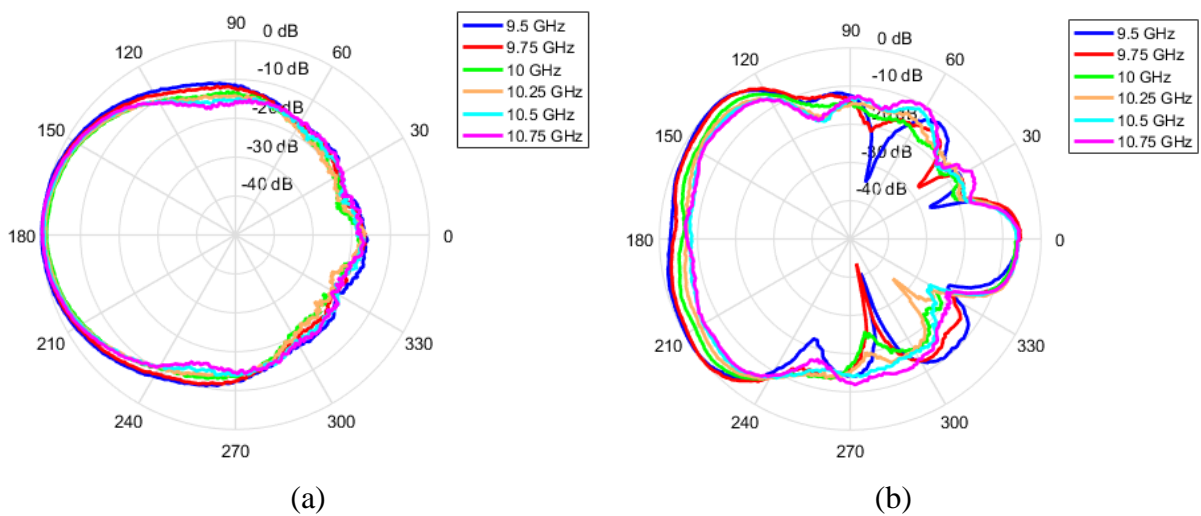


Fig. 6.11. Measured radiation patterns for; (a) WR-90 waveguide feed, (b) WR-90 waveguide feed with single layer metasurface.

Measured results in Fig. 6.11. show the frequency dependence for the waveguide radiation without and with the metasurface. This is visualized more closely in Fig. 6.12 separately for forward radiation and the full 360 deg. The metasurface effect produces again the splitting of the main beam for $\pm 45^\circ$ directions. Unlike the monopole case, there is a strong reflection in the backward direction which is a consequence of the fact that a single layer metasurface cannot be designed to reshape the radiation pattern with zero reflections.

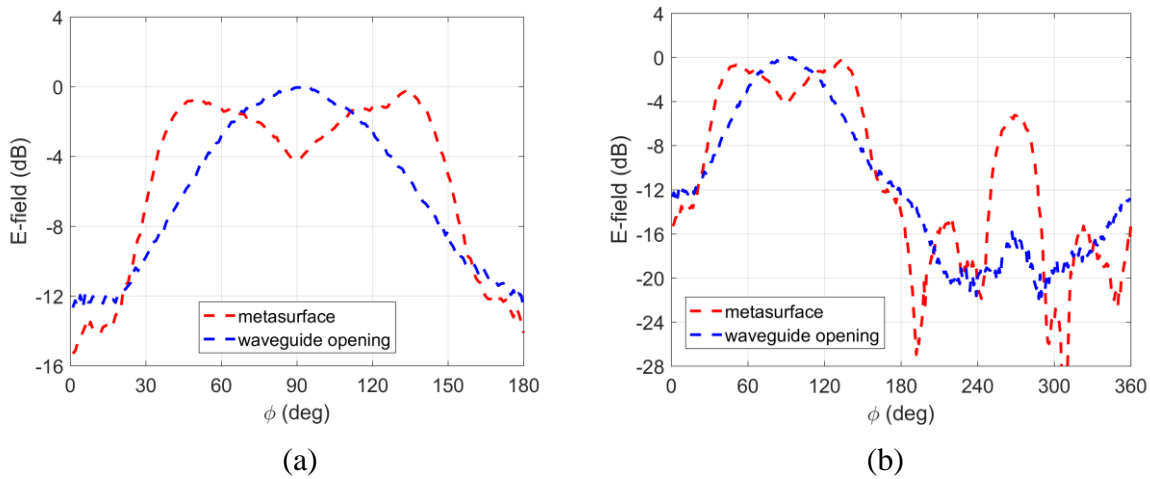
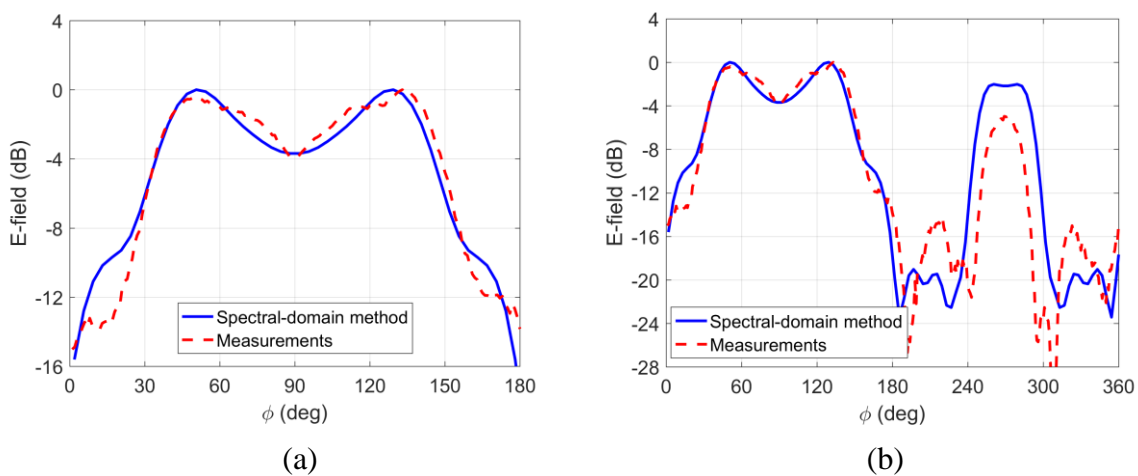


Fig. 6.12. Comparison between measured radiation patterns for waveguide feed without and with the metasurface; (a) only forward direction, (b) full angular pattern.

The developed SD method shows results which agree very well with the measurements as seen in Fig. 6.13. The agreement is not perfect in the backward direction (for the reflection from the metasurface), but also CST MS results fail to accurately predict this part of the pattern (as seen in Fig. 6.13.d).

The analysis of the frequency dependence in Fig. 6.14. reveals that the pattern is very stable in the forward direction. In the backward direction the reflection part is naturally also unchanged, but other segments change quite significantly with frequency.



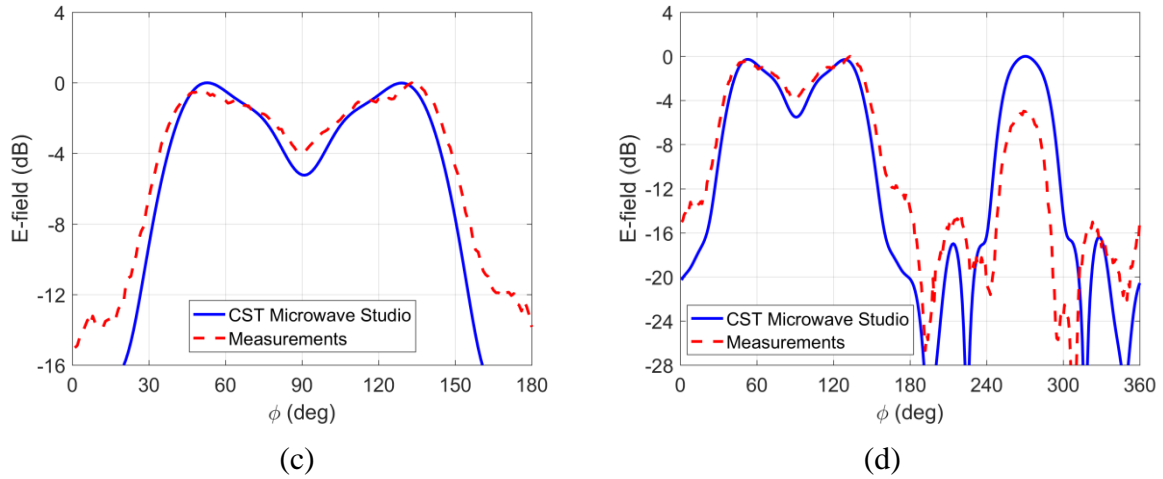


Fig. 6.13. Radiation patterns for the designed metasurface with waveguide feed; (a) comparison of measured results and developed SD method for forward direction, (b) comparison of measured results and developed SD method for the entire angular range, (c) comparison of measured results and CST MS results for forward direction, (d) comparison of measured results and CST MS results for the entire angular range.

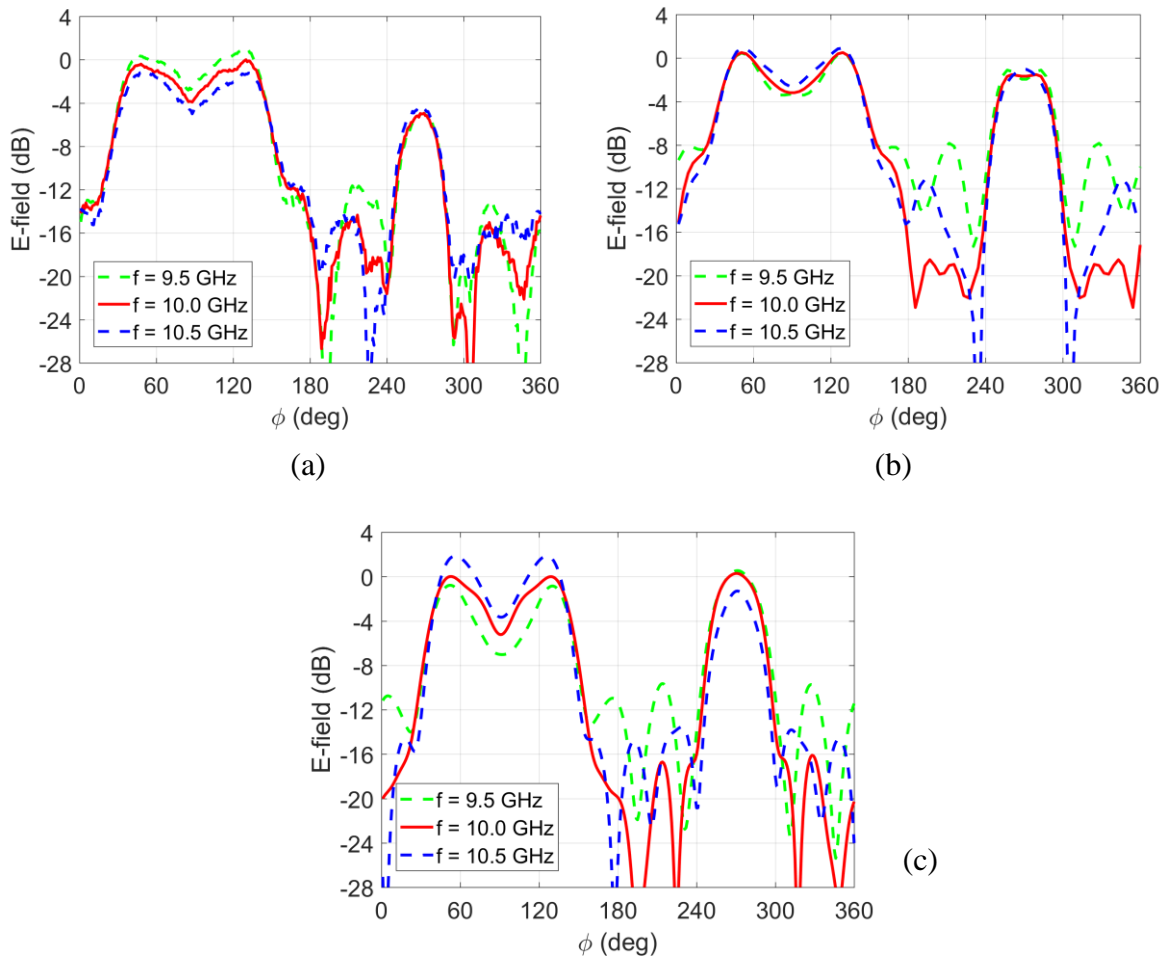
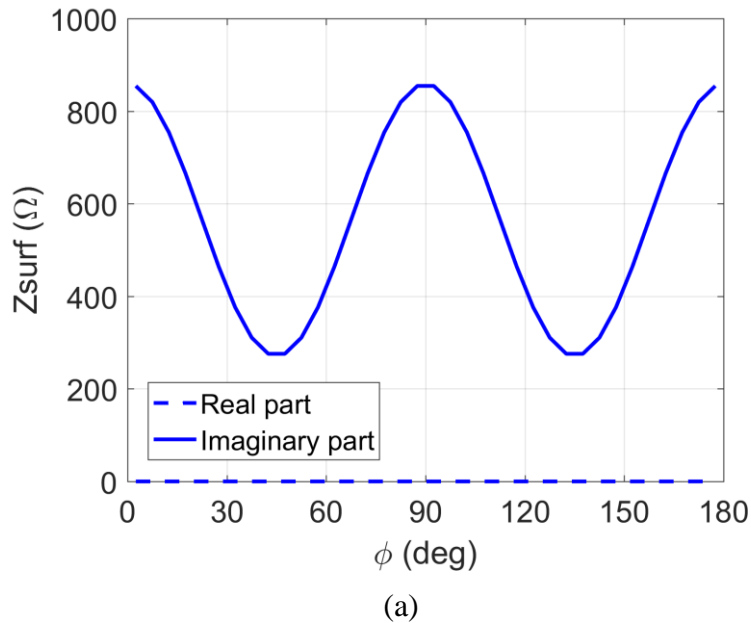


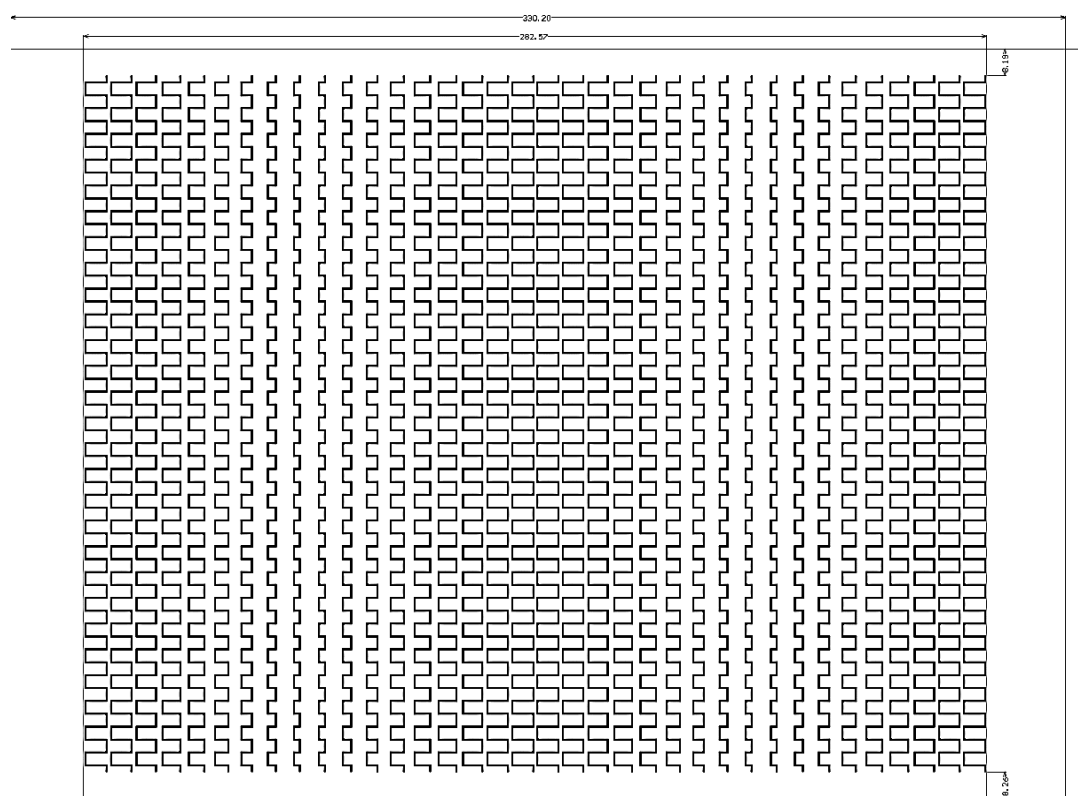
Fig. 6.14. Frequency dependence of radiation pattern; (a) measurements, (b) spectral domain approach, (c) CST Microwave Studio.

6.2 Two-layer cylindrical metasurface

As indicated before, a multilayer metasurface structure allows gives us more degrees of freedom when aiming to manipulate radiation pattern or similar wave properties. This will be demonstrated with a prototype designed for 10 GHz which consists of two identical metasurface layers. The design goal was to enhance the gain of the feed antenna and at the same time reduce the backscattering from the metasurface structure which was not possible with single-layer design.

The impedance profile and the metallization pattern needed for realization are show in Fig 6.15. Using a standard PCB technology this profile is printed on both sides of a flexible substrate and curved to shape a half-cylinder with a radius of 90 mm. The used substrate is IsoClad 933 laminate from Rogers Corporation with permittivity $\epsilon_r = 2.33$ and thickness $h = 1.55$ mm. One of the predicted applications of this substrate is realization of conformal antennas, thus the substrate is highly flexible (the flexural modulus is 239 kpsi which is one order of magnitude lower value than for usual microwave substrates), and it was possible to bend it to form a cylinder of radius 90 mm as shown in Fig. 6.16. All the geometry details are given in the Table 6.2 below and the photos of the structure mounted on a support dielectric cylinder and the measurement setup are shown in Figs. 6.16.





(b)

Fig. 6.15. Surface impedance profile for the cylindrical metasurface (used in two-layer case); (a) impedance values, (b) metallization profile.



Fig. 6.16. Image of a cylindrical metasurface with a monopole feed antenna.

TABLE 6.2 DETAILS OF THE DESIGN OF TWO-LAYER CYLINDRICAL METASURFACE STRUCTURE
 THE RADIUS OF THE CYLINDRICAL METASURFACE STRUCTURE IS 90 MM AND THE CENTRAL WORKING FREQUENCY IS 10 GHz. DUE TO SYMMETRY ONLY $\frac{1}{4}$ OF THE STRUCTURE IS DESCRIBED

Segment No.	Type of the metasurface structure	Angular position	Width of the stripline	Total width of the meander line	Calculated surface sheet impedance
1	meanderline	2.5°	0.5 mm	6.6 mm	$j \cdot 854.41 \Omega$
2	meanderline	7.5°	0.5 mm	6.4 mm	$j \cdot 819.51 \Omega$
3	meanderline	12.5°	0.5 mm	6.05 mm	$j \cdot 753.92 \Omega$
4	meanderline	17.5°	0.5 mm	5.56 mm	$j \cdot 665.54 \Omega$
5	meanderline	22.5°	0.5 mm	4.85 mm	$j \cdot 565.05 \Omega$
6	meanderline	27.5°	0.5 mm	4.15 mm	$j \cdot 464.56 \Omega$
7	meanderline	32.5°	0.5 mm	3.3 mm	$j \cdot 376.18 \Omega$
8	meanderline	37.5°	0.5 mm	2.5 mm	$j \cdot 310.59 \Omega$
9	meanderline	42.5°	0.5 mm	1.83 mm	$j \cdot 275.69 \Omega$

6.2.1. Waveguide feed - curved two-layer metasurface

Realized two-layer metasurface is illuminated by a waveguide feed WR-90 (shown in Fig. 6.10.a) and produces radiation patterns as shown in Fig. 6.17. From comparison with a standalone waveguide feed we see the focusing effect which was obtained by using this metasurface. The patterns are directly compared in Fig. 6.18. for the design frequency (10 GHz) and the gain improvement is clearly seen (note that the patterns are normalized with the gain of waveguide opening feeding antenna). Also, compared to the previous single-layer case there is no pronounced reflection in the backward direction from the metasurface.

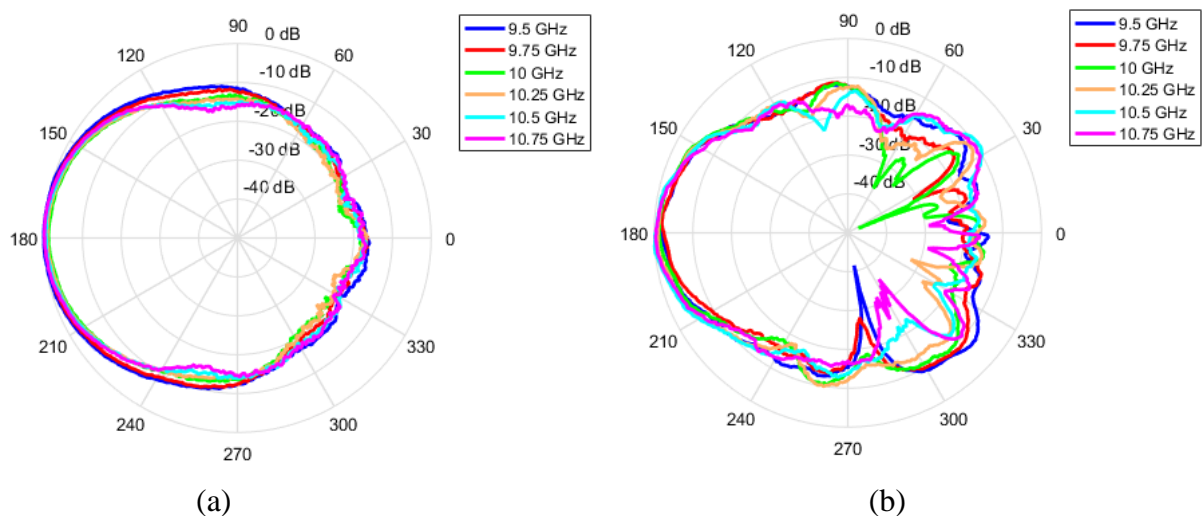


Fig. 6.17. Measured radiation patterns for; (a) WR-90 waveguide feed, (b) WR-90 waveguide feed with two-layer metasurface.

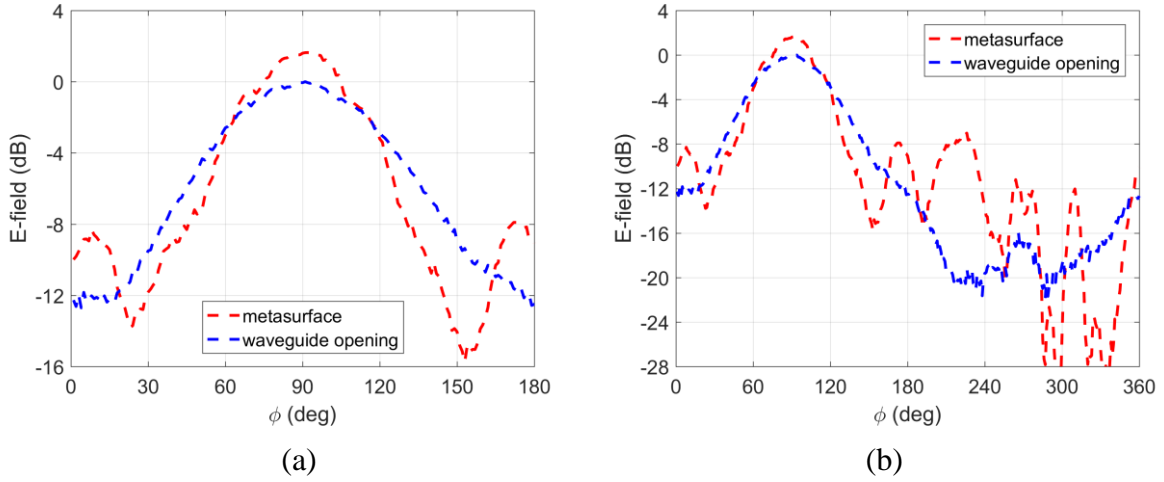


Fig. 6.18. Comparison between measured radiation patterns at 10 GHz for waveguide feed without and with the two-layer metasurface; (a) only forward direction, (b) full angular pattern.

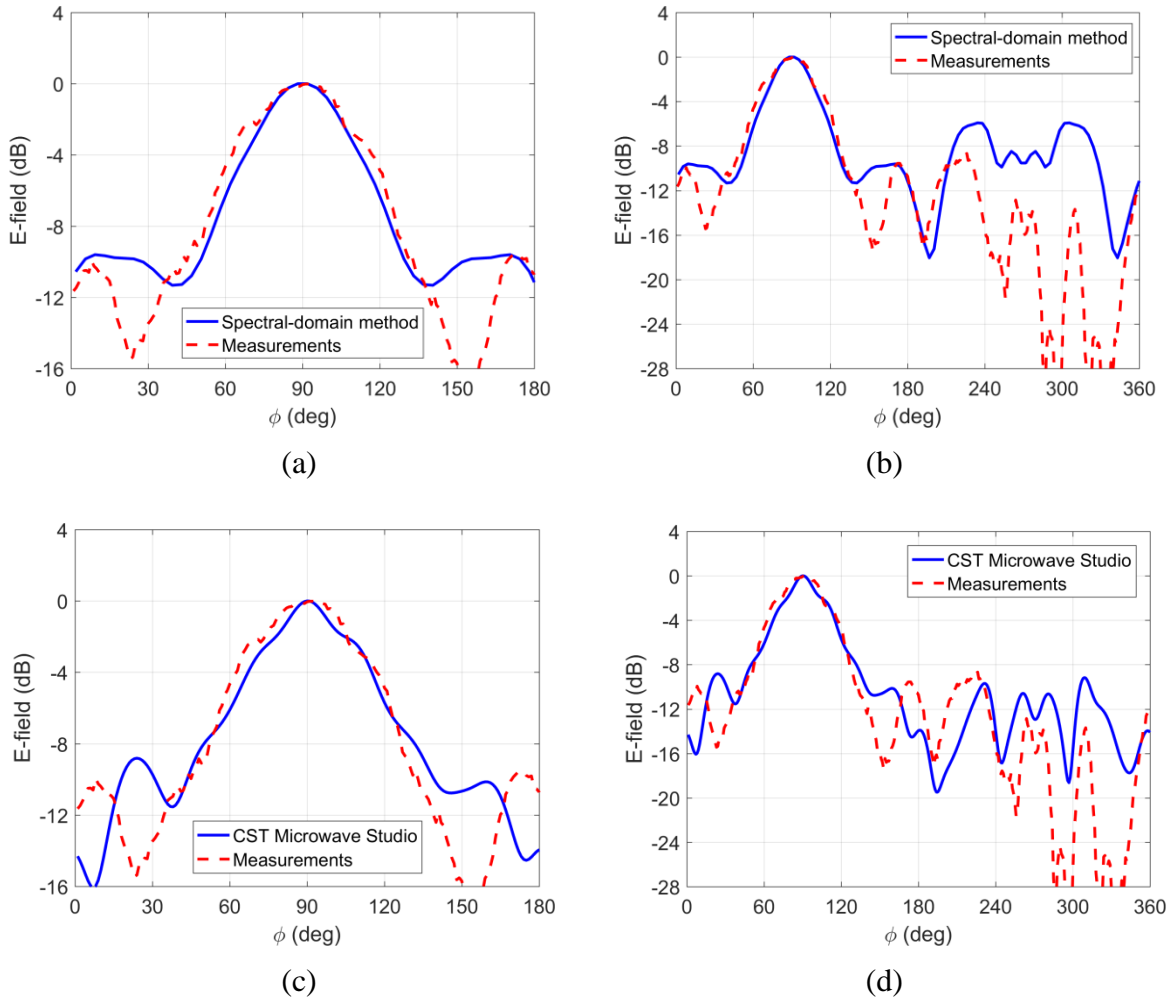


Fig. 6.19. Radiation patterns for the designed two-layer metasurface with waveguide feed; (a) comparison of measured results and developed SD method for forward direction, (b) comparison of measured results and developed SD method for the entire angular range, (c) comparison of measured results and CST MS results for forward direction, (d) comparison of measured results and CST MS results for the entire angular range.

The developed SD method shows results which accurately predict the main lobe, but fail in the backward direction as seen in Fig. 6.19.ab. CST MS results (Fig. 6.19.cd) give a better prediction in this case. This comparison indicates to a potential problem with measurement setup since there is no symmetry in the backward radiation direction.

The analysis of the frequency dependence in Fig. 6.20. reveals that the measurement pattern is stable in the forward direction, but the backward direction changes significantly with frequency. This is not the case in the numerically obtained results which show much smaller variations which again indicates a certain alignment problem which in spite several attempts was not successfully resolved in this measurement campaign.

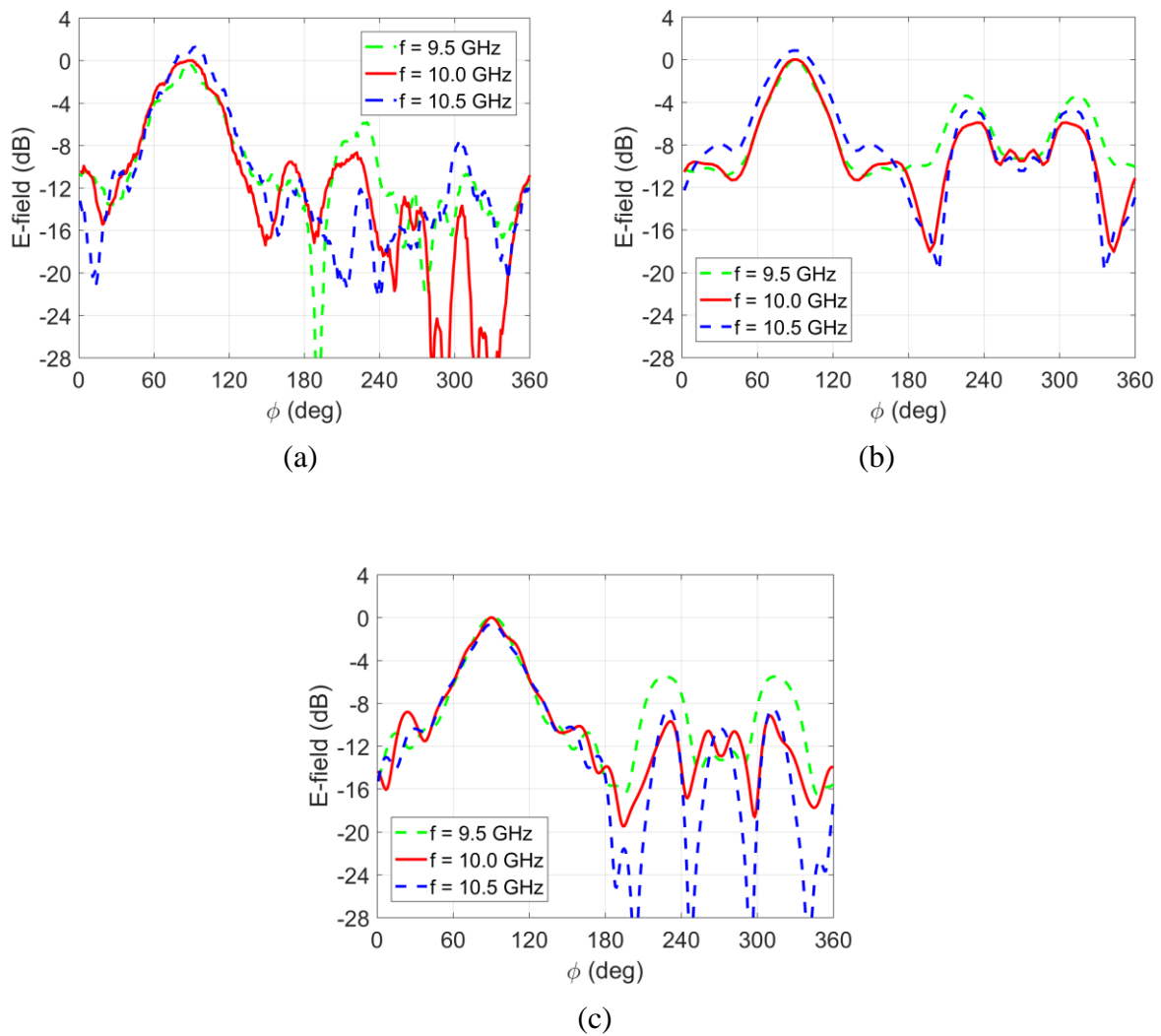


Fig. 6.20. Frequency dependence of radiation pattern; (a) measurements, (b) spectral domain approach, (c) CST Microwave Studio.

6.2.2. Rectangular horn feed - curved two-layer metasurface

Influence of the metasurface layer is investigated also using a rectangular horn feed antenna. The antenna and its radiation pattern are shown in Figs. 6.21 and 6.22, and as before the metasurface should enhance the gain of this horn antenna and at the same time have reduced backscattering compared to a single layer metasurface case.



Fig. 6.21. Rectangular horn feed antenna.

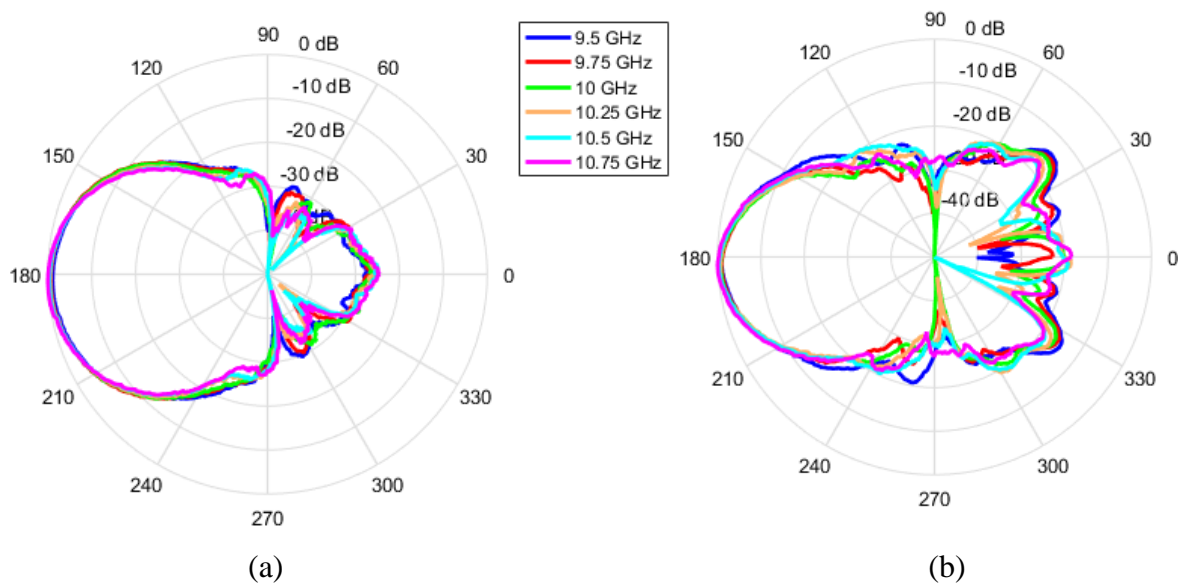


Fig. 6.22. Measured radiation patterns for; (a) rectangular horn feed antenna, (b) rectangular horn feed antenna with two-layer metasurface.

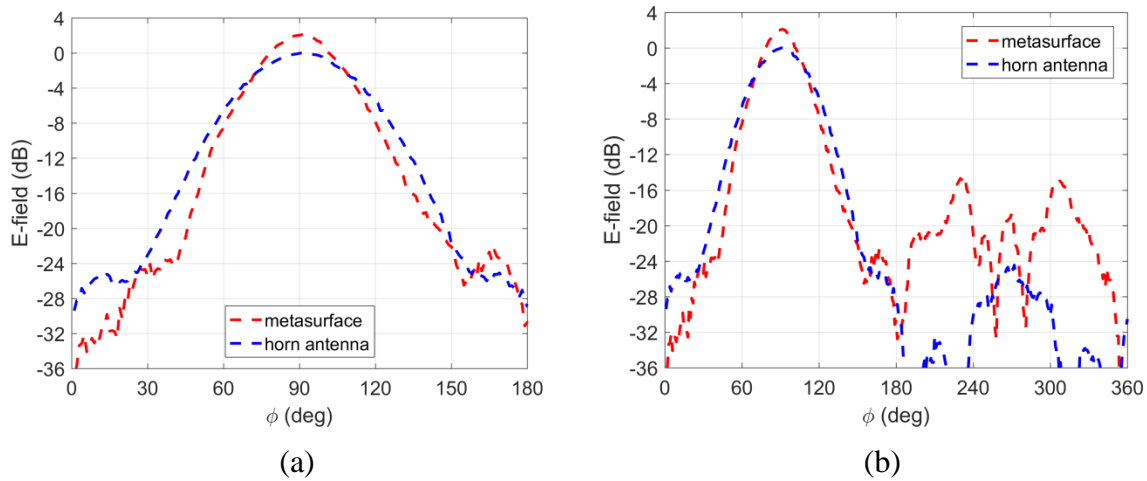
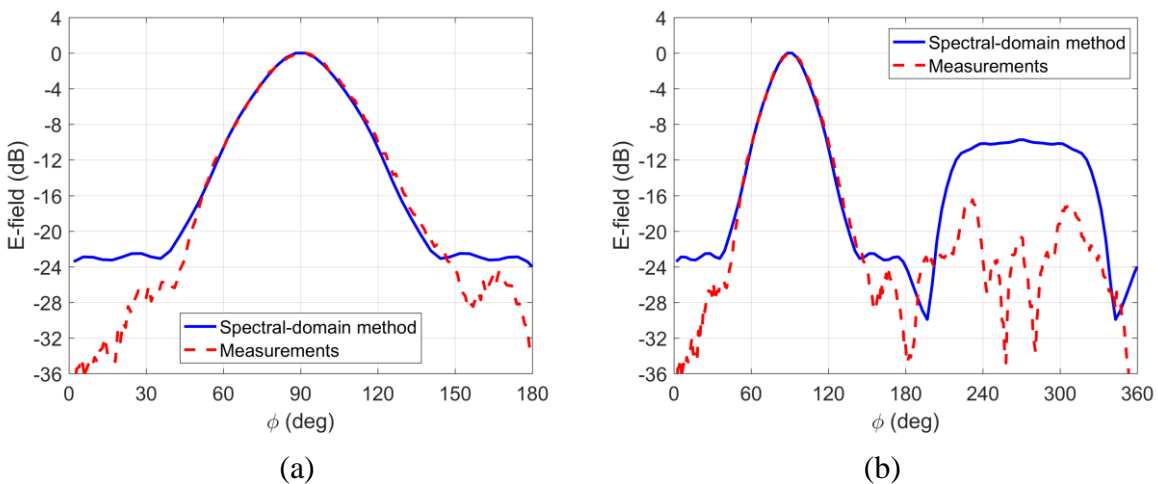


Fig. 6.23. Comparison between measured radiation patterns at 10 GHz for horn antenna without and with the two-layer metasurface; (a) only forward direction, (b) full angular pattern.

As expected, the results in Figs. 6.22. and 6.23. show the gain improvement achieved using the metasurface layer (note that the patterns are normalized with the gain of rectangular horn feed antenna).

The developed SD method again shows results (Fig. 6.24.ab) which accurately predict the main lobe, but the level of the field in the backward direction has a considerable error. CST MS results (Fig. 6.24.cd) are better in this case, and quite accurately predict the backward radiation.

Frequency results in Fig. 6.25 show much more stable results for the measured case with respect to the waveguide opening. This confirms a possible problem with the alignment of the waveguide feed in the previous case. Still however, the spectral domain method results show too high field level in the backward direction, whereas CST MS gives reasonable prediction for all frequencies.



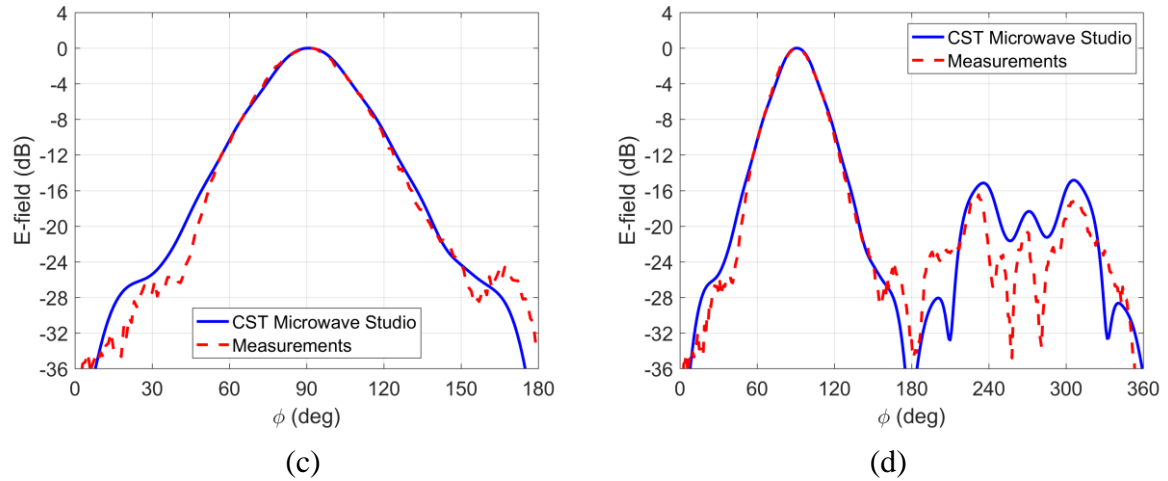


Fig. 6.24. Radiation patterns for the designed two-layer metasurface with waveguide feed; (a) comparison of measured results and developed SD method for forward direction, (b) comparison of measured results and developed SD method for the entire angular range, (c) comparison of measured results and CST MS results for forward direction, (d) comparison of measured results and CST MS results for the entire angular range.

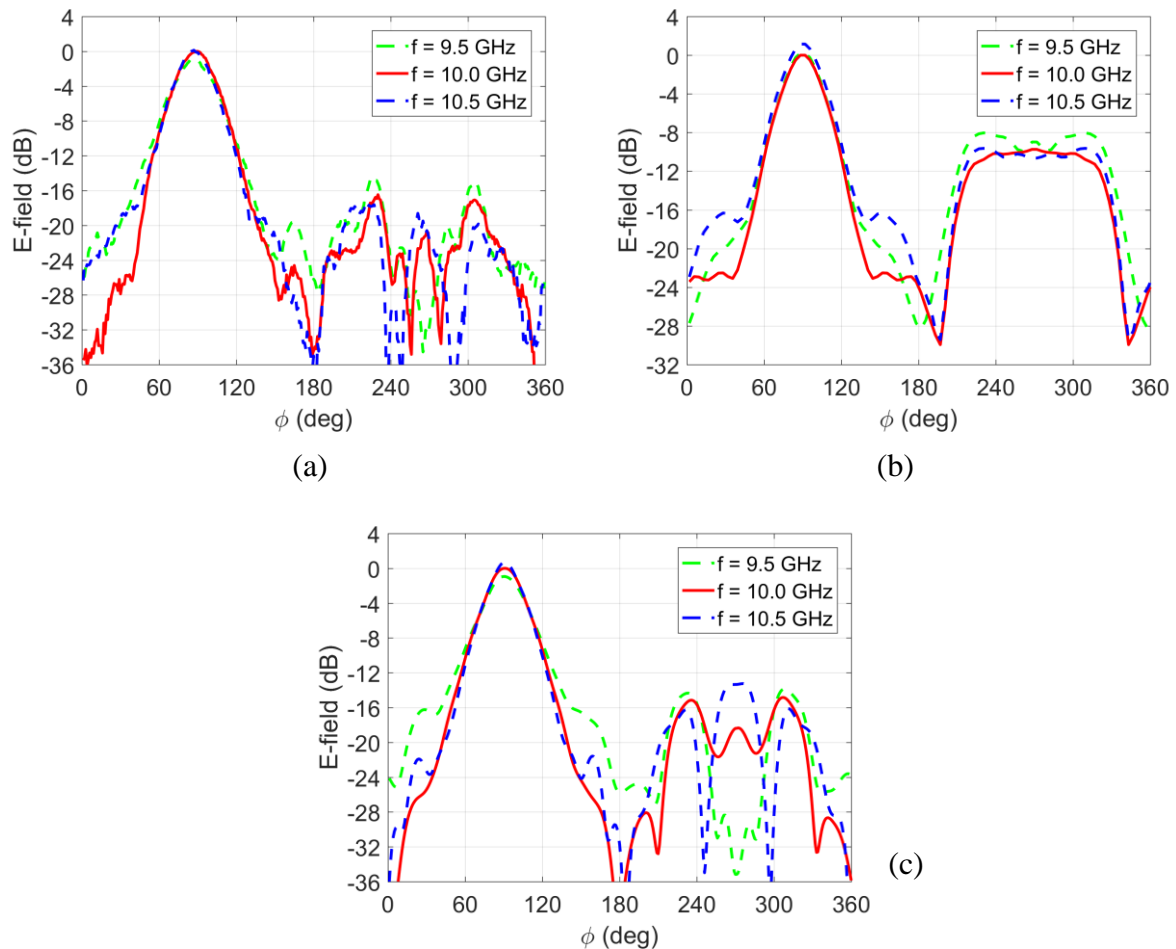


Fig. 6.25. Frequency dependence of radiation pattern; (a) measurements, (b) spectral domain approach, (c) CST Microwave Studio.

6.3 Production of curved metasurfaces structures

In principal, there are two problems with design and implementation of curved metasurfaces (in comparison to planar structures): analysis methods are more complicated and the production techniques are much more complex.

The production of single-curved structures (i.e. structures with one principal direction of curvature) is of the same order of complexity like production of planar counterparts - it is still possible to use standard printed circuit board (PCB) technology. However, there are several practical details to be considered. In the process of bending a planar substrate, the length of outer surface is larger than the length of inner surface. Therefore, the dimensions of the metasurface elements will be enlarged at the outer surface. This extension of the dimensions should be taken into account when designing the metasurface elements. Next, when designing structures with more than two metasurface layers, it is important to adhesively bond layers together without introducing airpockets, gaps and cracks between the layers. Therefore, in this process it is helpful and important to have a rigid frame (i.e. mold) to successfully bend and glue layers that form a multilayer structure. Finally, it is important to choose a substrate suitable for bending, i.e. to select a microwave substrate with a low value of flexural modulus. In mechanics, the flexural modulus or bending modulus is an intensive property that is computed as the ratio of stress to strain in flexural deformation, or the tendency for a material to resist bending. Ideally, flexural or bending modulus of elasticity is equivalent to the tensile modulus (Young's modulus). Another parameter of interest is the tensile strength of a material defined as the maximum amount of tensile stress that the material can take before failure, for example breaking. In the Table the values of flexural modulus and tensile strength are given for a "classical" FR4 substrate and for two substrates suitable for building conformal antennas and metasurfaces.

TABLE 6.3 MECHANICAL PROPERTIES OF DIFFERENT MICROWAVE SUBSTRATES

Name	Producer	Permittivity (at 10.0 GHz)	Flexural modulus	Tensile strength
FR4	Isola	3.65	3190 kpsi (22.0 GPa)	46.4 kpsi (320 MPa)
IsoClad 933	Rogers corporation	2.33	239 kpsi (1.65 GPa)	5.3 kpsi (36.6 Mpa)
FLX1100	Premix	11.0	275 kpsi (1.9 GPa)	2.03 kpsi (14.0 Mpa)

Double-curved metasurface structures are much harder to produce. It is not possible just to bend the substrate material since now we have two principal orthogonal directions of curvature. One possibility is to produce the dielectric supporting structure using 3D printing technology. In the last decade we faced a strong development of this production technology with a variety of applications. The accuracy of production facilities depends on the quality of the 3D printer, and the tolerances of the printed prototype can be less than 0.02 mm, which fulfils requirements for most of metasurface applications. Note that nowadays it is possible to buy "electromagnetic" filaments for 3D printing with a large range of permittivity and low

losses at microwave frequencies. For example, the Preperm company offers filaments for 3D printing with permittivity tailored between 3 and 10, and with typical dissipation factor 0.004.

While it is relatively simple to produce the dielectric supporting structure, the metallization process is much more complex. We have investigated several possibilities of performing metallization: using sprays with conductive paint, using electroless copper plating process or using sputtering technology. The first possibility is the simplest one – one needs just to make a mold or pattern for spraying and to spray the dielectric supporting structure with conductive paint. However, there are two serious drawbacks: the pattern should tightly fit to the dielectric structure (otherwise, the effect of widening the metal areas, patches and lines, will occur), which is not so easy to obtain for double-curved structures. The other drawback is more serious – such paints have limited conductivity and therefore the losses in metasurface structure are increased. Table 6.4 gives a comparison of conductivity of three commercial products. It can be seen that two of them have several orders of magnitude worse conductivity comparing to the copper made structures (the conductivity of copper at room temperature is 5.96×10^7 S/m).

TABLE 6.4 CONDUCTIVITY PROPERTIES OF DIFFERENT METALIZED PAINTS

Name of the product	Producer	Surface Resistivity	Estimated conductivity
Silver Plated Copper Compound RS 247-4251	RS PRO	0.3 - 0.7 Ω /sq. @ 50 microns	$2.9 \cdot 10^4$ - $6.7 \cdot 10^4$ S/m
NSCP Nickel Screening Compound – Plus	Electrolube	0.3 - 0.7 Ω /sq. @ 50 microns	$2.9 \cdot 10^4$ - $6.7 \cdot 10^4$ S/m
Conductive silver coating 3830	Hollandshielding	< 0.015 Ω /sq. @ 25 microns	> $2.7 \cdot 10^6$ S/m

In order to test the production process based on spraying the metalized paint we have repeated production of the single-layer metasurface described in section 6.1, but this time using this production technology. First we have produced the pattern for spraying. The pattern itself was made from a solid thin cardboard, and for precise cutting we have used laser CNC machine. Two prototypes of the pattern for spraying are shown in Fig. 6.26. It can be seen that the first prototype had problems with internal forces which laterally “moved” the walls between holes for meander line, but in the second prototype we have managed to solve this problem.

In the next step of production we sprayed the metasurface structure. As a spray we used the Tifoo conductive silver varnishing spray (with unfortunately no data about surface resistance), and as a supporting structure we used paper with weight (thickness) 200 g/m². It can be seen from Fig. 6.27 that we did not manage to keep the width of the meander lines as it was cut in the pattern, i.e. the realized lines were wider than desired. We believe that we will soon solve this problem by selecting the proper materials for the mold pattern and for the supporting structure.

The comparison of measured results of two metasurface structures (produced with the PCB technology and with spraying the conductive paint, respectively) is given in Fig. 6.28. It can be seen that the low-conductivity of the paint introduced additional losses, i.e. the realized gain pattern is 1.9 dB lower when the conductive paint is used for metasurface production. Furthermore, the undesired change in the width of the meander lines causes additional perturbations in the radiation pattern (with larger back-side radiation comparing to the original design). We believe that more accurate production procedure and using better conductive paint (e.g. Conductive silver coating 3830) will drastically improve the quality of metasurface structures produced using this simple technology.

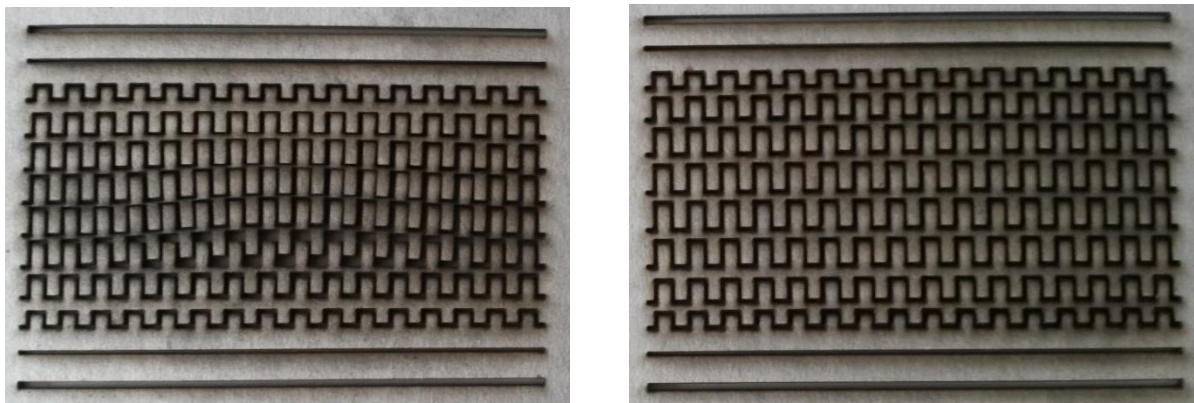


Fig. 6.26. Prototypes of the mold pattern with and without lateral shift of the internal walls.

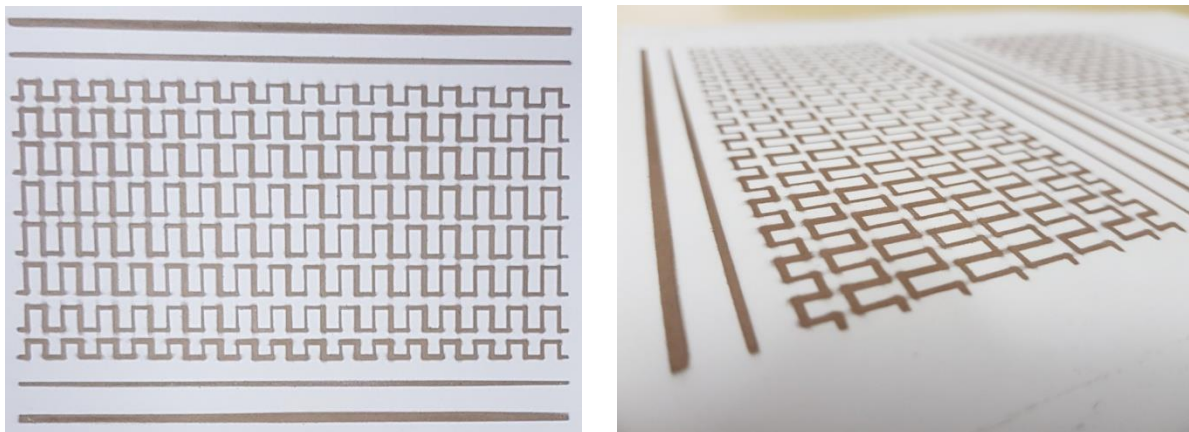


Fig. 6.27. Prototype of the metasurface structure produced by conductive coating technology.

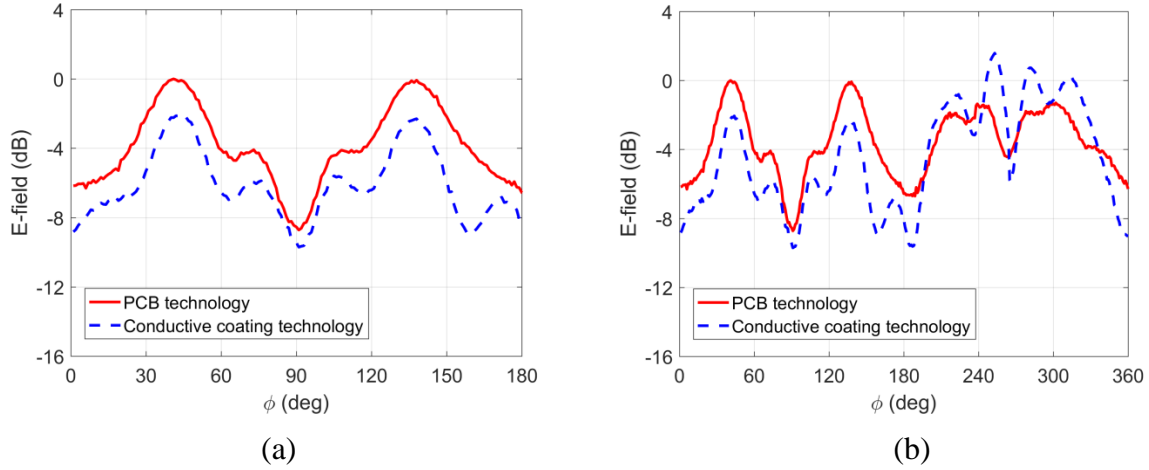


Fig. 6.28. The comparison of measured results of two metasurface structures produced by PCB technology and by spraying the conductive paint; (a) front radiation pattern, (b) full radiation pattern.

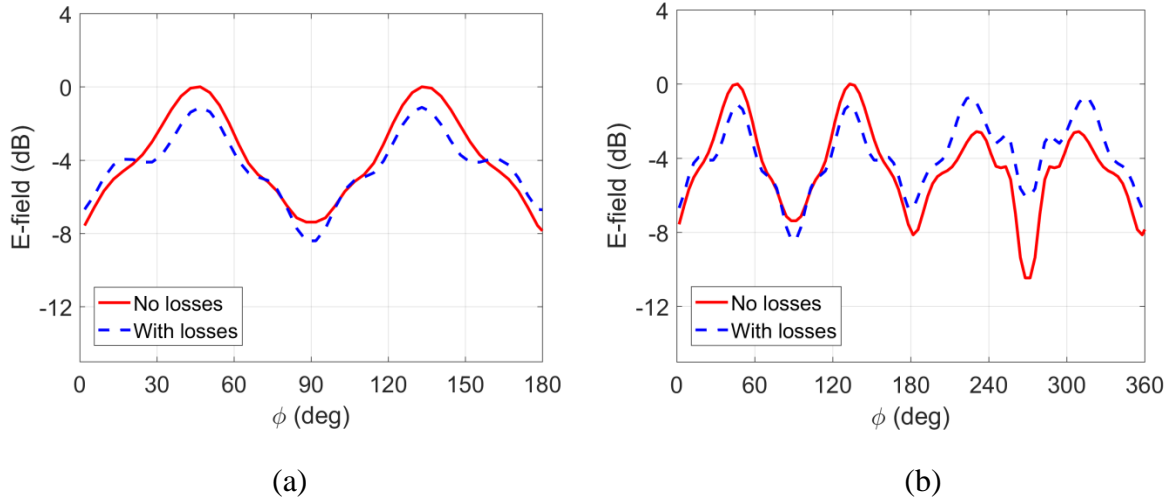


Fig. 6.29. The comparison of calculated results of two metasurface structures produced by PCB technology and by spraying the conductive paint; (a) front radiation pattern, (b) full radiation pattern. The assumed surface sheet impedance is given in Table 6.5

We tried to estimate the losses in the strips and meander lines of the prototype produced using conductive paint. In order to do that we started with an approximate formula for surface impedance of periodic strip lines with included losses [49], i.e. with generalization of eq. (3.16.a):

$$Z_{zz}^{approx}(k_z) = R_\sigma P_\phi + j \frac{k_0 \eta_0}{2\pi} P_\phi \log \left(\csc \left(\frac{\pi W}{2P_\phi} \right) \right) \left(1 - \frac{k_z^2}{k_{eff}^2} \right) \quad (5.1)$$

Here R_σ is the term that represents the losses due to finite conductivity – it is a ratio of voltage and line current per unit length. We have estimated that term by measuring the DC resistance,

and the results are given in table 6.5. The comparison of calculated radiation pattern for omnidirectional excitation using the developed spectral-domain approach is given in Fig. 6.29. By comparing the Figures 6.28 and 6.29 we can conclude that we have found a reasonable estimation of the surface impedance. The obtained values of surface resistance are quite large, which once more emphasize the need of using conductive paint of better quality (e.g. Conductive silver coating 3830).

TABLE 6.5 ESTIMATED SURFACE SHEET IMPEDANCE OF A METASURFACE REALIZED WITH PCB AND CONDUCTIVE PAINT TECHNOLOGY

Segment No.	Width of the stripline and meanderline	Total width of the meander line	Estimated surface sheet impedance of a metasurface realized with PCB technology	Estimated surface sheet impedance of a metasurface realized with conductive paint technology
1	w = 1.3 mm	-	$j \cdot 126.16 \Omega$	$10 + j \cdot 126.16 \Omega$
2	w = 0.5 mm	-	$j \cdot 223.66 \Omega$	$360 + j \cdot 223.66 \Omega$
3	w = 0.5 mm	h = 3.5 mm	$j \cdot 392.53 \Omega$	$683 + j \cdot 392.53 \Omega$
4	w = 0.5 mm	h = 5.15 mm	$j \cdot 587.52 \Omega$	$828 + j \cdot 587.52 \Omega$
5	w = 0.5 mm	h = 6.1 mm	$j \cdot 756.39 \Omega$	$918 + j \cdot 756.39 \Omega$
6	w = 0.5 mm	h = 6.5 mm	$j \cdot 853.89 \Omega$	$954 + j \cdot 853.89 \Omega$

We have also considered other technologies for performing metallization. Probably the best one is using sputtering technology [50]. Sputter deposition is a widely used technique to deposit thin films on substrates. The technique is based upon ion bombardment of a source material, the target. Ion bombardment results in a vapor due to a purely physical process, i.e. the sputtering of the target material. Then the target material is deposited on the object of interest (in our case on a dielectric substrate). Many scientific institutes have the sputtering systems, so they can be used for testing this promising metallization technology for the production of metasurface structures. Unfortunately, although one such facility exists in Zagreb, we were not able to arrange the production of such prototypes due to their time schedule (we hope to arrange it in near future).

The last metallization technology we have investigated is electroless copper plating process. Here the object that we would like to metalize (produced using 3D printing technology) is put into a digester, and the metallization process can be divided into the following stages: (i) rinsing and degreasing of 3D printed parts, (ii) preconditioning of 3D printed parts in a solution of sulphuric acid (H_2SO_4) and hydrogen-peroxide (H_2O_2) to create pores in the plastic for better adhesion of copper, (iii) sensitizing the surface by immersion into a solution of hydrogen chloride (HCl) and tin(II) chloride ($SnCl_2$), (iv) applying a catalyst by immersing the parts into a solution of hydrogen chloride and palladium chloride ($PdCl_2$) which allows the tin ions to bond with palladium ions (palladium is the catalyst for copper deposition), (v) removal of extra tin ions by immersion into a solution of hydrogen chloride (HCl) which melts the tin ions and removes them from the surface of the plastic parts, (vi)

deposition of copper through immersion in a solution of copper sulphate or copper chloride stabilised with ethylenediaminetetraacetic acid where formaldehyde is used for reductive coupling. Parts of this process are shown in the photographs in Fig. 6.30. This process is known as electroless bath process and is described in [51]. It results in a typical film thickness of 2-3 μm which is sufficient for our applications, but the components must be handled with care since the copper layer is easily scratched or damaged until a protective layer is applied. Till now we have successfully metalized objects (antennas) that originally are made from metal; the shape of produced antennas was determined using 3D printing technology and then they were fully metalized using the described technology. Now we are working on combining the production of the dielectric objects in 3D printing technology and the partial metallization (for that a mold pattern should be firmly attached to the 3D printed object).



Fig. 6.30. *Various stages of the electroless copper plating process.*

Conclusions

Metasurfaces that manipulate electromagnetic waves have garnered significant attention in recent years. The focus has primarily been on planar devices, while many applications require curved surfaces. The purpose of this project is to develop an analysis approach and specialized programs that are able to efficiently and accurately design curved multilayer metasurface structures. The proposed approach combines the concept of sheet impedance with a new transmission matrix formulation that is applicable to stratified, canonical curved geometries. The results are verified both numerically and experimentally through a lot of metasurface examples of cylindrical and spherical shape, as well as through structures with body of revolution type of symmetry.

The report discusses a method for determining the value of surface sheet impedance by considering the metasurface response on impinging electromagnetic wave with different phase variation along the curved surface, i.e. by response on different spectral-domain components of incoming wave. Furthermore, the reported approach extends the ABCD matrix formulation for the analysis of circuit networks or planar stratified electromagnetic structures to canonical curved geometries. The ABCD matrix formulation captures the interaction between sheets of the metasurface, while the individual sheets are modelled with surface impedance $\bar{\bar{Z}}$ calculated in the spectral domain. The surface impedances can be determined either using a rigorous electromagnetic solver, such as the Method of Moments, or using approximate analytical expressions. These approximate expressions often assume that the surface impedance is constant with respect to spectral-domain angular variation of the incidence field. This leads to inaccuracies when $\bar{\bar{Z}}$ changes rapidly with respect to the spectral variable, i.e. if the considered metasurface has strong spatial dispersion. To account for this, the analytical formulas for the surface impedance of some planar metallic patterns have been modified to account for the considered angular Fourier harmonic. It has been shown, through calculations and comparison with measurements, that such canonical metasurfaces can be accurately modelled with the proposed approach. The approach can also aid in selecting the type of patterned sheet needed to obtain the desired variation in surface impedance $\bar{\bar{Z}}$ with modal number m .

The considered analysis approach is extended to curved metasurfaces that are not homogeneous, i.e. to metasurfaces that have spatially-varying distribution of surface sheet impedance. The extended formulation also covers metasurfaces that are located only on a part of canonical curved surface (for the rest of the canonical surface we simply define that the

value of surface admittance is equal to zero). Four different formulations of the extended analysis approach are discussed, and the selection of most suitable one depends on the domain (spectral or spatial) in which we would like to calculate the surface impedance distribution and on the type of Green's functions that will take into account the presence of the multilayer curved structure.

The considered analysis approach is also extended to the structures with body-of-revolution type of symmetry. This type of structures belongs to the class of two-dimensional structures, i.e. they are homogeneous only in one (circumferential) direction. Consequently, for each spectral component of the excitation we need to solve a two dimensional electromagnetic problem, and for that purpose we have developed an efficient Moment Method program.

Finally, the problem of production of curved metasurfaces structures is discussed in the report. Single-curved structures (i.e. structures with one principal direction of curvature) can be quite easily produced using standard printed circuit board (PCB) technology; one just needs to select a proper substrate suitable for bending (i.e. a substrate with low value of the flexural modulus). However, double-curved structures are much harder to produce. One possibility is to produce the dielectric part using 3D printing technology and then somehow metalize the desired patterns on it. The metallization represents the largest problem in production, and it can be made using sprays with conductive paint (consequently, with larger losses comparing to the PCB technology), using electroless copper plating process or using sputtering technology. In all mentioned cases there are still many technology issues to be solved, in particular, the problem of firm contact of the mold pattern and the metasurface structure without cracks and gaps and these are the topics for future investigations.

Appendix

A.1 Approximate expressions for sheet impedance of metasurfaces with canonical patterns

In this Appendix we will list all the approximate expressions that we have used for initial design of metasurfaces created with metallic objects of regular geometric shape. Note that the final dimensions of metallic pattern were always determined with general solver (either based on the moment method (MoM) [26] or on Finite Integral Technique (FIT) [37]). However, these formulas are useful in order to get the feeling which elements (shapes) to use in some particular design, and which range of surface sheet impedance values can be achieved with the considered elements. Furthermore, the listed formulas have different level of accuracy; the most accurate formulas are for the simplest geometrical shapes – strips and patches.

The approximate expressions used for different designs are:

(a) Strips: E-field is along the strips (see Fig. A.1.a and references [27] and [49])

$$Z_{strips}^{TM,\parallel}(k_z) = j \frac{k_0 \eta_0}{2\pi} P \log \left(\csc \left(\frac{\pi W}{2P} \right) \right) \left(1 - \frac{k_z^2}{k_{eff}^2} \right) \quad (A.1.a)$$

$$Z_{strips}^{TE,\parallel}(k_z) = j \frac{k_0 \eta_0}{2\pi} P \log \left(\csc \left(\frac{\pi W}{2P} \right) \right) \quad (A.1.b)$$

$$k_{eff}^2 = k_0^2 \cdot (\epsilon_r + 1)/2, \quad k_z = k_0 \sin \theta. \quad (A.1.c)$$

(b) Strips: E-field is perpendicular to the strips (see Fig. A.1.a and ref. [27])

$$Z_{strips}^{TE,\perp}(k_z) = -j \frac{\pi \eta_0}{P k_0 (1 + \epsilon_r)} \left[\log \left(\csc \left(\frac{\pi W}{2P} \right) \right) \left(1 - \frac{k_z^2}{k_{eff}^2} \right) \right]^{-1} \quad (A.2.a)$$

$$Z_{strips}^{TM,\perp}(k_z) = -j \frac{\pi \eta_0}{P k_0 (1 + \epsilon_r)} \left[\log \left(\csc \left(\frac{\pi W}{2P} \right) \right) \right]^{-1} \quad (A.2.b)$$

(c) Two-dimensional strip grid (see Fig. A.1.b and references [27] and [49])

$$Z_{grid}^{TM}(k_z) = j \frac{k_0 \eta_0}{2\pi} P \log \left(\csc \left(\frac{\pi W}{2P} \right) \right) \left(1 - \frac{k_z^2}{2k_{eff}^2} \right) \quad (\text{A.3.a})$$

$$Z_{grid}^{TE}(k_z) = j \frac{k_0 \eta_0}{2\pi} P \log \left(\csc \left(\frac{\pi W}{2P} \right) \right) \quad (\text{A.3.b})$$

(d) Patches (see Fig. A.1.b and ref. [27])

$$Z_{patch}^{TE} = \frac{\eta_0^2}{2(\epsilon_r + 1) Z_{grid}^{TM}} \quad (\text{A.4.a})$$

$$Z_{patch}^{TM} = \frac{\eta_0^2}{2(\epsilon_r + 1) Z_{grid}^{TE}} \quad (\text{A.4.b})$$

(e) Meander lines (see Fig. A.1.d and ref. [52])

Approximate formula for parallel polarization (approximate formula for the perpendicular polarization can be found in [52]):

$$Z_{\parallel} = \frac{j\eta_0 P_{\parallel}}{2\lambda_0 \left[1 - \left(\frac{fh}{5.62} \right)^2 \right]} \left\{ K_4 \left[-\frac{P_{\perp}}{P_{\parallel}} \ln \left(\frac{\pi w}{2P_{\perp}} \right) \right] + K_5 \left[\frac{2h}{P_{\parallel}} \ln \left(\frac{4P_{\parallel}}{\pi w} \right) - 0.492 \right] \right\} \quad (\text{A5})$$

$K_4 = 5.3242, \quad K_5 = 1.7424.$

(f) Rectangular loops (see Fig. A.1.e and ref. [53])

$$Z_{loop} = j\eta_0 \cdot \left[\frac{d}{P} F(P, 2w, \lambda_0, \theta) - 4 \frac{d}{P} F(P, g, \lambda_0, \theta) \right] \quad (\text{A.6.a})$$

$$F(P, s, \lambda_0, \theta) = \frac{P}{\lambda_0} \cos \theta \left[\ln \left(\operatorname{cosec} \left(\frac{\pi s}{2P} \right) \right) + G(P, s, \lambda_0, \theta) \right] \quad (\text{A.6.b})$$

$$G(P, s, \lambda_0, \theta) = \frac{1}{2} \frac{(1 - \beta^2)^2 \left[\left(1 - \frac{\beta^2}{4} \right) (A_+ + A_-) + 4\beta^2 A_+ A_- \right]}{\left(1 - \frac{\beta^2}{4} \right) + \beta^2 \left(1 + \frac{\beta^2}{2} - \frac{\beta^4}{8} \right) (A_+ + A_-) + 2\beta^6 A_+ A_-} \quad (\text{A.6.c})$$

$$A^{\pm} = \frac{1}{\sqrt{\left[1 \pm \frac{2P \sin \theta}{\lambda_0} - \left(\frac{P \cos \theta}{\lambda_0}\right)^2\right]}} - 1, \quad \beta = \sin\left(\frac{\pi s}{2P}\right) \quad (\text{A.6.d})$$

(f) Jerusalem crosses (see Fig. A.1.f and references [54] and [55])

$$Z_{JC} = j\eta_0 \cdot \left[\frac{P-g}{P} F(P, w, \lambda_0, \theta) - 4 \frac{T}{P} F(P, g, \lambda_0, \theta) - 4 \frac{(2w+T)}{P} F(P, P-T, \lambda_0, \theta) \right] \quad (\text{A.7})$$

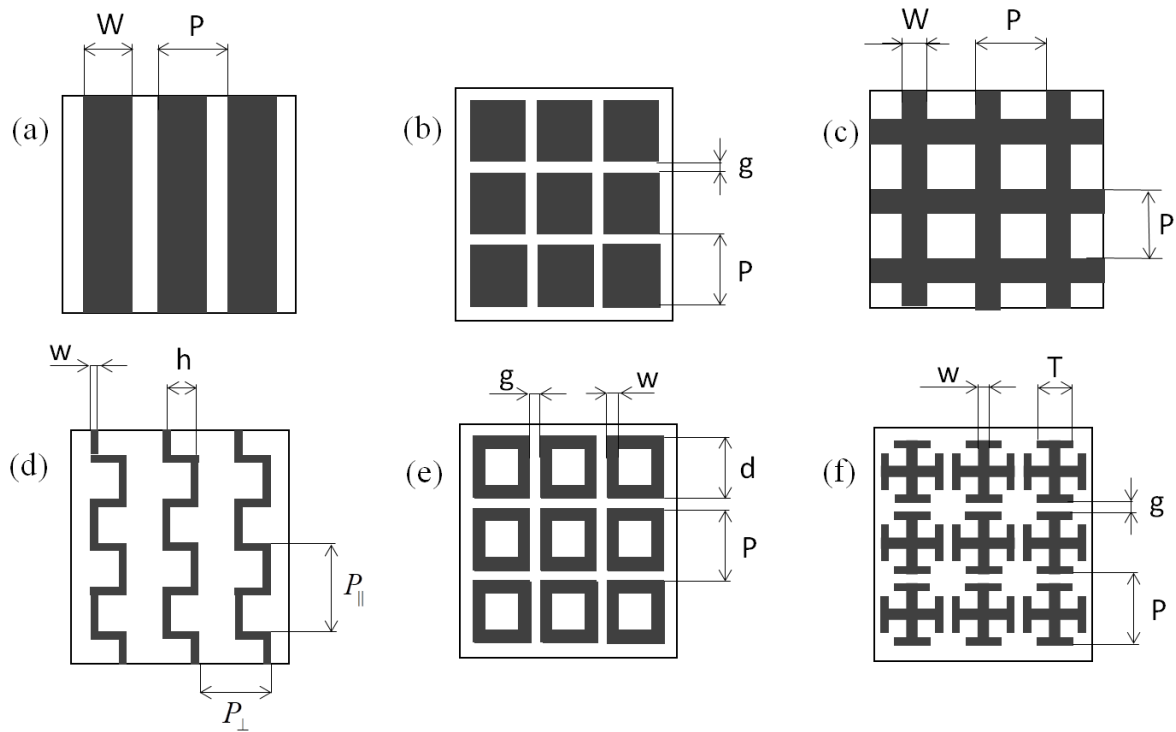


Fig. A.1. Regular geometrical shapes for which approximate expressions for surface sheet impedance are available.

Typical values that can be obtained using different metallic objects with regular geometric shape are given in Fig. A.2.

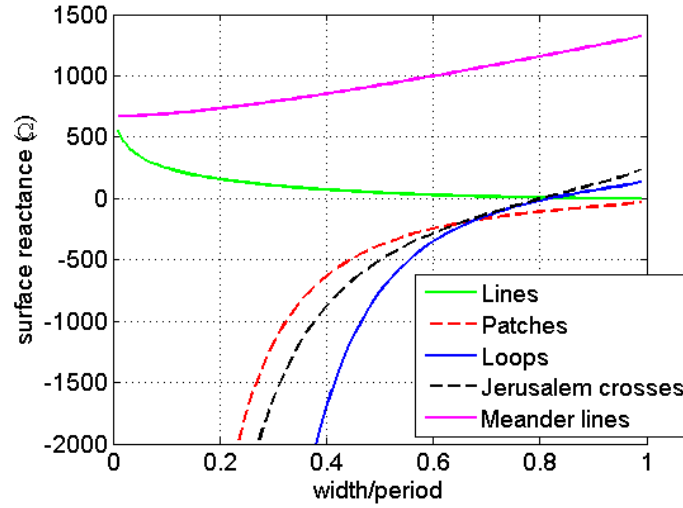


Fig. A.2. Typical values of surface sheet impedance that can be obtained using different metallic objects with regular geometric shape.

A.2 Moment method program for analyzing circular-cylindrical periodic structures

The formulation of the moment method (MoM) program for analyzing circular-cylindrical periodic structures is derived from the formulation for analyzing circular-cylindrical periodic structures and is described in details in [26]. Planar periodic metal pattern (represented by patches or strips) can be accurately analyzed by expanding the unknown currents on metal patterns in basis functions, and by using MoM to numerically determine the amplitudes of the basis functions. We formulate an integral equation by stating that the tangential electric field is zero at the metal surface, i.e. $\hat{n} \times [\mathbf{E}^{inc} + \mathbf{E}^{scat}] = 0$. Since the structure is periodic the electromagnetic field excited by the currents is in the form of the Floquet modes, and the currents on different metal patterns are identical except for a linear phase difference equal to the considered harmonic variation of the incident field.

The problem is solved in the spectral domain. In the planar case, we use a two-dimensional Fourier transformation in the directions in which the structure is periodic (i.e. x- and y-directions) and in the cylindrical case we use a Fourier transformation in a axial z direction and a Fourier series in a circumferential ϕ direction. The scattered field \mathbf{E}^{scat} can be expressed in terms of the spectral domain dyadic Green's function $\tilde{\mathbf{G}}$ and the Fourier transform of the current on one metal pattern, according to

$$\mathbf{E}^{scat}(u_n, u_o, u_l) = \frac{1}{P_o P_p} \sum_{m=-\infty}^{\infty} \sum_{l=-\infty}^{\infty} \tilde{\mathbf{G}}(u_n, k_o^m, k_p^l | u'_n) \cdot \tilde{\mathbf{J}}(k_o^m, k_p^l) e^{-jk_o^m u_o} e^{-jk_p^l u_p} \quad (\text{A.8})$$

$$k_o^m = \frac{2m\pi}{P_o} + k_o^{inc}, \quad k_p^l = \frac{2l\pi}{P_p} + k_p^{inc} \quad (\text{A.9})$$

where k_o^{inc} and k_p^{inc} are the propagation constants of the incident wave in two orthogonal directions across the metal pattern (i.e. o and p directions), P_o and P_p are the periodicity of the unit cell in o and p directions, and $'$ denotes the source coordinates. The spectral domain Green's function $\tilde{\mathbf{G}}$ is calculated for example by the G1DMULT routine. The integral equation is transformed into a matrix equation by using the MoM where the test functions are the same as the basis functions (Galerkin's method), and the inner product is taken across the central unit cell. The expression for the elements of the MoM matrix is derived from eq. (A.8), and the expression for the elements of the voltage vector is obtained by integrating the product of the test function and the incident field component parallel to the test function. The elements of the impedance matrix and the excitation vector are:

$$Z_{ij} = \frac{1}{P_o P_p} \sum_{m=-\infty}^{\infty} \sum_{l=-\infty}^{\infty} \tilde{\mathbf{J}}(-k_o^m, -k_p^l) \cdot \tilde{\mathbf{G}}(u_n, k_o^m, k_p^l | u'_n) \cdot \tilde{\mathbf{J}}(k_o^m, k_p^l) \quad (\text{A.10})$$

$$V_i = \tilde{\mathbf{J}}(-k_o^{inc}, -k_p^{inc}) \cdot \mathbf{E}(u'_n, u'_o = 0, u'_p = 0) \quad (\text{A.11})$$

where conveniently we choose that the u'_o and u'_p coordinates of the center of the metal pattern are zero. In the planar case, the quantities in eqs. (A.8) - (A.11) are:

$$u_n = z, \quad u_o = x, \quad u_p = y \quad (\text{A.12})$$

In the cylindrical case, the incident plane wave is expanded as

$$E_z^{inc} = E_0 \sin \theta^{inc} \cos \alpha^{inc} \cdot \sum_{n=-\infty}^{\infty} j^n J_n(k_0 \rho \sin \theta^{inc}) e^{-jn(\phi - \phi^{inc})} e^{jz k_0 \cos \theta^{inc}} \quad (\text{A.13})$$

where J_n is the n th-order Bessel function of the first kind, the polarization angle α^{inc} is the angle the incident electric field makes with the plane of incidence, and θ^{inc} and ϕ^{inc} are angles of incidence measured, respectively, from the z -axis and x -axis in the xy plane. The scatterer has the following symmetry: by rotating the scatterer by $2\pi/N_\phi$ where N_ϕ is the number of unit cells in ϕ direction, we get the same structure. Thus we expand the fields in Floquet modes in ϕ direction where for every component of the incident field in eq. (A.13) the strips excite fields which have the same phase variation between the centers of the strips as the incident cylindrical wave. In this case the scattered field due to the incident wave with $\exp(-jn\phi)$ variation is also given by eq. (A.8) with

$$u_n = \rho, \quad u_o = \phi, \quad u_p = z \quad (\text{A.14})$$

and

$$k_o^{inc} = n, \quad k_p^{inc} = -k_z^{inc} = -k_0 \cos \theta^{inc}. \quad (\text{A.15})$$

Bibliography

- [1] A. B. Munk, *Frequency Selective Surfaces: Theory and Design*, John Wiley & Sons, 2005.
- [2] C. L. Holloway, E. Kuester, J. Gordon, J. O'Hara, J. Booth, and D. Smith, "An overview of the theory and applications of metasurfaces: The twodimensional equivalents of metamaterials," *IEEE Antennas Propag. Mag.*, Vol. 54, no. 2, pp. 10–35, April 2012.
- [3] A. M. Patel and A. Grbic, "Millimeter-Wave Transmitarrays for Wavefront and Polarization Control," *IEEE Trans. Microw. Theory Techn.*, Vol. 61, pp. 4407-4417, Dec. 2013.
- [4] C. Pfeiffer and A. Grbic, "Bianisotropic metasurfaces for optimal polarization control: Analysis and synthesis," *Physical Review Applied*, Vol. 2, Art. ID 044011, October 2014.
- [5] C. Pfeiffer and A. Grbic, "Metamaterial Huygens' surfaces: Tailoring wave fronts with reflectionless sheets," *Phys. Rev. Lett.*, Vol. 110, 2013, Art. ID 197401.
- [6] A. Epstein and G. V. Eleftheriades, "Passive Lossless Huygens Metasurfaces for Conversion of Arbitrary Source Field to Directive Radiation," *IEEE Trans. Antennas Propag.*, Vol. 62, pp. 5680 - 5695, Nov. 2014.
- [7] S. Maci, G. Minatti, M. Casaletti, and M. Bosiljevac, "Metasurfing: Addressing waves on impenetrable metasurfaces," *IEEE Antennas Wireless Propag. Lett.*, Vol. 10, pp. 1499–1502, 2011.
- [8] M. Bosiljevac, M. Casaletti, F. Caminita, Z. Sipus, S. Maci, "Non-uniform Metasurface Luneburg Lens Antenna Design," *IEEE Trans. Antennas Propag.*, Vol. 60, pp. 4065-4073, Sep. 2012.
- [9] M. A. Moneum, Z. Shen, J.L. Volakis, and O. Graham, "Hybrid PO-MoM Analysis of Large Axi-Symmetric Radomes," *IEEE Trans. Antennas Propag.*, Vol. 49, pp. 1657-1666, 2001.
- [10] E. F. Kuester, M. A. Mohamed, M. Piket-May, and C. L. Holloway, "Averaged transition conditions for electromagnetic fields at a metafilm," *IEEE Trans. Antennas Propag.*, Vol. 51, pp. 2641-2651, 2003.
- [11] Y. Zhao, M. A. Belkin, and A. Alù, "Twisted optical metamaterials for planarized ultrathin broadband circular polarizers," *Nat. Commun.*, Vol. 3, pp. 870-876, 2012.

- [12] C. Pfeiffer and A. Grbic, "Cascaded metasurfaces for complete phase and polarization control," *Applied Physics Letters*, Vol. 102, Art. ID 231116, 2013.
- [13] F. Monticone, N. M. Estakhri, and A. Alù, "Full control of nanoscale optical transmission with a composite metascreen," *Phys. Rev. Lett.*, Vol. 110, Art. ID 203903, 2013.
- [14] M. Selvanayagam and G. V. Eleftheriades, "Polarization Control Using Tensor Huygens Surfaces," *IEEE Trans. Antennas Propag.*, Vol. 62, pp. 6155-6168, 2014.
- [15] A. M. Patel and A. Grbic, "Transformation electromagnetics devices based on printed-circuit tensor impedance surfaces," *IEEE Trans. Microwave Theory Tech.*, Vol. 62, pp. 1102 – 1111, 2014.
- [16] F. Elek, B. B. Tierney, and A. Grbic, "Synthesis of printed-circuit tensor impedance surfaces controlling phase and power flow," *IEEE Trans. Antennas Propag.*, Vol. 63, pp. 3956-3962, 2015.
- [17] B. O. Raeker and S. M. Rudolph, "Arbitrary Transformation of Antenna Radiation Using a Cylindrical Impedance Metasurface," *IEEE Antennas Wireless Propag. Lett.*, Vol. 15, pp. 1101-1104, 2016.
- [18] B. O. Raeker and S. M. Rudolph, "Verification of Arbitrary Radiation Pattern Control Using a Cylindrical Impedance Metasurface," *IEEE Antennas Wireless Propag. Lett.*, Vol. 16, pp. 995-998, 2017.
- [19] P.-Y. Chen, and A. Alu, "Mantle cloaking using thin patterned metasurfaces," *Phys. Rev. B*, Vol. 84, Art. ID 205110, 2011.
- [20] Y. R. Padooru, A. B. Yakovlev, P.-Y. Chen, and A. Alù, "Line-source excitation of realistic conformal metasurface cloaks," *J. Appl. Phys.*, Vol. 112, Art. ID 104902, 2012.
- [21] J. C. Soric, A. Monti, A. Toscano, F. Bilotti, and A. Alù, "Dual-Polarized Reduction of Dipole Antenna Blockage Using Mantle Cloaks," *IEEE Trans. Antennas Propag.*, Vol. 63, pp. 4827-4834, 2015.
- [22] S. Vellucci, A. Monti, A. Toscano, and F. Bilotti, "Scattering Manipulation and Camouflage of Electrically Small Objects through Metasurfaces," *Phys. Rev. Applied*, Vol. 7, Art. ID 034032, 2017.
- [23] A. Love, "Some highlights in reflector antenna development," *Radio Sci.*, Vol. 11, pp. 671–684, 1976.
- [24] N. Mohammadi Estakhri, C. Argyropoulos, and A. Alù, "Graded metascreens to enable a new degree of nanoscale light management," *Philos. Trans. R. Soc. A*, Vol. 373, Art. ID 20140351, 2015.
- [25] M. A. Francavilla, E. Martini, S. Maci, and G. Vecchi, "On the numerical simulation of metasurfaces with impedance boundary condition integral equation," *IEEE Trans. Antennas Propag.*, vol 63, pp. 2153-2160, 2015.
- [26] Z. Sipus, S. Raffaelli, P.-S. Kildal, "Periodic strips on planar and circular cylindrical substrates: Exact and asymptotic analysis," *Microwave and Optical Technology Letters*, Vol. 7, pp. 173-178, Feb. 1998.
- [27] O. Luukkonen, C. Simovski, G. Grant, G. Goussetis, D. Lioubtchenko, A. Raisanen, and S. Tretyakov, "Simple and accurate analytical model of planar grids and high-impedance surfaces comprising metal strips or patches," *IEEE Trans. Antennas Propag.*, vol 56, pp. 1624-1632, 2008.

- [28] C. R. Simovski, P. De Maagt, and I. V. Melchakova, "High-impedance surfaces having stable resonance with respect to polarization and incidence angle," *IEEE Trans. Antennas Propag.*, vol. 53, pp. 908-914, 2005.
- [29] D. M. Pozar, *Microwave Engineering*, John Wiley & Sons, 2011.
- [30] Z. Sipus, P.-S. Kildal, R. Leijon, and M. Johansson, "An algorithm for calculating Green's functions for planar, circular cylindrical and spherical multilayer substrates," *Applied Computational Electromagnetics Society Journal*, Vol. 13, pp. 243-254, Nov. 1998.
- [31] P.-S. Kildal, Z. Sipus, J. J. ang, and R. Maaskant, "Useful physical images and algorithms for vector dyadic green's functions," *IEEE Antennas Propag. Mag.*, Vol. 59, no. 4, pp. 106 - 116, Aug. 2017.
- [32] J. C. Vardaxoglou, *Frequency selective surfaces*. Research Studies Press Ltd., Taunton, England, 1997.
- [33] N. V. Shuley, "Higher-order mode interaction in planar periodic structures," *Proc. IEE-H*, Vol. 131, pp. 129-132, June 1984.
- [34] W. Y. Tam and K. M. Luk, "Resonances in spherical-circular microstrip structures of cylindrical-rectangular and wraparound microstrip antennas," *IEEE Trans. Microwave Theory Tech.*, Vol. 39, pp. 700-704, 1991.
- [35] R. F. Harrington, *Time-Harmonic Electromagnetic Fields*. McGraw-Hill Book Company, New York and London, 1961.
- [36] J. R. Wait and C. M. Jackson, "Calculations of the bistatic scattering cross section of a sphere with an impedance boundary condition," *Radio Sci.*, Vol. 69D, pp. 299-315, 1964.
- [37] CST Microwave Studio™ 2017 , Computer Simulation Technology AG, www.cst.com, Darmstadt, Germany
- [38] M. G. Andreasen, "Scattering from bodies of revolution," *IEEE Trans. Antennas Propag.*, Vol. AP-13, pp. 303-310, 1965.
- [39] J. R. Mautz and R. F. Harrington, *Electromagnetic scattering from homogeneous body of revolution*, Technical Report TR-77-10, Department of Electrical and Computer Engineering, Syracuse University, Nov. 1977.
- [40] J. R. Mautz and R. F. Harrington, *H-Field, E-Field, and Combined Field Solutions for Bodies of Revolution*, Interim Technical Report RA1K-TR-77-109, Air Force Base, New York, March 1977.
- [41] J. R. Mautz and R. F. Harrington, "Electromagnetic scattering from a homogeneous material body of revolution," *Arch. Elec. Übertragung.*, Vol. 33, pp. 71-80, Feb. 1979.
- [42] T. K. Wu and L. L. Tsai. "Scattering from arbitrarily-shaped lossy dielectric bodies of revolution," *Radio Sci.*, Vol. 12, pp. 709-718, Sept.-Oct. 1977.
- [43] A. W. Glisson and D. R. Wilton, *Simple and efficient numerical techniques for treating bodies of revolution*, Univ. Mississippi, RADC-TR-79-22, Rome Air Development Center, Griffiss AFB, NY, Mar. 1979.
- [44] A. W. Glisson and D. R. Wilton, "Simple and Efficient Numerical Methods for Problems of Electromagnetic Radiation and Scattering from Surface," *IEEE Trans. Antennas Propag.*, Vol 28, pp. 593-603, Sep. 1980.

- [45] F. J. S. Moreira, *Design and rigorous analysis of generalized axially-symmetric dual-reflector antennas*, Ph.D. dissertation, Univ. of Southern California, Los Angeles, Aug. 1997.
- [46] A. J. Poggio and E. K. Miller, "Integral Equation Solutions of Three Dimensional scattering Problems," Chap. 4 in *Computer Techniques for Electromagnetics*, edited by R. Mittra, Pergamon Press, 1973.
- [47] J. Yang and P.-S. Kildal, "A fast algorithm for calculating the radiation pattern in the longitudinal plane of antennas with cylindrical structure by applying asymptotic waveform evaluation in a spectrum of two dimensional solutions," *IEEE Trans. Antennas Propag.*, Vol. 52, pp.1700–1706, 2004.
- [48] C. A. Balanis, *Advanced Engineering Electromagnetics*, John Wiley&Sons, 2012, p. 584.
- [49] S. A. Tretyakov, *Analytical Modeling in Applied Electromagnetics*, Artech House, Norwood, 2003.
- [50] D. Depla, S. Mahieu, and J.E. Greene, "Sputter deposition processes," in *Handbook of Deposition Technologies for Films and Coatings*, 3rd ed., edited by P. M. Martin, William Andrew, Oxford, 2010, Chap. 5, pp. 253–296.
- [51] M. Schlesinger, M. Paunovic, *Modern electroplating*, J.Wiley&Sons, Fifth edition, 2010.
- [52] R.-S. Chu and K.-M. Lee, "Analytical method of a multilayered meander-line polarizer plate with normal and oblique plane-wave incidence,," *IEEE Trans. Antennas Propag.*, Vol. 35, pp.652-661, 1987, Errata Vol. 36, p. 1041, 1988.
- [53] R. J. Langley and E. A. Parker, "Equivalent circuit model for arrays of square loops," *Electronics Letters*, Vol. 18, pp. 294-296, 1982.
- [54] R. J. Langley and A. J. Drinkwater, "Improved empirical model for the Jerusalem cross," *IEE Proc. H - Microwaves, Optics and Antennas*, Vol. 129, pp. 1-6, 1982.
- [55] L. B. Wang, K. Y. See, J. W. Zhang, B. Salam, and A. C. W. Lu, "Ultrathin and flexible screen-printed metasurfaces for emi shielding applications," *IEEE Transactions on Electromagnetic Compatibility*, Vol. 53, pp. 700 – 705, 2011.